Doklady Physics, Vol. 49, No. 4, 2004, pp. 205–207. Translated from Doklady Akademii Nauk, Vol. 395, No. 4, 2004, pp. 467–469.

PHYSICS

Metallic Compounds of Uranium under Neutron Irradiation and the Possibility of Their Nondestructive Testing

Corresponding Member of the RAS V. P. Silin* and A. Z. Solontsov**

Received December 10, 2003

A model describing the effect of neutron irradiation on metallic uranium compounds is proposed to take into account two opposite phenomena, namely, effective expansion (swelling) of the crystal lattice due to an increase in the volume occupied by radiation-induced defects and compression caused by the pressure created on the crystal lattice by these defects. In magnetic uranium compounds such as uranium nitride UN, this compression results in a significant change in the antiferromagnetic transition temperature, whose measurement makes it possible to estimate the properties of the crystal lattice in the compound.

The majority of promising types of nuclear fuel presently being used or developed and similar uranium compounds exhibit strong magnetic properties. For example, uranium dioxide UO_2, uranium nitride UN, and uranium phosphate UP are antiferromagnets (their Néel temperatures are 180, 53, and 23 K, respectively). Uranium chalcogenide US is a ferromagnet (its Curie temperature is equal to 18 K) [1]. A strong magnetoelastic coupling is observed in all these compounds [1, 2]. In metallic uranium compounds UN and US, this coupling is gigantic and results in magnetostriction of the order of 10^{-3}, which is close to that found for invar alloys Fe–Ni, Fe–Ni–Cr, etc. [3]. Thus, magnetism in metallic uranium compounds is strongly coupled with their crystal lattice.

On the other hand, nuclear fuel under reactor conditions is irradiated, which results in its effective expansion (swelling) and burning out. This determines the service life of fuel in nuclear reactors. Despite numerous investigations, the mechanism of such an expansion determined by various radiation-induced defects remains unclear [4, 5]. In our opinion, the properties of the crystal lattice of fuel after the appearance of radiation-induced defects in it are also poorly known.

* *Lebedev Physical Institute, Russian Academy of Sciences, Leninskiĭ pr. 53, Moscow, 119924 Russia*

** *State Center for Condensed Matter Physics, ul. Rogova 5a, Moscow, 123060 Russia; Bochvar Institute of Inorganic Materials, ul. Rogova 5, Moscow, 123060 Russia*
e-mail: solontsov@newmail.ru

The effect of neutron irradiation on the magnetic properties of various uranium compounds, including those used as nuclear fuel, has been studied [6]. Even small irradiation doses ($<10^{17}$ decays cm^{-3}) turned out to lead to strong suppression of magnetism.

In this paper, we propose the following mechanism of the effect of small neutron irradiation doses and radiation-induced defects on the crystal lattice and magnetism of metallic uranium compounds, including nuclear fuel. First, we assume that radiation-induced defects (vacancies and gas pores, point defects, etc.) caused by irradiation of the crystal lattice immediately lead to the change ΔV_{rad} in the lattice volume. In turn, this change results in the appearance of an additional internal pressure P_{rad} in the lattice, which can be accompanied by the compression of the crystal lattice with a change in its volume $\Delta V_{int} < 0$. In this case, the total change in the crystal-lattice volume under irradiation is the sum of the intrinsic change in the lattice volume ΔV_{int} and the change ΔV_{rad} caused by radiation defects:

$$\Delta V_{eff} = \Delta V_{rad} + \Delta V_{int}. \quad (1)$$

Second, we assume that all variations of the magnetic properties of uranium compounds exposed to small doses of neutron irradiation under partial preservation of the magnetic order are entirely caused by the magnetovolume effect. This effect arises due to the change in the crystal-lattice volume under the pressure P_{rad}.

It should be noted that, in these compounds irradiated by neutrons, the positive volume change ΔV_{rad} due to radiation-induced defects may be compensated by the compression of the crystal lattice ($\Delta V_{int} < 0$) under the defect-induced pressure P_{rad}. In certain respects, such compensation is similar to the invar effect [3], which arises when the expansion of the crystal lattice due to the phonon anharmonicity is compensated by the lattice compression caused by the magnetovolume effect. It is worth noting that the compensation of the contributions ΔV_{rad} and ΔV_{int} to the total change in the volume of nuclear fuel can significantly reduce effects of its swelling and promote the prolongation of its service life in nuclear reactors.

1028-3358/04/4904-0205$26.00 © 2004 MAIK “Nauka/Interperiodica”

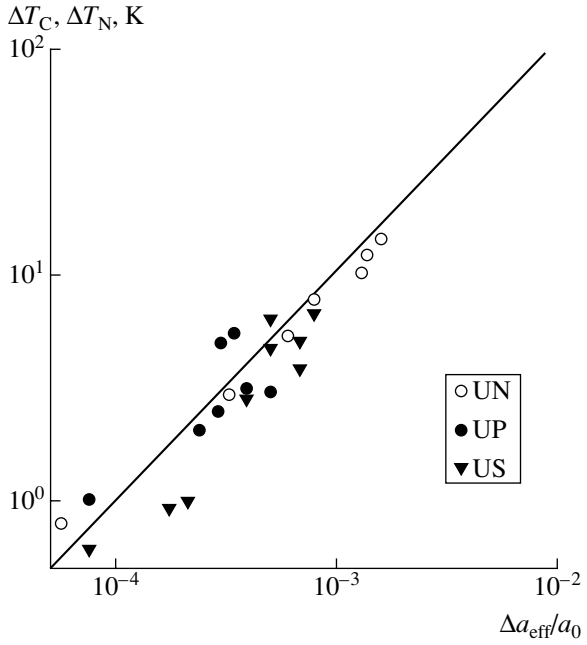

Absolute changes ΔT_N and ΔT_C in the magnetic-transition temperatures as a function of the effective variation of the crystal-lattice parameter $\Delta a_{eff}/a_0$ of antiferromagnetic (UN and UP) and ferromagnetic (US) uranium compounds irradiated by neutrons [9].

As an illustration of the proposed model that describes the behavior of uranium compounds under neutron irradiation, we now analyze the properties of uranium nitride UN. This compound is a relatively simple antiferromagnetic system with itinerant 5*f* electrons [6] and is considered as a promising nuclear fuel for fast-neutron nuclear reactors [7]. The effect of both external hydrostatic pressure [1, 2, 8] and neutron irradiation [9] on the magnetism of UN is investigated quite well, which allows simple estimates.

In the figure taken from [9], the absolute values of negative changes ΔT_N and ΔT_C in, respectively, the Néel and Curie temperatures of a number of metallic uranium compounds having the NaCl structure are given as functions of the effective change Δa_{eff} in the lattice parameter corresponding to formula (1). As is seen in the figure, for a relative change of 10^{-3} in the effective lattice parameter, the temperature of the magnetic transition in antiferromagnetic UN decreases by about 10 K. Therefore, the relative variation of the total volume is equal to

$$\frac{\Delta V_{eff}}{V} = 3\frac{\Delta a_{eff}}{a_0} \approx 3 \times 10^{-3}. \quad (2)$$

Here, V and a_0 are the volume and parameter of the crystal lattice prior to irradiation, respectively. It is of interest that, according to the figure, the decrease ΔT_N in the magnetic-transition temperature of UN due to the total irradiation-induced change in volume can be described by the empirical formula

$$\frac{\Delta T_N}{T} = \eta_{rad}\frac{\Delta V_{eff}}{V}, \quad (3)$$

where, e.g., for UN,

$$\eta_{rad} = \frac{\partial \ln T_N}{\partial \ln V} \approx -63. \quad (4)$$

We now take into account the experimental data on the magnetovolume effect in UN [1, 2]:

$$\eta_{int} = \frac{\partial \ln T_N}{\partial \ln V} \approx 19. \quad (5)$$

Using these data, we can estimate the relation between the intrinsic change ΔV_{int} caused in the crystal-lattice volume by its compression due to radiation-induced defects and the total change ΔV_{eff} including the effect of radiation-induced defects (swelling). For UN, we have

$$\frac{\Delta V_{int}}{V} = \frac{\Delta V_{eff}}{V}\frac{\eta_{rad}}{\eta_{int}} \approx -3.3\frac{\Delta V_{eff}}{V}. \quad (6)$$

In this case, the volume change due to radiation-induced defects is

$$\frac{\Delta V_{rad}}{V} = \frac{\Delta V_{eff}}{V} - \frac{V_{int}}{V} \approx 4.3\frac{\Delta V_{eff}}{V}. \quad (7)$$

As follows from the comparison of formulas (5) and (7), in uranium nitride, the positive contribution to the volume change $\Delta V_{rad} = 4.3\Delta V_{eff} > 0$, which is caused by radiation-induced defects and results in expansion (swelling) of the crystal lattice, is partially compensated by the negative contribution $\Delta V_{int} = -3.3\Delta V_{eff} < 0$ caused by the compression of the crystal lattice due to the pressure P_{rad} of radiation-induced defects.

Finally, we can estimate the pressure that is caused by radiation-induced defects and results in the compression of the crystal lattice. For UN, we arrive at the relations

$$P_{rad} = -B_0\frac{\Delta V_{int}}{V} = -B_0\frac{\Delta V_{eff}}{V}\frac{\eta_{rad}}{\eta_{int}} \approx 670\frac{\Delta V_{int}}{V}\ \text{GPa}, \quad (8)$$

where $B_0 = 203$ GPa is the bulk modulus of UN [10]. For irradiation doses corresponding to total change (2) in the lattice volume, i.e.,

$$\frac{\Delta V_{eff}}{V} \approx 3 \times 10^{-3},$$

this pressure reaches 2.0 GPa.

On the basis of the above model for the behavior of uranium compounds under neutron irradiation, we may suggest new approaches to the nondestructive control of nuclear fuel in the case of small irradiation doses. One of these approaches is associated with both the determination of the irradiation-induced shift of the magnetic-transition temperature in nuclear fuel and the

calculation of the volume variations ΔV_{int}, ΔV_{rad}, and ΔV_{eff}, which makes it possible to evaluate the effects of fuel swelling by using the above model. The measurements can be carried out by various methods, namely, by measuring kinetic properties (electrical and thermal conductivity), magnetic susceptibility, specific heat, etc., which have pronounced anomalies at the magnetic-transition point [1].

In addition, the above model is suitable for analyzing the properties of neutron-irradiated construction materials based on austenitic and ferrite-martensitic steels, because these steels are basically antiferromagnetic and have strong magnetic properties.

ACKNOWLEDGMENTS

This work was supported by the program "Strongly Correlated Electrons in Semiconductors, Metals, Superconductors, and Magnetic Materials," by the Council of the President of the Russian Federation for Support of Young Russian Scientists and Leading Scientific Schools (project no. NSh-1385.2002.2) and by the European Science Foundation (program "Fermi Liquid Instabilities in Correlated Metals"). A.Z.S. is grateful to G. Lonzarich, P.P. Poluéktov, V.V. Inozemtsev, and M.E. Mazur for fruitful discussions.

REFERENCES

1. P. Erdos and J. M. Robinson, *Actinide Compounds* (Plenum, New York, 1983).
2. J. M. Fournier, Physica B **130**, 268 (1985).
3. E. F. Wassermann, in *Ferromagnetic Materials*, Ed. by K. H. Buschow and E. P. Wohlfarth (North-Holland, Amsterdam, 1991), Vol. 5.
4. I. I. Konovalov, Preprint No. 2001-3, VNIINM (All-Russia Research Institute of Inorganic Materials, Moscow, 2001).
5. F. A. Garner and M. B. Toloczko, Radiat. Eff. Defects Solids **148**, 479 (1999).
6. A. Z. Solontsov and V. P. Silin, Preprint No. 24, FIAN (Lebedev Physical Institute, Russian Academy of Sciences, Moscow, 2003); Fiz. Met. Metalloved. **97** (6) (2004).
7. V. V. Orlov, V. N. Leonov, A. G. Sila-Novitskiĭ, *et al.*, in *Proceedings of the International Seminar on Fast Reactors and Fuel Cycle* (Min. Atom. Énerg., Moscow, 2000), pp. 9–21.
8. D. Braithwaite, A. Demuer, and I. N. Goncharenko, J. Alloys Compd. **271–273**, 426 (1998).
9. H. Matsui, M. Tumaki, M. Horiki, and T. Kirihara, in *Proceedings of International Conference on Actinides, Tashkent, 1989*, pp. 160–161.
10. U. Benedict, J. Less-Common Met. **100**, 153 (1984).
11. A. Z. Men'shikov and A. E. Teplykh, Fiz. Met. Metalloved. **57**, 391 (1984).

Translated by G. Merzon

Doklady Physics, Vol. 49, No. 4, 2004, pp. 208–212. Translated from Doklady Akademii Nauk, Vol. 395, No. 6, 2004, pp. 751–755.

PHYSICS

Effect of Barrier Mechanisms of Polarization on the Determination of the Parameters of Polyacene Quinone Semi-Electrics

N. V. Afanas'ev, L. V. Mukhaeva, T. G. Ermakova, and Academician M. G. Voronkov

Received December 8, 2003

To develop the method for analyzing a complicated dielectric spectrum of a semi-electric, or polymeric semiconductor formed of conducting macromolecules, we use the effect of their pseudo-isolation [1] discovered for polyacene quinones as an example. This is necessary for developing methods of synthesis of polymeric materials used in molecular electronics [2].

We study 76EHE(5) polyacene quinone obtained by polycondensation of pyromellite dianhydride with pyrene for five hours by the procedure presented in [3] (previously, the reaction was carried out for 24 h). Reduction of the duration of the polycondensation process made it possible to reduce the specific conductivity at constant current σ_0 and to measure not only permittivity ε' [3, 4] but also the loss factor ε''. In [5], due to these measurements, three dispersion regions for ε' and ε'' were found in the spectrum of a pressed polymer sample by the method of circle diagrams. These regions are numbered in order of increasing frequency ν_{max} of the ε'' maximum and correspond to different polarization mechanisms. The first dispersion region is attributed to interlayer polarization [6] associated with the Schottky barrier; the second region is attributed to the surface capacity of grains [7], which is associated with their surface barriers; and the third region is attributed to the interlayer polarization of three-dimensional conducting macromolecules [8].

The spectrum structure was qualitatively corroborated [9], but its parameters were incorrect. In particular, the frequency $\nu_{max3} = 5$ MHz [5] of the ε'' maximum in the third dispersion region must be treated as overestimated by more than one order of magnitude on the basis of the pseudo-isolation effect. This effect is a decrease in ν_{max3} compared to its value $\nu'_{max3} \approx 200$ kHz [5] in the spectrum of the mixture of 76EHE(5) polyacene quinone powder with paraffin isolating grains.

The error was caused by using the rule for plotting circle diagrams for neighboring dispersion regions in the complicated spectra of ordinary dielectrics [10], where barrier polarization mechanisms, as well as interlayer polarization itself, are not observed in the frequency band available for measurements of ε' and ε'' due to low conductivity. According to this rule, the low-frequency edge ε'_{3s} of the third dispersion region must coincide with the high-frequency edge $\varepsilon'_{2\infty}$ of the second region:

$$\varepsilon'_{3s} = \varepsilon'_{2\infty}. \quad (1)$$

Therefore, the neighboring circle diagrams must touch rather than intersect each other. To decrease ν_{max3}, it is necessary to increase ε'_{3s} as is shown in Fig. 1a. However, for a fixed $\varepsilon'_{2\infty}$ value, this increase leads to the intersection of the circle diagrams:

$$\varepsilon'_{3s} > \varepsilon'_{2\infty}. \quad (2)$$

Equality (1) of ε' limits follows from the principle of superposition of contributions from uncoupled polarization mechanisms to the complex permittivity ε of a semi-electric. It is also expected that this equality will be satisfied in the absence of perturbation of the spectrum in the third dispersion region by surface-barrier polarization. To this end, the dispersion regions must not be too close to each other in the spectrum. The second region is observed in the sonic and ultrasonic bands, and the third region lies in the rf band. However, the latter is comparatively small and perturbation is therefore considerable.

We assume that the unperturbed spectrum in each dispersion region is a Debye spectrum. In the absence of the Schottky barrier, the observed spectrum with allowance for the effect of the surface-barrier polariza-

Irkutsk State Technical University, ul. Lermontova 83, Irkutsk, 664074 Russia
Irkutsk Institute of Chemistry, Siberian Division, Russian Academy of Sciences, ul Favorskogo 1, Irkutsk, 664033 Russia

1028-3358/04/4904-0208$26.00 © 2004 MAIK "Nauka/Interperiodica"

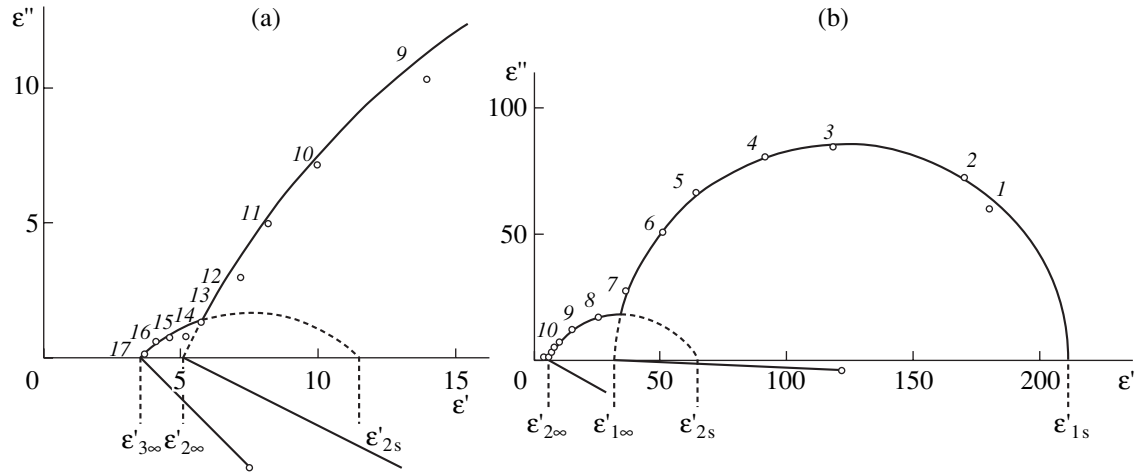

Fig. 1. Circle diagrams for 76EHE(5) polyacene quinone in the (a) third and (b) first and second dispersion regions for a frequency of (*1*) 0.1, (*2*) 0.2, (*3*) 0.4, (*4*) 0.6, (*5*) 1, (*6*) 2, (*7*) 3, (*8*) 5, (*9*) 10, (*10*) 30, (*11*) 50 kHz, (*12*) 0.15, (*13*) 0.5, (*14*) 1.5, (*15*) 5, (*16*) 12, and (*17*) 50 MHz.

tion on the polarization of macromolecules is described by the equation

$$\varepsilon(\nu) = \varepsilon'_{3\infty} + \frac{\Delta\varepsilon'_3}{1 + (jz_3)^{\alpha_3}} + \frac{\Delta\varepsilon'_2}{1 + (jz_2)^{\alpha_2}} - f(z_2)\frac{\Delta\varepsilon'_3}{1 + (jz_3)^{\alpha_3}}. \quad (3)$$

Here, j is the imaginary unit, $z = \dfrac{\nu}{\nu_{max}}$, $\Delta\varepsilon' = \varepsilon'_s - \varepsilon'_\infty$ is the ε' increment in the dispersion region, and both the parameter α of the relaxation-time distribution and effect factor f lie from 0 to 1.

Since the circle-diagram method is based on the geometric interpretation of the relation between ε' and ε" on the complex plane corresponding to Eq. (3), rule (1) for ordinary dielectrics must be satisfied for $f = 0$.

For semi-electrics, the effect of barrier polarization is negligibly small in the absence of perturbation ($z_2 \to \infty$). Therefore, the neighboring circle diagrams must only touch each other according to equality (1) of limits. To satisfy this requirement, it is necessary to set $f = 0$ in Eq. (3). In this case, the static permittivity ε'_s of the semi-electric, which is measured at low frequencies ($\nu \ll \nu_{max2}$), is determined by the sum of increments $\Delta\varepsilon'$ of the unperturbed dispersion regions according to equality (1):

$$\varepsilon'_s = \varepsilon'_{3\infty} + \Delta\varepsilon'_3 + \Delta\varepsilon'_2. \quad (4)$$

In the presence of perturbation, $\Delta\varepsilon'_3$ decreases due to the effect of the surface barrier that corresponds to $f > 0$. Therefore, the neighboring circle diagrams intersect each other, and the ε'_s value is smaller according to inequality (2) between limits:

$$\varepsilon'_s = \varepsilon'_{3\infty} + (1 - f_s)\Delta\varepsilon'_3 + \Delta\varepsilon'_2. \quad (5)$$

Here, the effect factor can be expressed as

$$f_s = \frac{\Delta\varepsilon'_3 - (\varepsilon'_{2\infty} - \varepsilon'_{3\infty})}{\Delta\varepsilon'_3}. \quad (6)$$

In this case, according to Fig. 1a, the contribution from the interlayer polarization of macromolecules to ε'_s is as small as 20% of the unperturbed value, because $f_s = 0.8$ according to formula (6).

In the model of the surface capacity of grains [7], air gaps between polymer grains are disregarded [9], because they are bypassed by surface electric conductivity through electron traps. The surface barrier is formed between resistance R_1 in a grain and its bulk resistance $R_2 < R_1$, which leads to the redistribution of the applied voltage to the barrier. This redistribution reduces the contribution from macromolecules in the grain bulk to the ε value. Therefore, f in Eq. (3) is positive for any frequency. For $\nu \ll \nu_{max2}$, when surface-barrier polarization follows the applied electric field, the grain is virtually nontransparent for this field. In this case, $f = f_s \approx 1$, and the contribution from macromolecules is negligible. If $\nu \gg \nu_{max2}$ ($z_2 \to \infty$), barrier polarization cannot be established during the half-period of the applied voltage, the grain becomes transparent for the field, and the third dispersion region is observed in the part corresponding to $f_s = 0.8$. However, this part presents the unperturbed (Debye) spectrum corresponding to $f = f_\infty = 0$ and, therefore, to the unperturbed $\Delta\varepsilon'_3$ value in Eq. (3).

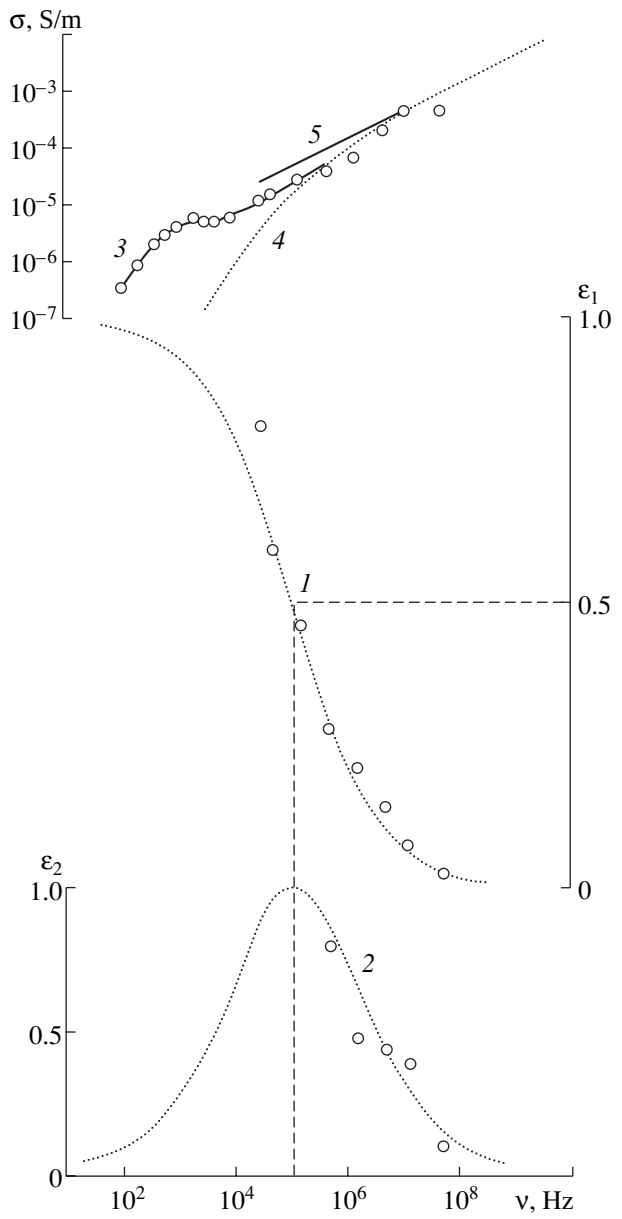

Fig. 2. Dispersion patterns for 76EHE(5) polyacene quinone that are constructed using the data for the third dispersion region shown in Fig. 1a: (*1*) ε_1 for $\Delta\varepsilon' = 8$ and $\varepsilon'_\infty = 3.5$, (*2*) ε_2 for $\varepsilon''_{max} = 1.67$ and $\alpha = 0.5$, (*3*) the active conductivity σ of the sample, (*4*) the theoretical σ value for the third dispersion region, and (*5*) the logarithmic asymptote of active conductivity.

The above method of overlapping circle diagrams with allowance for inequality (2) of ε' limits includes the construction of the circle diagram based only on the observed part of the third dispersion region. However, such a construction is not uniquely defined, because the experimental part of an arc is small. Due to the noticeable random error in measurement of ε'' near the high-frequency edge of the third region (Fig. 2, line *4*), it is impossible to apply the logarithmic-asymptote method [11]. This difficulty is overcome by using the pseudo-isolation-effect method [12], which is applicable for model semi-electrics corresponding to the structure model of polydispersion. According to this model, polyacene quinone macromolecules are spherical and distributed over the size and conductivity in the dielectric matrix with the volume concentration of the conducting phase v in a pressed sample and $v' \ll v$ in the mixture with paraffin. When plotting variants of the circle diagram (Fig. 1a), the $\Delta\varepsilon'_3$ value is determined by the formula

$$\Delta\varepsilon'_3 = \eta(\mu - 1) \tag{7}$$

for various pseudo-isolation-effect parameters

$$\mu = \frac{\nu'_{max3}}{\nu_{max3}} > 1. \tag{8}$$

The η coefficient is calculated by the formula

$$\eta = \frac{\varepsilon'_p}{(1 - v')N} + \varepsilon'_{3\infty} - \varepsilon'_p, \tag{9}$$

where $0 \le N \le 1$ is the depolarization coefficient of macromolecules, which depends on their shape, and ε'_p is the permittivity of paraffin. Taking $N = \frac{1}{3}$ for the spherical shape, $\varepsilon'_{3\infty} = 4$ [12], $\varepsilon'_p = 2$, and $v' = 0.1$, we obtain $\eta = 0.87$.

To choose a variant of the circle diagram, we use the dispersion-plot method [13], in which values measured for permittivity $\varepsilon_1 = \frac{\varepsilon' - \varepsilon'_\infty}{\Delta\varepsilon'}$ and the loss factor $\varepsilon_2 = \frac{\varepsilon''}{\varepsilon''_{max}}$ are compared with their theoretical values under the assumption of the applicability of the generalized Debye equation for the description of the spectrum in the third dispersion region. According to Fig. 2, the chosen value $\Delta\varepsilon'_3 = 8$, which corresponds to the acceptable value $N = 0.37$ for $\nu_{max} = 110$ kHz (Fig. 2), $\nu'_{max} = 225$ kHz [5], and $\varepsilon'_\infty = 3.5$ (Fig. 1a), is larger than the previously obtained value $\Delta\varepsilon'_3 = 2.5$ [5] by a factor of 3. However, it is equal to one-third of the value obtained by the logarithmic-asymptote method from independent data [11]. This difference can be attributed to the fact that, due to the inclusion of the surface barrier, the dimension effect is observed for smaller grains. The dimension effect was previously assumed only for grains smaller than the radius of macromolecules [14].

The effect of the Schottky barrier on the surface-barrier polarization is similar. For low frequencies ($\nu \ll \nu_{max1}$), the sample bulk can be treated as a continuation of an electrode, because the applied voltage is redistributed to the thin near-electrode high-ohmic layer. Therefore, the contribution of grains in the bulk of a pressed sample to the permittivity ε of the semi-electric is neg-

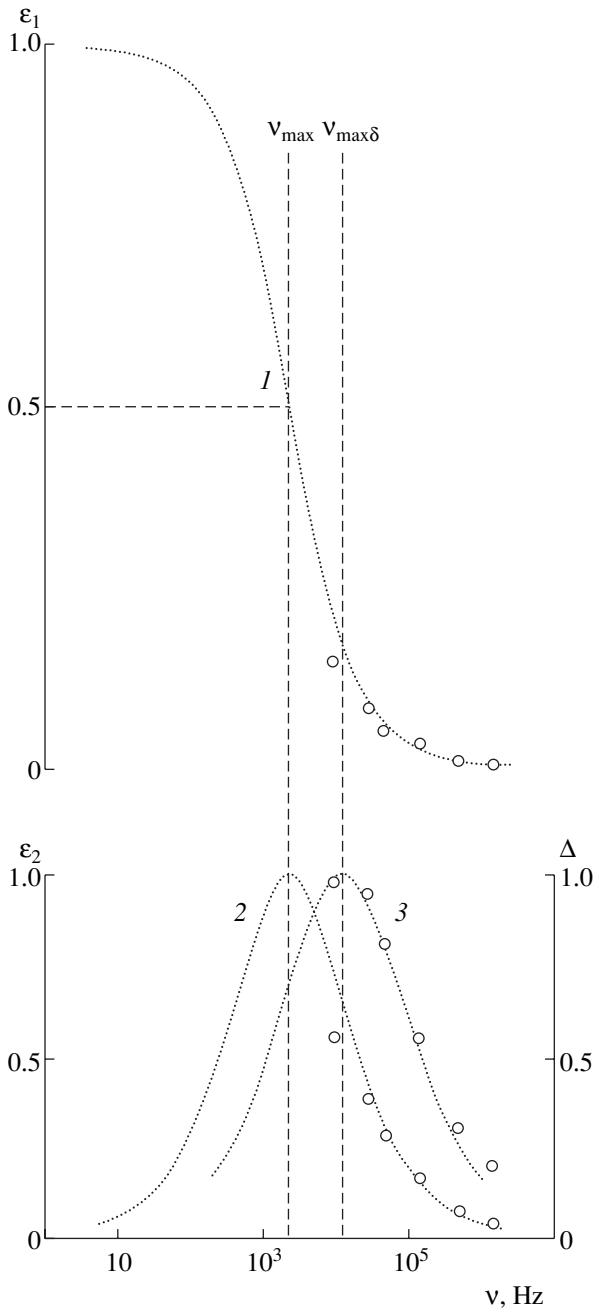

Fig. 3. Dispersion patterns for 76EHE(5) polyacene quinone constructed using the data for the second dispersion region shown in Fig. 1b: (*1*) ε_1 for $\Delta\varepsilon' = 60$ and $\varepsilon'_\infty = 5.1$, (*2*) ε_2 for $\varepsilon''_{max} = 18.4$, and (*3*) Δ for $\tan\delta_{max} = 0.75$ and $\alpha = 0.7$.

ligible. For high frequencies ($\nu \gg \nu_{max1}$), the sample bulk becomes transparent to the electric field and the second dispersion region is observed in the part that is close to the high-frequency edge and corresponds to the unperturbed Debye spectrum.

The parameters of the second dispersion region are determined in a similar approach, i.e., the construction of the circle diagram disregarding $\varepsilon'_{1\infty}$ according to the inequality of ε' limits (Fig. 1b). However, a variant of dispersion plots is chosen by the method of the auxiliary maximum $\tan\delta_{max}$ [15] of the loss-angle tangent $\tan\delta = \frac{\varepsilon''}{\varepsilon'}$, which is observed in contrast to the maximum of ε'' (Fig. 3, lines *2*, *3*). The correspondence of the observed spectrum of $\tan\delta$ to the Debye spectrum is checked by the method of dispersion Δ plots, in which values measured for the relative loss-angle tangent $\Delta = \frac{\tan\delta}{\tan\delta_{max}}$ are compared with the theoretical formula [15]

$$\Delta(y) = \frac{2 + b}{y^{\alpha} + y^{-\alpha} + b}. \qquad (10)$$

Here, $y = \frac{\nu}{\nu_{max\delta}}$, where $\nu_{max\delta}$ is the frequency of the maximum of $\tan\delta$, and $b = (\chi^{1/2} + \chi^{-1/2})\cos\alpha\pi/2$, where $\chi = \frac{\varepsilon'_{2s}}{\varepsilon'_{2\infty}}$. The $\varepsilon'_{2\infty}$ value is correct because the parameters of the second dispersion region satisfy the formula [15]

$$\frac{\nu_{max\delta}}{\nu_{max}} = \chi^{1/2\alpha} \qquad (11)$$

within an accuracy of 7%.

The above study shows that the possibility of violating the superposition principle must be taken into account when using circle diagrams to analyze the complicated spectra of polymeric semiconductors.

REFERENCES

1. N. V. Afanas'ev, L. V. Mukhaeva, M. G. Voronkov, and T. G. Ermakova, Dokl. Akad. Nauk **360**, 614 (1998) [Dokl. Phys. **43**, 330 (1998)].
2. V. I. Minkin, Zh. Khim. O–va im D. I. Mendeleeva **49** (6), 3 (2000).
3. R. Rosen and H. A. Pohl, J. Polym. Sci. [A1] **4**, 1135 (1966).
4. R. V. Afanas'eva, N. V. Afanas'ev, T. G. Ermakova, *et al.*, Vysokomol. Soedin., Ser. B **19**, 698 (1977).
5. N. V. Afanas'ev, R. V. Afanas'eva, T. G. Ermakova, *et al.*, Vysokomol. Soedin., Ser. A **21**, 413 (1979).
6. *Dielectrics: A Handbook of Recommended Terms*, Ed. by B. M. Tareev (Izd. Akad. Nauk SSSR, Moscow, 1961).
7. N. V. Afanas'ev, L. V. Mukhaeva, M. G. Voronkov, and T. G. Ermakova, Dokl. Akad. Nauk **337**, 595 (1994) [Phys. Dokl. **39**, 556 (1994)].

8. N. V. Afanas'ev, L. V. Mukhaeva, M. G. Voronkov, and T. G. Ermakova, Dokl. Akad. Nauk SSSR **323**, 452 (1992) [Sov. Phys. Dokl. **37**, 135 (1992)].
9. N. V. Afanas'ev, L. N. Omel'chenko, L. V. Mukhaeva, *et al.*, Dokl. Akad. Nauk SSSR **289**, 596 (1986) [Sov. Phys. Dokl. **31**, 572 (1986)].
10. A. R. von Hippel, *Dielectrics and Waves* (Wiley, New York, 1954; Inostrannaya Literatura, Moscow, 1960).
11. N. V. Afanas'ev, L. V. Mukhaeva, M. G. Voronkov, and T. G. Ermakova, Dokl. Akad. Nauk **326**, 999 (1992) [Sov. Phys. Dokl. **37**, 508 (1992)].
12. N. V. Afanas'ev, L. V. Mukhaeva, L. Ya. Tsarik, *et al.*, Dokl. Akad. Nauk **367**, 179 (1999) [Dokl. Phys. **44**, 413 (1999)].
13. N. V. Afanas'ev, L. V. Mukhaeva, M. G. Voronkov, *et al.*, Dokl. Akad. Nauk SSSR **319**, 858 (1991) [Sov. Phys. Dokl. **36**, 580 (1991)].
14. N. V. Afanas'ev, L. V. Mukhaeva, M. G. Voronkov, and T. G. Ermakova, Dokl. Akad. Nauk **330**, 177 (1993) [Phys. Dokl. **38**, 205 (1993)].
15. N. V. Afanas'ev, L. V. Mukhaeva, M. G. Voronkov, and T. G. Ermakova, Dokl. Akad. Nauk **336**, 179 (1994) [Phys. Dokl. **39**, 333 (1994)].

Translated by R. Tyapaev

Doklady Physics, Vol. 49, No. 4, 2004, pp. 213–217. Translated from Doklady Akademii Nauk, Vol. 395, No. 6, 2004, pp. 756–760.

PHYSICS

Study of Microstrip Models of Band-Pass Filters Based on Superlattices

B. A. Belyaev*, A. S. Voloshin, and Academician V. F. Shabanov

Received December 25, 2003

Current technologies of the epitaxial growth of thin films make it possible to produce multilayer structures consisting of alternating layers of different materials with a thickness comparable with the crystal lattice constant. Such structures belong to superlattices and, due to their unique physical properties, are promising for the creation of various radio- and optoelectronic devices. In particular, multilayer structures consisting of alternating magnetic and nonmagnetic metallic layers can be used as detectors of magnetic fields, because they are characterized by the giant magnetoresistive effect [1]. Superlattices consisting of alternating dielectric layers with different permittivities are used as polarizers in switching devices in fiber-optic communication lines [2]. They can serve as filters and mirrors for electromagnetic waves of the x-ray, as well as optical, band [3, 4]. In addition, superlattices are used to create various photonic crystals, which have been intensively studied in recent years [5, 6].

In view of the difficult technological problems of the manufacture of high-quality multilayer structures and their high cost, it is sometimes appropriate to carry out preliminary experimental investigations of the properties of superlattices on bulk (non-film) analogues working at frequencies much lower than optic frequencies. For example, irregular waveguide structures working in the UHF band can be used as an analogue of a superlattice consisting of alternating dielectric layers, which can be used as a filter or mirror in a certain frequency band. In particular, experimental investigations of the frequency dependences of passing and reflecting powers with respect to incident power with variation of the number and parameters of layers in a structure are usually carried out by using waveguides containing various irregularities, such as dielectric or metallic pins, steps, etc., as well as special corrugated waveguides.

In this work, we proposed a microstrip model for studying the properties of superlattices. It is simple and can be easily manufactured. Its main advantage is that its properties are closer to the real layered structure of a superlattice than those of waveguide analogues. This advantage is due to the fact that the basic oscillation modes propagating in microstrip transmission lines are quasi-TEM waves whose rf-field structure virtually coincides with the structure of the fields of transverse waves propagating in superlattices. At the same time, waves propagating in waveguides are either *E* or *H* waves that have either electric or magnetic rf-field components along the propagation direction, respectively.

BASIC RESULTS

The effective permittivity determining the propagation velocity and, correspondingly, the electromagnetic wavelength in a microstrip transmission line is expressed in terms of the basic parameters of the line as [7]

$$\varepsilon_{\text{eff}} = \frac{\varepsilon + 1}{2} + \frac{\varepsilon - 1}{2} P,$$

where

$$P = \begin{cases} \dfrac{1}{\sqrt{1 + \dfrac{12h}{w}}} & \text{for} \quad w \geq h \\ \dfrac{1}{\sqrt{1 + \dfrac{12h}{w}}} + 0.04\left(1 - \dfrac{w}{h}\right)^2 & \text{for} \quad w \leq h, \end{cases} \tag{1}$$

h is the substrate thickness, ε is the relative permittivity, and w is the width of the strip conductor. Formula (1) is valid for the zero-thickness strip conductor and only in the quasistatic frequency band, when the width w and thickness h of the microstrip transmission line are much shorter than the length of an electromagnetic wave propagating in the line.

Figure 1 shows the ratio $\dfrac{\varepsilon_{\text{eff}}}{\varepsilon}$ calculated by Eq. (1) as a function of the relative width of the strip conductor for three substrate materials—FLAN, alumina, and

Kirenskiĭ Institute of Physics, Siberian Division, Russian Academy of Sciences, Akademgorodok, Krasnoyarsk, 660036 Russia

** e-mail: belyaev@iph.krasn.ru*

1028-3358/04/4904-0213$26.00

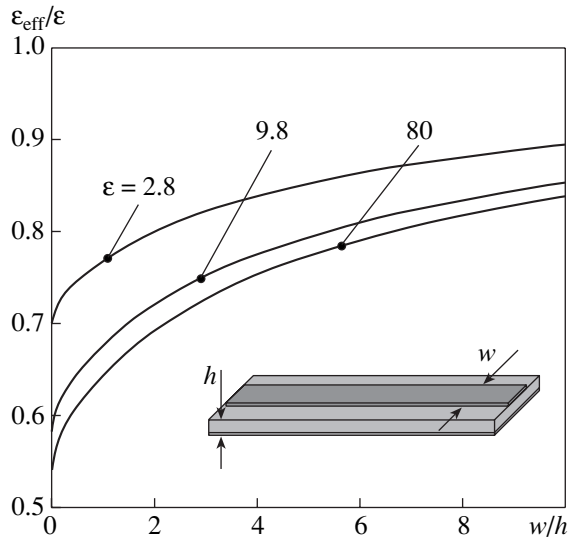

Fig. 1. Effective permittivity of the microstrip line vs. the relative width of the strip conductor.

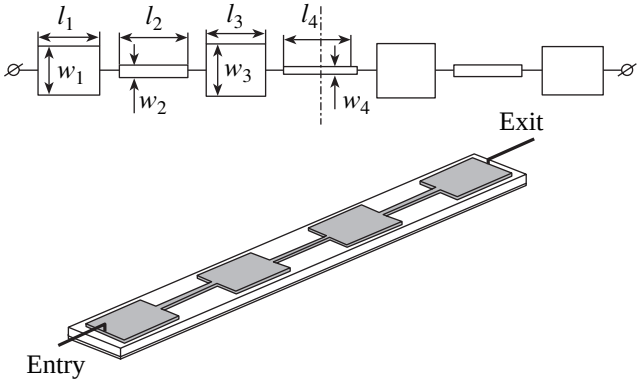

Fig. 2. Microstrip model of a seven-layer superlattice.

TBNS ceramic with ε = 2.8, 9.8, and 80, respectively—widely used in UHF equipment. As is seen, the range of variation in the effective permittivity with an increase in w is relatively wide for all substrates. In particular, $\varepsilon_{\text{eff}} \approx 45$ and 67 for a microstrip transmission line on a 1-mm-thick TBNS-ceramic substrate whose width is w = 0.1 and 10 mm, respectively. These properties make it possible to develop microstrip models of the above superlattice that are a series of regular segments of microstrip lines with different widths of conductors. Figure 2 shows a construction that is symmetric with respect to its middle and consists of seven segments of microstrip lines whose conductors have widths $w_1 - w_4$ and lengths $l_1 - l_4$.

Such a construction operates in the UHF band as a low-frequency filter. However, with the appropriate adjustment, it can also be used as a band-pass filter. As an example, Fig. 3 shows the frequency response of the (solid lines) direct losses of UHF power passed through the microstrip structure and (dashed lines) reflection losses. Figure 3a is given for a filter that is based on a 1-mm-thick alumina substrate (ε = 9.8) and has a pass band with central frequency f_0 = 3 GHz and relative width $\frac{\Delta f_3}{f_0}$ = 40% measured at a level of –3 dB from the minimum-loss level. The parametric synthesis of the seven-segment construction under consideration was carried out numerically in the quasistatic approximation. In addition to the central frequency and width of the pass band, the maximum reflection level in the band was given as L_r = –14 dB. The adjustment of the filter was performed by correcting the length and width of strip conductors in each regular segment.

Regular segments of the lines in the microstrip construction under consideration, which model corresponding dielectric layers of a superlattice, are obviously resonators. Therefore, the number of the minima of reflection losses in the pass band of the microstrip structure is equal to the number of regular segments in it. It is worth noting that three conditions must be satisfied for the adjustment of the superlattice model as well as for the tuning of any multisegment band-pass filter. First, outer resonators (segments) must be properly coupled with the input and output transmission lines. This coupling is determined by the given pass band of a device. Second, couplings between all segments must be balanced. Third, the resonance frequencies of segments must coincide with the central frequency of the pass band. Coupling between adjacent resonators is primarily determined by the difference between the wave resistances of their microstrip lines. In the quasistatic region, these resistances are calculated by the formulas

$$Z = \begin{cases} \dfrac{\dfrac{120\pi}{\sqrt{\varepsilon_{\text{eff}}}}}{1.393 + \dfrac{w}{h} + 0.667\ln\left(\dfrac{w}{h} + 1.444\right)} & \text{for} \quad w \geq h \\ \dfrac{60}{\sqrt{\varepsilon_{\text{eff}}}}\ln\left(\dfrac{8h}{w} + \dfrac{w}{4h}\right) & \text{for} \quad w \leq h. \end{cases} \tag{2}$$

Coupling between resonators with the external section is determined by the difference in the wave resistances of the carrying transmission lines $Z_0 = 50\ \Omega$ and the corresponding segments of the microstrip transmission lines in the model under consideration. Coupling between segments in the microstrip structure is determined not only by jumps in wave resistances but also by the loaded Q-factor of the resonators. This factor affects the amplitudes of rf fields in the resonators and is higher for inner segments. As a result, to ensure a given coupling constant between inner resonators, the jump of the wave resistances of their line segments

must be larger than that for the outer resonators. This fact is reflected by the construction parameters obtained from the parametric synthesis of the microstrip model under consideration and presented in the table in comparison with the construction parameters of a similar filter whose pass band has a relative width of $\frac{\Delta f_3}{f_0} = 60\%$.

Figure 3b shows the frequency dependences of (solid line) direct and (dashed line) reflection losses for the microstrip structure under consideration for $l_1 = l_2 = l_3 = l_4 = 17.19$ mm. In this case, the width of the conductors in the regular segments with low wave resistance is equal to the width of the first segment, $w_1 = w_3 = 3.92$ mm, and the width of the conductors with high wave resistance is equal to the width of the second segment, $w_2 = w_4 = 0.10$ mm. Such a construction corresponds to a superlattice consisting of seven alternating layers with equal thickness with the permittivities $\varepsilon_1 = 7.58$ and $\varepsilon_2 = 5.94$ (see table). In this case, the pass band includes strong reflections, leading to unacceptably large irregularity of the frequency response. Moreover, the width of the pass band increases and the stop levels decrease considerably both to the left and right of this band. These properties are obviously attributed to the higher natural frequencies of the layers with low permittivity, which are pronounced in the frequency response (Fig. 3), as well as to unbalanced couplings between resonators. Therefore, a superlattice consisting of alternating layers with different permittivities and identical thicknesses cannot serve as a band-pass filter.

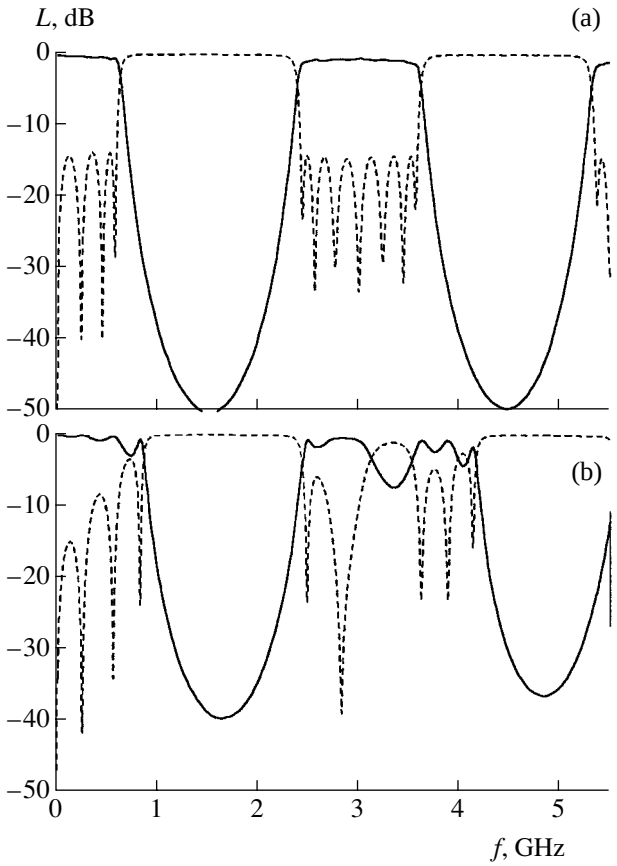

Fig. 3. Frequency dependences of (solid lines) losses in the passed electromagnetic wave and (dashed lines) reflection losses in the microstrip model of the superlattice with (a) optimized layer parameters and (b) identical thickness of alternating layers.

The experiment with several superlattice models made by the lacquer engraving method [8] agrees quite well with the numerical calculation. As an example, Fig. 4a shows measurements of direct and inverse losses for a seven-element filter that had a relative width of the pass band of $\frac{\Delta f_3}{f_0} = 60\%$ and was obtained by the parametric synthesis on a 1-mm-thick alumina substrate. The lines are calculations for the model where the real construction parameters of the microstrip structure are used: $w_1 = 2.10$ mm, $l_1 = 18.95$ mm, $w_2 = 0.44$ mm, $l_2 = 19.69$ mm, $w_3 = 3.15$ mm, $l_3 = 18.09$ mm, $w_4 = 0.33$ mm, and $l_4 = 19.88$ mm.

As was shown by investigations, increasing the jump of the wave resistances of the microstrip lines in models of band-pass superlattice filters, one can reduce the relative width of their pass band to $\frac{\Delta f_3}{f_0} = 1\%$. Necessary large jumps of wave resistances can be obtained by using composite (hybrid) substrates of different materials with high and low permittivities for the low- and high-ohmic segments of transmission lines, respectively.

Investigations also show that an increase in the number of segments leads to an almost exponential increase

Parameters of microstrip segments for lattice filters whose first pass bands have relative widths of 40 and 60%

Layer no.	$\frac{\Delta f_3}{f_0}$, %	w, mm	l, mm	ε_{eff}	$\frac{Z_N}{Z_0}$
1 (7)	40	3.92	17.19	7.58	0.43
	60	2.47	17.62	7.22	0.59
2 (6)	40	0.10	20.49	5.94	2.16
	60	0.50	19.66	6.32	1.33
3 (5)	40	6.44	17.14	8.00	0.29
	60	3.54	17.78	7.50	0.46
4	40	0.05	20.69	5.84	2.52
	60	0.36	19.92	6.22	1.49

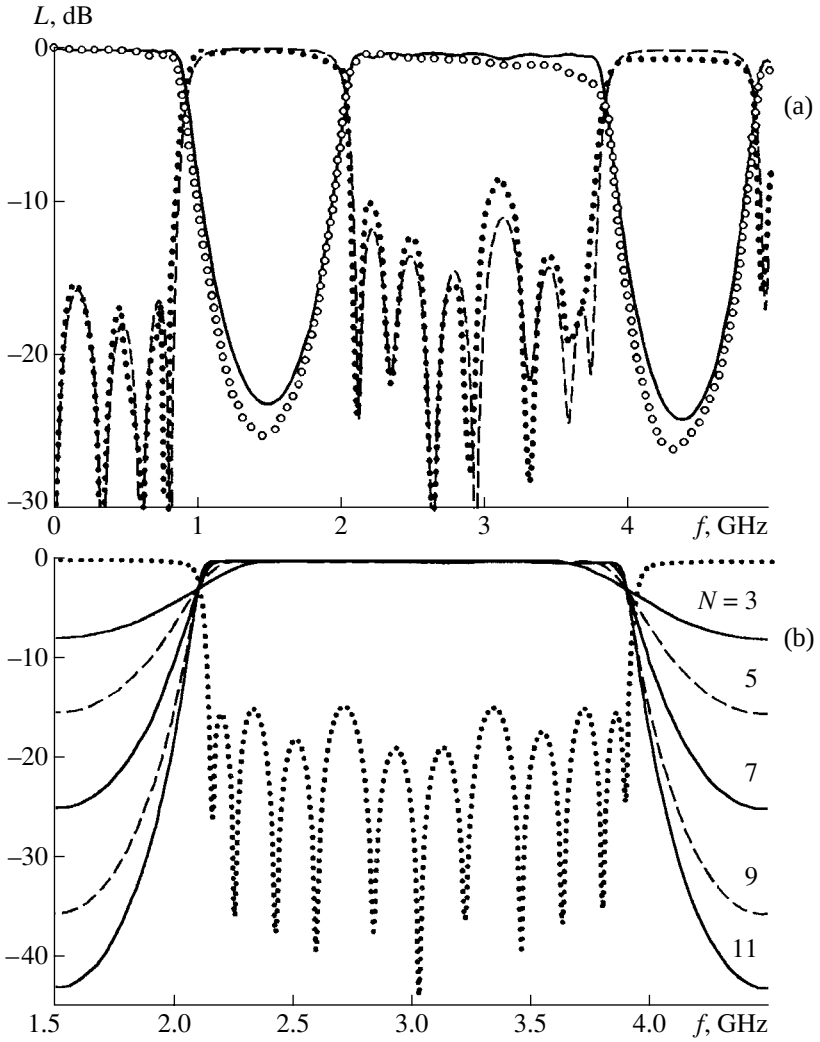

Fig. 4. Frequency responses of microstrip models of filters for the (a) seven-layer superlattice (lines are calculations, points are experimental data) and (b) superlattice with 3–11 layers (points are reflection losses for the 11-layer filter).

in damping in the stop bands as well as to an increase in the slopes of the frequency response. This statement is corroborated in Fig. 4b, which shows the frequency response of alumina substrate filters that have a pass-band width of $\frac{\Delta f_3}{f_0}$ = 60% and consist of 3–11 segments. It is seen that each addition of two segments to the construction under consideration leads to an increase in damping in the stop bands to the left and right of the pass band by almost 10 dB. It is worth noting that damping in the stop bands increases strongly with a decrease in the width of the pass band of the device.

CONCLUSIONS

The proposed microstrip model is a close analogue of a superlattice consisting of alternating layers with different permittivities. Due to good agreement of the quasistatic numerical analysis of the model with experiment, the construction parameters of a band-pass filter on a superlattice with given characteristics can be obtained. Since microstrip structures are simple to produce and cheap, a device can be preliminary checked experimentally in the chosen UHF band.

Investigations show that a superlattice even with a comparatively small number of layers can serve as a good band-pass filter under three conditions. First, the necessary jump must be ensured between the wave resistances of the outer layers of the superlattice and the wave resistances of the entry and exit. The jump value is determined by a given pass band of the device. Second, it is necessary to balance couplings between the layers in the superlattice by choosing their permittivities. These couplings must also correspond to the given pass band. Third, the natural frequencies of all layers serving as resonators must coincide with the central frequency of the pass band. The proposed approach can

obviously be used to model optical mirrors and photonic crystals.

REFERENCES

1. P. M. Levy, Solid State Phys. **47**, 367 (1994).
2. Masataka Shirasaki, Hiroshika Nakajima, Takeshi Obokata, and Kunihjko Asama, Appl. Opt. **21**, 4229 (1982).
3. N. A. Feoktistov and L. E. Morozova, Pis'ma Zh. Tekh. Fiz. **20** (5), 12 (1994) [Tech. Phys. Lett. **20**, 180 (1994)].
4. E. Yablonovitch, Phys. Rev. Lett. **58**, 2059 (1987).
5. S. Ya. Vetrov and A. V. Shabanov, Zh. Éksp. Teor. Fiz. **120**, 1126 (2001) [JETP **93**, 977 (2001)].
6. Yu. I. Bespyatykh, I. E. Dikshteĭn, V. P. Mal'tsev, and W. Wasilewski, Fiz. Tverd. Tela (St. Petersburg) **45**, 2056 (2003) [Phys. Solid State **45**, 311 (2003)].
7. V. I. Gvozdev and E. I. Nefedov, *3-Dimensional Integral Microwave Circuits* (Nauka, Moscow, 1985) [in Russian].
8. B. A. Belyaev, A. V. Kazakov, A. A. Leksikov, and I. Ya. Makievskiĭ, Prib. Tekh. Éksp., No. 1, 167 (1998).

Translated by R. Tyapaev

Doklady Physics, Vol. 49, No. 4, 2004, pp. 218–221. Translated from Doklady Akademii Nauk, Vol. 395, No. 5, 2004, pp. 609–613.

TECHNICAL PHYSICS

Thermal-Radiation Study of the Kinetics of the Elastic–Plastic Deformation and Fracture of Construction Elements with Stress Concentrators

A. M. Ivanov*, E. S. Lukin, and Academician V. P. Larionov

Received December 19, 2003

A single loading of construction elements with stress concentrators is characterized by elastic–plastic deformation, development of plastic zones, and final fracture. Data on the kinetics of elastic–plastic deformation and the character of fracture under stress concentration can be used to estimate the strength and bearing strength of construction elements with stress concentrators. The appearance and development of elastic–plastic deformations in stress-concentration zones lead to both the redistribution of stresses and change in the temperature of a material.

In this work, deformation, stages of the development of plastic deformation zones, and fracture of metals under stress concentration are studied by the thermal radiation method based on analysis of the change in the temperature of a specimen.

Virtually all physical processes in loaded materials (phase transformations, plastic deformation, fracture, etc.) are accompanied by the release or absorption of heat. Study of the deformation and fracture of materials by recording thermograms and measuring temperature is based on the thermal effect accompanying deformation processes. Thermal effects accompanying elastic and plastic deformations have been known since the 1850s. Heating and cooling of elastic bodies under loading were described and then experimentally studied by W. Thompson (Lord Kelvin) in 1855. More recently, variation in temperature under mechanical loading was experimentally detected by J.P. Joule (1857), H. Hort *et al.* (1907), E. Rasch (1908), A. Nadai (1911), and others. Brief descriptions of these experiments can be found in [1]. Temperature variation accompanying deformation processes in solids is studied by thermoelectric, calorimetric, and thermovision methods.

Institute of Physico-Engineering Problems of the North, Siberian Division, Russian Academy of Sciences, ul. Oktyabr'skaya 1, Yakutsk, 677891 Russia

** e-mail: a.m.ivanov@iptpn.ysn.ru*

Cooling and heating of a metal are observed under elastic tension and compression, respectively. The transition to the plastic deformation stage is accompanied by the appearance of irreversible plastic deformations as well as by the release and dissipation of energy in the form of heat [1–15].

Mechanisms responsible for radiation accompanying the deformation and fracture of specimens of metals and alloys under various loading types were explained in [5–7]. In addition, the appearance of infrared and visible radiation under the deformation and fracture of metals was discovered, and the mechanism of the emission of these types of radiation was explained.

Methods were developed for (i) obtaining temperature distribution over a specimen [8, 9], (ii) estimating the inhomogeneity of stress distribution in the stress-concentration zone [10, 11], (iii) analyzing stress fields [12], (iv) determining both the specific work of the fracture of a specimen with a crack and the stress intensity coefficient [13], and (v) analyzing the kinetics of the deformation and fracture of materials by the thermal radiation method [14]. Temperature was measured by thermocouples and thermovision instruments. Thermovision methods are also applied in practice for nondestructive testing of various objects, including large metallic constructions of lifting machines [11], for the detection of defects in construction elements [15], etc.

The kinetics of both deformation and limiting state of construction materials (metals and their alloys) was experimentally studied in [14] under the conditions of homogeneous stress–strain state by the thermal radiation method.

As is known, plastic deformations are localized in the stress-concentration zone arising due to a natural defect or an artificial stress concentrator. Thermal radiation in the regions of the development of plastic deformations is more intense than radiation in the other part of the specimen and is maximal at the fracture of the specimen. This circumstance, along with the time dependence of the thermal process corresponding to deformation, stimulates the study of the kinetics of the elastic–plastic deformation and fracture of construction

1028-3358/04/4904-0218$26.00

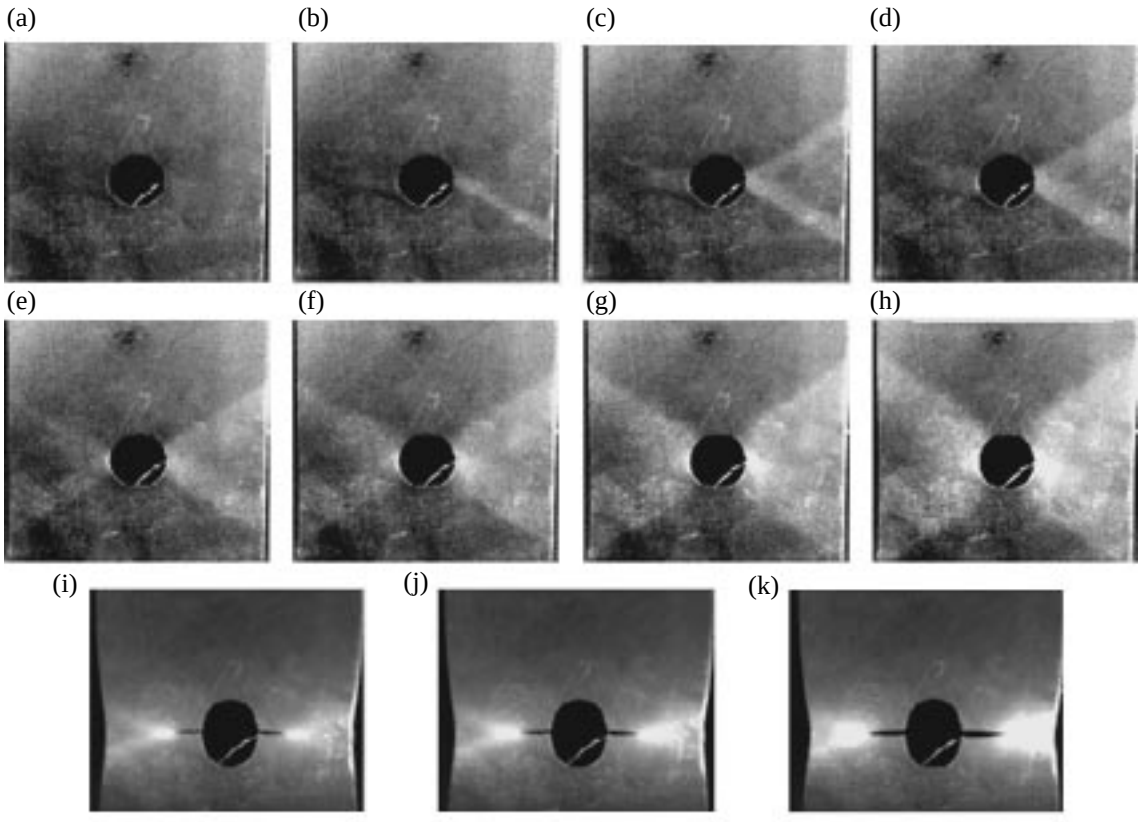

Fig. 1. Thermograms of a plane 10kp5-steel specimen with a circle hole for δ = (a–h) 1–3.1% and (i–k) 6.8–7.3%.

elements with stress concentrators by instruments detecting thermal radiation.

The kinetics of the deformation and fracture of specimens with geometric stress concentrators was experimentally studied by the TKVr–IFP thermovision system developed at the Institute of Semiconductor Physics, Siberian Division, Russian Academy of Sciences (Novosibirsk). Its limiting sensitivity is equal to ±0.03 K, measured temperature range is 293–318 K, spatial resolution is no worse than 0.3–0.4 mm per pixel, recording rate is equal to 20 fps, and the characteristic working wavelength lies in the range 2.8–3.05 μm. It provides analysis of thermograms, etc. [15]. The stages of the development of deformations were analyzed on thermograms and temperature plot along with the tension diagram. The scheme of thermovision measurements provided the maximum possible spatial resolution.

During experiments, static thermograms were obtained and on-line analysis was carried out with the representation of the thermal images of specimens on a computer monitor. Individual thermograms and thermofilms were conserved in the file form. Computer analysis of thermograms included the following functions: (i) on-line observation of a color or black-and-white thermal image on the computer monitor, (ii) measurement of temperature at any point of a frame, (iii) representation of the temperature distribution along the horizontal and vertical lines of the frame, (iv) representation of the time dependence of temperature at a chosen point on the thermogram (in the thermofilm regime), and (v) detection of time variations in maximum T_{max}, minimum T_{min}, and average T_{av} temperatures of the chosen part of the specimen surface.

Uniaxial tensile tests of specimens were carried out on an Instron-1195 universal testing machine at room temperature under loading rates ensuring the adiabaticity of the deformation process. To analyze the effect of the stress concentration on change in the temperature regime, we tested the following specimens with stress concentrators: cylindrical metallic (technical copper) specimens with a ring neck and 10kp5-steel plane specimens with central circle holes. The kinetics of the temperature (plastic-deformation) field at the stage of the elastic–plastic deformation of a specimen with a stress concentrator can be described by analyzing the patterns of infrared radiation (Fig. 1) and variation in its temperature regime (Figs. 2–4).

As an example, Fig. 1 shows a set of thermograms of a 230 × 100 × 1.6-mm 10kp5-steel specimen with a hole 22 mm in diameter for δ = (a–h) 1–3.1% and (i–k) 6.8–7.3%. These thermograms were obtained under the uniaxial tension of the specimen with a rate of 0.83 mm/s. As is seen in Fig. 1, thermograms reflect

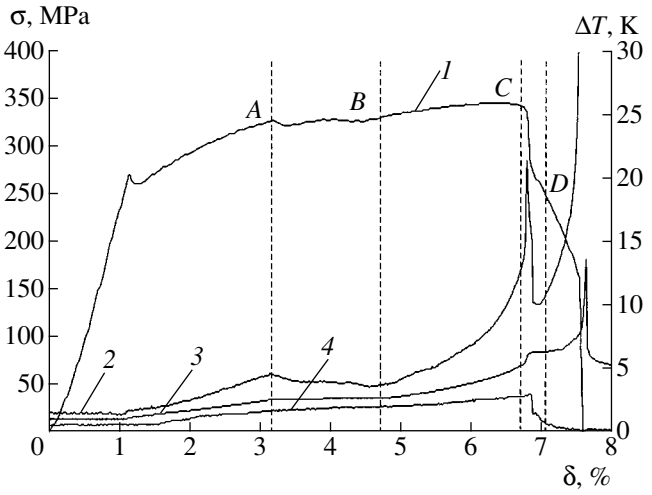

Fig. 2. (*1*) Stress–strain curve for a plane 10kp5-steel specimen with a circle hole; strain dependence of the (*2*) maximum, (*3*) average, and (*4*) minimum temperatures in the working part of the specimen.

the development of plastic deformations. The thermogram in Fig. 1a corresponds to the elastic deformation stage, and the thermograms in Figs. 1b–1h, to various degrees of the development of plastic deformations in the sample. The development of slip bands is seen on both sides of the stress concentrator. The thermograms in Figs. 1i–1k were obtained after the appearance of cracks on both sides of the hole. The development of plastic deformation zones is seen at the crack apices.

Figure 2 shows the stress–strain curve for a specimen with a hole along with variations of the maximum, average, and minimum temperatures measured in a chosen working part of the specimen. The stress–strain curve plots the normal stress σ in the minimum cross-section versus the specimen strain (relative elongation) δ. The processes of deformation and fracture are reflected most completely and reliably by variation in the maximum temperature of the specimen. Analyzing both the strain dependence of the temperature of the construction element with the hole and changes in the thermograms, we draw the following conclusions. In the elastic region, temperature decreases by 0.08 K on average (Fig. 2). Temperature first begins to increase at stress σ = 255 MPa, which corresponds to the onset of the local plastic flow of a material near the hole. The monotonic increase in temperature up to the point *A* on the stress–strain curve (σ = 261–327 MPa, δ = 1.1–3.2%) corresponds to the development of plastic deformations that terminates with the envelopment of the dangerous cross section by a plastic flow. Thermograms exhibit Chernov–Luders slip bands that reach the lateral surface of the plate at an angle of 45°. In the *AB* interval (δ = 3.2–4.7%), plastic deformations propagate further through the basic part of a specimen. At this stage, the relaxation of the nominal stresses is observed, and temperature decreases due to the unloading of the material along the dangerous cross section. The further considerable increase in temperature in the *BC* interval up to the maximum stress corresponds to the relative elongation δ = 4.7–6.7%, at which the intense development of plastic deformations, as well as the contraction of the material, occurs. Then, when cracks appear on both sides of the hole, temperature increases abruptly by ΔT = 21.5 K. Each crack grows up to 7 mm. A thermal pulse (abrupt temperature increase) at δ = 6.8%, which was detected at the stage

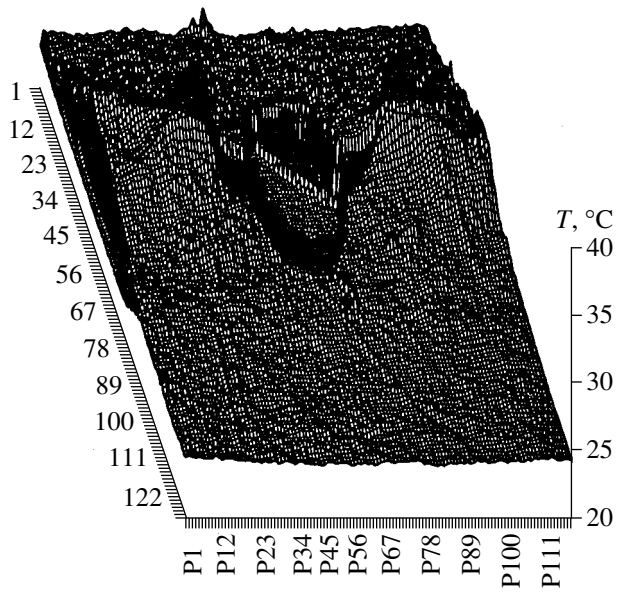

Fig. 3. Three-dimensional plot of the temperature field of the plane 10kp5-steel specimen with the circle hole for σ = 248 MPa and δ = 7%.

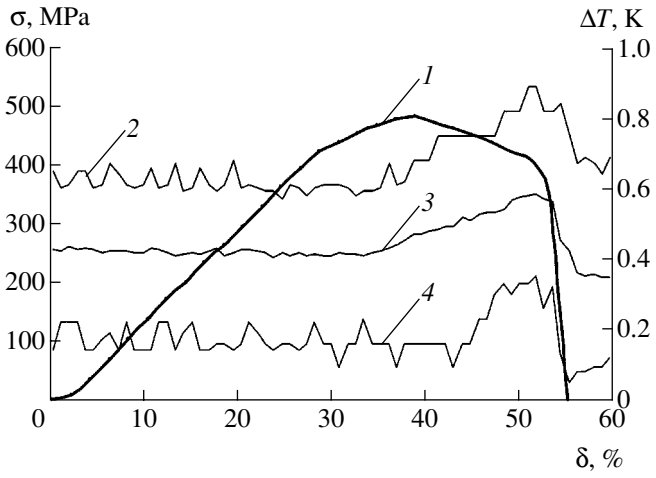

Fig. 4. (*1*) Stress–strain curve for a cylindrical copper specimen with a ring neck; strain dependence of the (*2*) maximum, (*3*) average, and (*4*) minimum temperatures near the stress concentrator.

of the pre-fracture (preceding the complete fracture) of the 10kp5-steel specimen with the circle hole, characterizes the appearance of a crack on the contour of the hole. The propagation of the main crack (complete fracture of the specimen) is accompanied by considerable heat release. The appearance of two thermal pulses is associated with the viscous fracture of the specimen with the concentrator.

As an example, Fig. 3 shows the three-dimensional plot (isometry) of the temperature field over the surface of the 10kp5-steel specimen with the hole. The plot was obtained using Microsoft Excel and corresponds to the stage when cracks are present on both sides of the hole (Fig. 2, point *D* in line *1*).

The kinetics of the temperature field in the technical-copper specimen with the neck differs from kinetics for steel specimens with holes and is determined by the physical and mechanical properties of copper. The strain dependence of the temperature of the copper specimen with the ring neck (88 mm in length, 10.3 mm in diameter, with a neck radius of 2.5 mm) is shown in Fig. 4. It reflects the deformation process in a material with high plasticity and thermal conductivity under the stress-concentration conditions. The loading rate was equal to 0.83 mm/s. The thermal process is concentrated in the neck region. Due to high thermal conductivity, temperature decreases slightly at the elastic deformation stage. Under plastic flow conditions and development of plastic deformations, temperature increases monotonically up to the fracture of the specimen.

Thus, experimental procedures based on the detection of thermograms by a thermovision instrument and further analysis of thermograms and variation in the temperature of a specimen under deformation can be successfully applied to study the kinetics of deformation in the inhomogeneous stress–strain state. The difference in the character of the deformation and fracture of construction elements that include stress concentrators and are made of different materials is manifested on thermograms and the plot of temperature variation. Nonmonotonic variation in the temperature of 10kp5-steel specimens at the deformation stage from the onset of local plastic flow to the fracture of the material in the stress concentration zone reflects the dynamics of the development of plastic deformations over a specimen. The observed temperature decrease corresponding to the relaxation of nominal stresses is associated with the unloading of the material in the dangerous cross section due to the propagation of plastic deformations over the basic part of the specimen. A thermal pulse (abrupt temperature increase) detected at the pre-fracture stage for steel specimens with stress concentrators corresponds to the appearance of a crack and is determined by the elastic compression of the material under the rapid unloading of the specimen due to the formation of new surfaces. The plastic-flow onset, appearance of the Chernov–Luders bands, localization of the plastic flow in the stress-concentration zone, and the contraction of the material near the concentrator are identified by bends, whereas the appearance of a crack and the fracture of the specimen, by sharp peaks in the temperature curves.

ACKNOWLEDGMENTS

This work was supported in part by the Russian Foundation for Basic Research (project no. 03-01-96065r2003arktika) and the Program for Basic Research, Division of Power and Mechanical Engineering, Mechanics, and Control Processes, Russian Academy of Sciences (project no. 3.11.4).

REFERENCES

1. A. Nadai, *Theory of Flow and Fracture of Solid* (McGraw-Hill, New York, 1963; Mir, Moscow, 1969), Vol. 2.
2. J. C. Erdmann and J. A. Jahoda, Appl. Phys. Lett. **4**, 204 (1964).
3. Y. Nakada, Philos. Mag. **11**, 251 (1965).
4. Ya. B. Fridman, *Mechanical Properties of Metals: Deformation and Destruction* (Mashinostroenie, Moscow, 1974), Part 1.
5. A. A. Tupik, N. P. Valuev, and B. V. Manegin, Dokl. Akad. Nauk **272**, 858 (1983) [Sov. Phys. Dokl. **28**, 890 (1983)].
6. K. B. Abramova, B. P. Peregud, and I. P. Shcherbakov, Zh. Tekh. Fiz. **60** (4), 159 (1990) [Sov. Phys. Tech. Phys. **35**, 497 (1990)].
7. G. V. Mikhaĭlova, B. K. Zuev, N. P. Novikov, *et al.*, Dokl. Akad. Nauk **295**, 1324 (1987) [Sov. Phys. Dokl. **32**, 643 (1987)].
8. W. Dahl and P. Belhe, in *Static Strength and Mechanics of Steel Fracture: Collection of Scientific Works* (Metallurgiya, Moscow, 1986) (translated from German), pp. 51–133.
9. M. M. Krishtal, Metalloved. Term. Obrab. Met., No. 4, 27 (2003).
10. V. Ya. Bash, *Thermoelectric Studies of Stress and Strain* (Naukova Dumka, Kiev, 1984).
11. V. N. Pustovoĭ, *Noncontact Method of Studying Stress Concentration in Metal Constructions of Elevators* (VO Mortekhinformreklama, Moscow, 1991).
12. D. Oliver, in *Handbook of Experimental Mechanics*, Ed. by A. S. Kobayashi (Prentice-Hall, Eagle Wood Cliffs, 1987; Mir, Moscow, 1990), Vol. 2, pp. 113–123.
13. V. E. Remorov, Zavod. Lab., No. 5, 27 (1992).
14. A. M. Ivanov, E. S. Lukin, and V. P. Larionov, Dokl. Akad. Nauk **384**, 469 (2002) [Dokl. Phys. **47**, 454 (2002)].
15. E. S. Lukin, A. M. Ivanov, and B. G. Vaĭner, Defektoskopiya, No. 6, 70 (2003).

Translated by R. Tyapaev

Doklady Physics, Vol. 49, No. 4, 2004, pp. 222–225. Translated from Doklady Akademii Nauk, Vol. 395, No. 4, 2004, pp. 470–473.

MECHANICS

Axisymmetric Hertz Problem with Tangential Displacements on the Contact Surface

I. I. Argatov

Presented by Academician N.F. Morozov November 27, 2003

Received December 10, 2003

The Hertz contact problem in a more precise formulation is analyzed and, under certain assumptions, reduced to a system of two integral equations with asymmetric kernels. An approximate solution is obtained in a closed form.

1. HERTZ PROBLEM IN A MORE PRECISE FORMULATION

Let elastic bodies Ω_1 and Ω_2 in undeformed states touch each other at the point O near which the surfaces in contact are specified by the equations

$$z_i = (2R_i)^{-1}r^2, \quad i = 1, 2,$$

where R_i is the curvature radius of the surface of the body Ω_i at the point O. Let δ_0 be the approach of the bodies Ω_1 and Ω_2 compressed by oppositely directed forces each of magnitude P.

We consider two points, M_1 and M_2, on the front surfaces of the bodies Ω_1 and Ω_2. The point M_i is shifted under deformation by $u_r^i(r_i)$ and $w_i(r_i)$ in the radial and vertical directions, respectively. The conditions of compatibility of displacements have the form [1]

$$r_1 + u_r^1 = r_2 + u_r^2, \quad z_1 + w_1 = -(z_2 + w_2) + \delta_0. \quad (1.1)$$

These equalities must be satisfied for $0 \le r_i \le a_i$, where $i = 1$ and 2 and a_1 and a_2 are the radii corresponding to the points M_1 and M_2 at the edge of the contact area. In this case, the radius of the contact area ω is determined from the relation

$$a = a_1 + u_r^1(a_1) = a_2 + u_r^2(a_2). \quad (1.2)$$

The displacements of the points of the elastic bodies near the contact area are expressed in terms of the solution of the Boussinesq problem as

$$w_i(r_i) = \theta_i \iint\limits_{\omega_i} \frac{p_i(\rho)\rho\, d\rho\, d\varphi}{\sqrt{r_i^2 + \rho^2 - 2r_i\rho\cos\varphi}}, \quad \theta_i = \frac{1-\nu_i^2}{\pi E_i}; \quad (1.3)$$

$$u_r^i(r_i) = -\theta_i^\vee \iint\limits_{\omega_i} \frac{p_i(\rho)(r_i - \rho\cos\varphi)}{r_i^2 + \rho^2 - 2r_i\rho\cos\varphi}\rho\, d\rho\, d\varphi, \quad \theta_i^\vee = \frac{(1+\nu_i)(1-2\nu_i)}{2\pi E_i}. \quad (1.4)$$

Here, $i = 1$ and 2, ω_i is a circle with the radius a_i (prototype of the contact area for the body Ω_i), and $p_i(r_i)$ is the density of generalized contact pressures.

According to the static equilibrium equation,

$$2\pi \int\limits_0^{a_i} p_i(\rho)\rho\, d\rho = P \quad i = 1, 2. \quad (1.5)$$

Expressing radii r_1 and r_2 from the first of Eqs. (1.1) and using the second of Eqs. (1.1), we arrive at the linearized equations

$$w_1(r_1) + w_2(r_2) = \delta_0 - \frac{r_i^2}{2R} + (-1)^i \frac{r_i}{R_{3-i}}(u_r^1(r_1) - u_r^2(r_2)), \quad i = 1, 2, \quad (1.6)$$

where $R^{-1} = R_1^{-1} + R_2^{-1}$ is the total curvature. To simplify system (1.6), Galanov [2] proposed the assumption

$$\theta_2^{-1}w_2(r_2) \approx k\theta_1^{-1}w_1(r_1), \quad (\theta_2^\vee)^{-1}u_r(r_2) \approx k(\theta_1^\vee)^{-1}u_r(r_1), \quad (1.7)$$

where k is a certain constant. The adequacy of hypothesis (1.7) was numerically checked in [2]. In view of

Admiral Makarov State Maritime Academy, Kosaya liniya 15-A, St. Petersburg, 199026 Russia
e-mail: argatov@home.ru

1028-3358/04/4904-0222$26.00 © 2004 MAIK “Nauka/Interperiodica”

relations (1.7), system (1.6) takes the form

$$\Theta_i(B_i p_i)(r_i) = \delta_0 - \frac{r_i^2}{2R} + (-1)^{i+1}\frac{r_i}{R_{3-i}}\Theta_i^\vee(B_i^\vee p_i)(r_i). \quad (1.8)$$

Here, $\Theta_i = \theta_i + k^{-1}\theta_{3-i}$, $\Theta_i^\vee = (-1)^{i+1}(\theta_i^\vee - k^{-1}\theta_{3-i}^\vee)$, and B_i and $B_i^\vee$ are integral operators in formulas (1.3) and (1.4). The contact area is determined from the condition that the contact pressures are positive; i.e., $p_i(r_i) > 0$ for $0 \le r_i < a_i$ and $p_i(a_i) = 0$.

To determine the contact pressure densities $p_1(r_1)$ and $p_2(r_2)$, radii a_1 and a_2, approach δ_0 of the elastic bodies, and auxiliary parameter k under a given contact force P, Galanov [2] proposed an algorithm based on the numerical method developed in [3]. In [4], a solution was obtained by a numerical method where integral operators were approximated by finite sums. The two-dimensional contact problem in a more precise formulation was analyzed analytically in [5]. An approach based on the theory of variational inequalities was developed in [6, Section 2.3] for models of plates and shells with contact conditions similar to Eq. (1.8).

Equations (1.6) were derived by disregarding the term $(2R_2)^{-1}(u_r^1(r_1) - u_r^2(r_2))^2$ and retaining the term $(2R_2)^{-1}(u_r^1(r_1) - u_r^2(r_2))r_1$, which provides a correction to the Hertz theory. Since

$$u_r^i(r_i) = -\theta_i^\vee(B_i^\vee p_i)(r_i),$$
$$(B_i^\vee p_i)(r_i) = \frac{2\pi}{r_i}\int_0^{r_i} p_i(\rho)\rho\, d\rho, \quad (1.9)$$

we obtain the estimate $|u_r^i| < \theta_i^\vee \pi a_i p_{i0}$, where p_{i0} is the maximum of the density $p_i(r_i)$. Determining p_{i0} from the Hertz theory, we conclude that the tangential displacements $u_r^i(r_i)$ (up to a factor depending on the ratio of the elastic constants) is less than the approach δ_0. Thus, the correction terms are equal to about $\delta_0^{3/2}R^{-1/2}$, because the radius a_i of the contact area is equal to about $\sqrt{\delta_0 R}$, and the rejected terms are equal to about $\delta_0^2 R^{-1}$; i.e., the relative error of the linearized condition of displacement compatibility is equal to about $\frac{\delta_0}{R}$.

2. APPROXIMATE SOLUTION OF THE REFINED CONTACT PROBLEM

The general solution of the axisymmetric contact problem has the form [7–9]

$$p_i(r_i) = -\frac{1}{\pi}\int_{r_i}^{a_i}\frac{F_i'(s)}{\sqrt{s^2 - r_i^2}}ds, \quad F_i(a_i) = 0, \quad (2.1)$$

where, in view of Eqs. (1.8) and (1.9),

$$\pi\Theta_i F_i(r_i) = \delta_0 - \frac{r_i^2}{R} + (-1)^{i+1}\Theta_1^\vee\frac{2\pi r_i}{R_{3-i}}\int_0^{r_i}\frac{p_i(s)s}{\sqrt{r_i^2 - s^2}}ds. \quad (2.2)$$

Substituting expression (2.2) into the first of Eqs. (2.1) for $r_i = 0$, we express the maximum of the contact pressures as

$$\pi\Theta_i p_i(0) = \frac{2a_i}{\pi R} + (-1)^i\frac{2\Theta_1^\vee}{R_{3-i}}\int_0^{a_i} p_i(t)\left(\arccos\frac{t}{a_i} + \frac{t}{\sqrt{a_i^2 - t^2}}\right)dt, \quad (2.3)$$

where $i = 1$ and 2. According to the Hertz theory [10], the pressure on the contact area is equal to

$$p_i(r_i) = p_{0i}\sqrt{1 - \frac{r_i^2}{a_i^2}}, \quad i = 1, 2, \quad (2.4)$$

where p_{i0} is the maximum of the contact pressures. Substituting densities (2.4) into the right-hand side of Eqs. (2.3) and omitting the terms of the order of $\left(\frac{a_i}{R}\right)^2$, we obtain

$$p_{i0} = \frac{2a_i}{\pi^2\Theta_i R}\left\{1 + (-1)^i\left(\frac{\pi^2}{4} + 2\right)\frac{\Theta_i^\vee a_i}{\pi(\theta_1 + k\theta_2)R_{3-i}}\right\}, \quad i = 1, 2. \quad (2.5)$$

In view of Eqs. (2.2) and (2.4), the second of Eqs. (2.1) takes the form

$$\delta_0 = \frac{a_i^2}{R} - (-1)^i\pi a_i^2 p_{i0}\frac{\Theta_i^\vee}{R_{3-i}}, \quad i = 1, 2. \quad (2.6)$$

Disregarding quantities of the order of $O\left(\frac{\delta_0}{R}\right)$ and tak-

ing into account Eq. (2.5), from Eq. (2.6), we obtain

$$a_i = \sqrt{\delta_0 R}\left(1 + (-1)^{i+1}\frac{\Theta_i^\vee}{\pi\Theta_i}\frac{\sqrt{\delta_0 R}}{R_{3-i}}\right), \quad i = 1, 2. \quad (2.7)$$

Then, using the Mossakovskiĭ theorem [11], from Eq. (1.8), we derive

$$\pi\Theta_i P = \frac{4a_i^3}{3R} + (-1)^i\frac{4\pi\Theta_i^\vee}{kR_{3-i}}\int_0^{a_i}\frac{p_i(t)t^3}{\sqrt{a_i^2 - t^2}}dt, \quad i = 1, 2. \quad (2.8)$$

Substituting Hertz density (2.4) with p_{i0} specified by Eq. (2.5) and a_i specified by Eq. (2.7) into Eq. (2.8), we express the force P in terms of the displacement δ_0 as

$$P = \frac{4\delta_0^{3/2}\sqrt{R}}{3\pi\Theta_i}\left\{1 + (-1)^{i+1}\frac{3\Theta_i^\vee}{2\pi\Theta_i}\frac{\sqrt{\delta_0 R}}{R_{3-i}}\right\}, \quad i = 1, 2. \quad (2.9)$$

Equating the right-hand sides of expressions (2.9), we obtain

$$k = 1 + \frac{3}{2\pi}\frac{(\theta_1^\vee - \theta_2^\vee)}{(\theta_1 + \theta_2)}\sqrt{\frac{\delta_0}{R}}. \quad (2.10)$$

Substitution of expression (2.10) into Eq. (2.9) yields

$$P = \frac{4\delta_0^{3/2}\sqrt{R}}{3\pi(\theta_1 + \theta_2)} \times\left\{1 + \frac{3(\theta_1^\vee - \theta_2^\vee)}{2\pi(\theta_1 + \theta_2)^2}\frac{(R_1\theta_1 - R_2\theta_2)}{R_1 + R_2}\sqrt{\frac{\delta_0}{R}}\right\}. \quad (2.11)$$

Let us briefly discuss the problem that concerns the more accurate determination of the maximum tangential stresses at the Dinnik point, which is important for the mechanics of contact fracture [12]. According to the Huber solution (see, e.g., [12]), stresses in an elastic half-space whose boundary is subjected to the action of a ball indenter, which transmits normal pressure (2.4), are given by the expressions $\sigma_{ij} = p_a\psi_{ij}(r, z)$, where the dimensionless functions $\psi_{ij}(r, z)$ of the coordinates depend parametrically on the Poisson ratio and

$$p_a = P(\pi a^2)^{-1} \quad (2.12)$$

is the average normal pressure. Setting $\theta_2 = \theta_2^\vee = 0$, $R_1 = \infty$, and $R_2 = R$ in Eqs. (2.7) and (2.11), we obtain

$$a = \sqrt{\delta_0 R}\left(1 + \frac{\alpha}{2\pi}\sqrt{\frac{\delta_0}{R}}\right), \quad P = \frac{4E\sqrt{R}}{3(1-\nu^2)}\delta_0^{3/2}\left(1 + \frac{3\alpha}{4\pi}\sqrt{\frac{\delta_0}{R}}\right). \quad (2.13)$$

Substitution of Eqs. (2.13) into Eq. (2.12) yields

$$p_a = \frac{2E}{\pi(1-\nu^2)}\sqrt{\delta_0 R}\left(1 - \frac{\alpha}{4\pi}\sqrt{\frac{\delta_0}{R}}\right). \quad (2.14)$$

Thus, more accurate calculation by using Eq. (2.14) yields somewhat lower stress in the contact area. This decrease can be disregarded in most strength calculations.

3. REFINED THEORY OF THE AXISYMMETRIC QUASISTATIC COLLISION OF ELASTIC BODIES

We consider the problem of the direct central collision of two elastic bodies Ω_1 and Ω_2 with the respective masses m_1 and m_2 (see, e.g., [13, Section 1.1]). It is described by the equation

$$M_0\ddot{\delta}_0 = -P(t), \quad \delta_0(0) = 0, \quad \dot{\delta}_0 = v_0; \quad M_0 = \frac{m_1 m_2}{m_1 + m_2}, \quad (3.1)$$

where v_0 is the initial relative velocity. In this case, according to Eq. (2.11), we have

$$P = K\delta_0^{3/2} + k\delta_0^2, \quad K = \frac{4\sqrt{R}}{3\pi(\theta_1 + \theta_2)}, \quad k = \frac{2(\theta_1^\vee - \theta_2^\vee)(R_1\theta_1 - R_2\theta_2)}{\pi^2(\theta_1 + \theta_2)^3(R_1 + R_2)}. \quad (3.2)$$

Equation (3.1) has the energy integral

$$\frac{M_0\dot{\delta}_0^2}{2} - \frac{M_0 v_0^2}{2} = -\frac{2}{5}K\delta_0^{5/2} - \frac{1}{3}k\delta_0^3. \quad (3.3)$$

Setting $\dot{\delta}_0 = 0$, we arrive at the equation

$$\frac{M_0 v_0^2}{2} = \frac{2}{5}K\delta_{0m}^{5/2} + \frac{1}{3}k\delta_{0m}^3 \quad (3.4)$$

for maximum approach δ_{0m}. Expressing the relative velocity $\dot{\delta}_0$ from Eq. (3.3), we determine the collision time

$$T = \frac{2\delta_{0m}}{v_0}\int_0^1\left(1 - \eta^{5/2}\frac{(1 + \kappa\eta^{1/2})}{1 + \kappa}\right)^{-1/2}d\eta, \quad \kappa = \frac{5k}{6K}\sqrt{\delta_{0m}}. \quad (3.5)$$

Disregarding quantities of the order of κ^2, from

Eq. (3.4), we obtain

$$\delta_{0m} = \delta_{0m}^{H}\left(1-\frac{2}{5}\kappa_0\right), \quad \delta_{0m}^{H} = \left(\frac{5M_0v_0^2}{4K}\right)^{2/5}, \qquad \kappa_0 = \frac{5k}{6K}\sqrt{\delta_{0m}^{H}}. \tag{3.6}$$

In view of Eq. (3.6), the maximum contact force is determined from formula (3.2) as

$$P_m = P_m^{H}\left(1+\frac{3}{5}\kappa_0\right), \quad P_m^{H} = K^{2/5}\left(\frac{5}{4}M_0v_0^2\right)^{3/5}. \tag{3.7}$$

Approximate calculation of integral (3.5) yields the collision time in the form

$$T = T_H\left(1-\frac{3I_1}{5I_0}\kappa_0\right), \quad T_H = \left(\frac{5M_0}{4K\sqrt{v_0}}\right)^{2/5}I_0, \tag{3.8}$$

where

$$I_0 = \int_0^1 \frac{d\eta}{\sqrt{1-\eta^{5/2}}} = \frac{2\sqrt{\pi}\Gamma(2/5)}{5\Gamma(9/10)},$$

$$I_1 = \int_0^1 \frac{\eta^{1/2}d\eta}{\sqrt{1-\eta^{5/2}}} = \frac{4\sqrt{\pi}\Gamma(3/5)}{\Gamma(1/10)}.$$

Relation (3.3) characterizes the transformation of the initial kinetic energy of colliding bodies to the potential energy of deformation. Therefore, the parameter κ_0 is primarily the relative increment of the potential energy at the time $t = \frac{T}{2}$. This increment is due to the inclusion of tangential displacements. According to Eq. (3.4), $\delta_{0m} < \delta_{0m}^{H}$ ($\delta_{0m} > \delta_{0m}^{H}$) if the parameter k is positive (negative). It is easy to show that $T < T_H$ ($T > T_H$), where T_H is the collision time according to the Hertz theory, if $\kappa > 0$ ($-1 < \kappa < 0$).

An asymptotic model of a quasistatic direct impact of a rigid ball on the plane boundary of an elastic body was developed in [14], including the integral correction for the shape of the body. The refined theory of collision of elastic balls was given in [13, Chapter 3, Section 5] with the approximate inclusion of the global deformation of the balls, as well as the local deformation in the contact area. It is worth noting that the leading terms of equations that were derived in [13, 14] and determine the contact force as a function of the approach between bodies are similar to Eqs. (3.2). At the same time, according to the theory [15] refining the shape of the elastic body in the contact area, the contact force is given by the expression $P = K\delta_0^{3/2} + k\delta_0^{5/2}$. Thus, the above effects must be manifested earlier than those discussed in [15]. At the same time, comparison with results obtained in [14] shows that, in the problem of the impact of an absolutely rigid ball on an elastic layer whose thickness is equal to the ball radius, the effect of the tangential displacement is weaker than the effect of finite thickness of the elastic layer by one order of magnitude and both effects reduce the impact time.

ACKNOWLEDGMENTS

This work was supported by the Council of the President of the Russian Federation for Support of Young Russian Scientists and Leading Scientific Schools, project no. NSh-2288.2003.1.

REFERENCES

1. A. E. H. Love, *A Treatise on the Mathematical Theory of Elasticity*, 4th ed. (Cambridge Univ. Press, Cambridge, 1927; ONTI, Moscow, 1935).
2. B. A. Galanov, Izv. Akad. Nauk SSSR, Mekh. Tverd. Tela, No. 6, 56 (1983).
3. B. A. Galanov, Izv. Akad. Nauk SSSR, Mekh. Tverd. Tela, No. 5, 61 (1981).
4. B. A. Galanov and Yu. M. Krivonos, in *Calculus and Applied Mathematics: Collection of Scientific Works* (Kiev. Gos. Univ., Kiev, 1984), No. 53, pp. 87–94.
5. I. A. Soldatenkov, Izv. Akad. Nauk, Mekh. Tverd. Tela, No. 4, 51 (1994).
6. A. M. Khludnev and V. A. Kovtunenko, *Analysis of Cracks in Solids* (WIT Press, Boston, 2000).
7. M. Ya. Leonov, Prikl. Mat. Mekh. **3** (2), 53 (1939).
8. G. Schubert, Ing. Arch. **13** (3), 132 (1942).
9. I. Ya. Shtaerman, *Contact Problem in the Theory of Elasticity* (Gostekhizdat, Moscow, 1949).
10. H. Hertz, Jahrb. Reine Angew. Math. **92**, 156 (1882).
11. V. I. Mossakovskiĭ, Prikl. Mat. Mekh. **17**, 477 (1953).
12. Yu. V. Kolesnikov and E. M. Morozov, *Mechanics of Contact Fracture* (Nauka, Moscow, 1989).
13. S. A. Zegzhda, *Impact of Elastic Solids* (S.-Peterb. Gos. Univ., St. Petersburg, 1994).
14. I. I. Argatov, in *Collection of Selected Works. Second Polyakhovskiĭ Lectures* (NII Khimii S.-Peterb. Gos. Univ., St. Petersburg, 2000), pp. 237–246.
15. H. Deresiewicz, Acta Mech. **6** (1), 110 (1968).

Translated by R. Tyapaev

Doklady Physics, Vol. 49, No. 4, 2004, pp. 226–230. Translated from Doklady Akademii Nauk, Vol. 395, No. 4, 2004, pp. 474–478.

MECHANICS

Analytical Solution of the Axisymmetric Problem of the Dynamics of a Hemispherical Dome

G. G. Bulychev* and P. F. Sabodash**

Presented by Academician S.S. Grigoryan November 21, 2003

Received November 28, 2003

In this study, an analytical solution of the problem of the dynamics of an axisymmetric body is presented. The dynamics of the body is mathematically described in a spherical coordinate system. The body material is assumed to be homogeneous, isotropic, and linearly elastic. Body forces are absent.

A solution is constructed by the method of expansion in a series in the Legendre functions $P_n^{(0)} \equiv P_n$ and first associated Legendre functions $P_n^{(1)}$ forming an orthogonal basis for the characteristics of the stress–strain state of the body. The basis is natural, because both normal and tangent (to the boundary surfaces of the body) components of stresses and displacements are expanded in different axes of the basis.

The dynamics of the body is mathematically described by the equations

$$(2\mu + \lambda)\nabla(\nabla \cdot \mathbf{u}) - \mu\nabla \times \nabla \times \mathbf{u} = \rho\partial_t^2\mathbf{u},$$
$$\varepsilon_{ij} = 0.5(\nabla_i u_j + \nabla_j u_i), \quad \sigma_{ij} = 2\mu\varepsilon_{ij} + \lambda\delta_{ij}\varepsilon, \quad (1)$$
$$i, j = 1, 2, 3,$$

where μ and λ are the Lamé constants; ∇ is the Hamilton operator; $\mathbf{u}$ is the particle velocity vector; ε_{ij} and σ_{ij} are the strain and stress tensor components, respectively; δ_{ij} is the Kronecker delta; $\varepsilon = \varepsilon_{11} + \varepsilon_{22} + \varepsilon_{33}$, ρ is the density; t is time; $\partial_t^2 = \dfrac{\partial^2}{\partial t^2}$; and the dot and cross between the vectors refer to their scalar and vector products, respectively. We will write Eqs. (1) in a spherical coordinate system $\{R, \theta, \varphi\}$ with allowance for symmetry about φ, i.e., $u_\varphi = \varepsilon_{\alpha\varphi} = \sigma_{\alpha\varphi} = \dfrac{\partial}{\partial\varphi} = 0$, where $\alpha = R$ or θ. The functions entering into Eqs. (1) are assumed to be expandable into a series in the products of the form $f(R, t, \theta) = f_1(R, t) \cdot f_2(\theta)$. This constraint is typical for the method of separation of variables.

We decompose $\mathbf{u}$ into the gradient and curl components:

$$\mathbf{u} = \nabla\Phi + \nabla \times \mathbf{\Psi}, \quad (2)$$

where Φ and $\mathbf{\Psi}$ are the scalar and vector displacement potentials. In our problem, we have $\Phi_R \equiv \Phi$ and $\Psi_\theta \equiv \Psi$. Using Eqs. (1) and (2), we obtain the equations for Φ and Ψ in the form

$$\nabla \cdot \nabla\Phi = \partial_\tau^2\Phi, \quad \nabla \times \nabla \times \mathbf{\Psi} = -\gamma^2\partial_\tau^2\mathbf{\Psi},$$
$$\gamma = \frac{c_\parallel}{c_\perp} \quad (3)$$

or, by virtue of the symmetry of the problem, in the form

$$\Delta\Phi = \partial_\tau^2\Phi, \quad \Delta^*\Psi = \gamma^2\partial_\tau^2\Psi,$$
$$\Delta^* = \Delta - R^{-2}\sin^{-2}\theta, \quad (4)$$

where $c_\parallel = \sqrt{\dfrac{2\mu + \lambda}{\rho}}$, $c_\perp = \sqrt{\dfrac{\mu}{\rho}}$, $\tau = c_\parallel t$, and Δ is the Laplace operator.

The displacements and stresses entering into Eqs. (1) are expressed in terms of the potentials Φ and Ψ by Eq. (2) in the form

$$u_R = \frac{\partial\Phi}{\partial R} + \frac{1}{R\sin\theta}\frac{\partial}{\partial\theta}\sin\theta\Psi, \quad u_\theta = \frac{1}{R}\left[\frac{\partial\Phi}{\partial\theta} - \frac{\partial}{\partial R}R\Psi\right],$$

$$\bar{\sigma}_{RR} = \nu_s\Delta\Phi + \left(\frac{\partial^2\Phi}{\partial R^2} + \frac{1}{\sin\theta}\frac{\partial}{\partial\theta}\sin\theta\frac{\partial}{\partial R}\frac{\Psi}{R}\right),$$

$$\bar{\sigma}_{\theta\theta} = \nu_s\Delta\Phi + \frac{1}{R}\left[\frac{\partial}{\partial\theta}\left(\frac{1}{R}\frac{\partial\Phi}{\partial\theta} - \frac{1}{R}\frac{\partial}{\partial R}R\Psi\right)\right.$$

* *State Institute of Physics and Technology, ul. Prechistenka 13/7, Moscow, 119034 Russia*
e-mail: postmaster@dep11.ifftr.msc.su

** *Moscow State University of Environmental Engineering, ul. Pryanishnikova 19, Moscow, 127550 Russia*

1028-3358/04/4904-0226$26.00

$$+\frac{\partial\Phi}{\partial R}+\frac{1}{R\sin\theta}\frac{\partial}{\partial\theta}\sin\theta\Psi\Big],$$

$$\bar{\sigma}_{\varphi\varphi} = \nu_s\Delta\Phi+\frac{1}{R}\Big[\frac{\partial\Phi}{\partial R}+\frac{1}{R\sin\theta}\frac{\partial}{\partial\theta}\sin\theta\Psi$$

$$+\frac{\cot\theta}{R}\Big(\frac{\partial\Phi}{\partial\theta}-\frac{\partial}{\partial R}R\Psi\Big)\Big], \quad (5)$$

$$\bar{\sigma}_{R\theta} = \frac{\partial}{\partial R}\Big(\frac{1}{R}\frac{\partial\Phi}{\partial\theta}\Big)-\frac{1}{2}\Delta^*\Psi$$

$$+\frac{1}{R^2}\Big(\frac{\partial}{\partial R}R\Psi+\frac{\partial}{\partial\theta}\frac{1}{\sin\theta}\frac{\partial}{\partial\theta}\sin\theta\Psi\Big).$$

Here, $\nu_s = \frac{\nu}{1-2\nu}$, where ν is the Poisson ratio; $\bar{\sigma}_{\alpha\beta} = \frac{\sigma_{\alpha\beta}}{2\mu}$, where α and β may be R and θ; and $\bar{\sigma}_{\varphi\varphi} = \frac{\sigma_{\varphi\varphi}}{2\mu}$. Equations (3)–(5), together with the corresponding boundary conditions, make it possible to reduce the problem to the determination of the potentials Φ and Ψ.

We will present Φ and Ψ as the products $\Phi = \Phi_1(R, \tau)\Phi_2(\theta)$ and $\Psi = \Psi_1(R, \tau)\Psi_2(\theta)$, where $\Phi_2(\theta)$ and $\Psi_2(\theta)$ are the eigenfunctions dependent on the θ parts of the operators Δ and Δ^*, which have no singularities in the interval $0 \le \theta \le \frac{\pi}{2}$. It is known [1] that these functions are the Legendre polynomials P_n and first associated Legendre polynomials $P_n^{(1)}$, while the corresponding eigenvalues are given by the expression $m_n = -n(n+1)$. The potentials Φ and Ψ can be written as the following series in these polynomials ($\Phi_n \equiv \Phi_{1n}$ and $\Psi_n \equiv \Psi_{1n}$):

$$\Phi = \sum_{n=0}^{\infty}\Phi_n(R, \tau)P_n(\theta), \quad \Psi = \sum_{n=0}^{\infty}\Psi_n(R, \tau)P_n^{(1)}(\theta). \quad (6)$$

In this case, $\Phi_n(R, \tau)$ and $\Psi_n(R, \tau)$ satisfy the similar equations

$$\Big[\frac{\partial^2}{\partial R^2}+\frac{m_n}{R^2}\Big]R\Phi_n = \frac{\partial^2}{\partial\tau^2}R\Phi_n,$$
$$\Big[\frac{\partial^2}{\partial R^2}+\frac{m_n}{R^2}\Big]R\Psi_n = \gamma^2\frac{\partial^2}{\partial\tau^2}R\Psi_n. \quad (7)$$

These equations for $R\Phi_0(R, \tau)$ and $R\Psi_0(R, \tau)$ take the form of the well-studied equations for longitudinal and transverse plane waves. The equation for Φ_0 is widely used in spherically symmetric problems.

In order to obtain the solutions of Eqs. (7) for $n \ge 0$, we take their Laplace transforms with respect to τ. Let us establish the correspondence between the original quantities and their transforms:

$$\tau \Leftrightarrow s, \quad \Phi_n(R, \tau) \Leftrightarrow \Phi_n^*(R, s)$$

and

$$\Psi_n(R, \tau) \Leftrightarrow \Psi_n^*(R, s).$$

Under zero initial conditions, the equations for the transforms Φ_n^* and Ψ_n^* take the form

$$\frac{d^2R\Phi_n^*(R, s)}{dR^2}-\frac{n(n+1)\Phi_n^*(R, s)}{R}$$

$$-s^2R\Phi_n^*(R, s) = 0,$$

$$\frac{d^2R\Psi_n^*(R, s)}{dR^2}-\frac{n(n+1)\Psi_n^*(R, s)}{R}$$

$$-\gamma^2s^2R\Psi_n^*(R, s) = 0. \quad (8)$$

The solution of Eqs. (8) has the form [2]

$$\Phi_n^*(R, s) = C_{1n}\hat{L}_ne^{sR}+C_{2n}\hat{L}_ne^{-sR},$$
$$\Psi_n^*(R, s) = C_{3n}\hat{L}_ne^{s\gamma R}+C_{4n}\hat{L}_ne^{-s\gamma R}, \quad (9)$$

where $\hat{L}_n = R^n\Big(R^{-1}\frac{d}{dR}\Big)^{n+1}$ and C_{in}, $i = 1, 2, 3, 4$, are the constants determined from the boundary conditions.

For the further presentation, it is useful to recall some information on the functions $P_n(\cos\theta)$ and $P_n^{(1)}(\cos\theta)$ [1]. These functions are orthogonal polynomials. They are orthogonal with respect to the number n within their families. Moreover, the functions with the same number that belong to different families are also orthogonal to each other. The quantities $g_{0n} = n+\frac{1}{2}$ and $g_{1n} = \frac{g_{0n}}{|m_n|}$. are the normalization constants for P_n and $P_n^{(1)}$, respectively.

Thus, the sets $\{P_n\}$ and $\{P_n^{(1)}\}$ form two independent families and can be used to expand functions that are either continuous or piecewise-continuous and bounded in the interval [–1, 1].

We use the following relations between P_n and $P_n^{(1)}$:

$$P_n(x) = \frac{1}{2^n n!}\frac{d^n}{dx^n}(x^2-1)^n, \quad P_n^{(1)}(x) = -\sin\theta\frac{dP_n}{dx},$$

$$x = \cos\theta,$$

$$g_{0n}\int_{-1}^{1} P_n(x)P_m(x)dx = \delta_{nm},$$

$$g_{1n}\int_{-1}^{1} P_n^{(1)}(x)P_m^{(1)}(x)dx = \delta_{nm}, \qquad (10)$$

$$\int_{-1}^{1} P_n(x)P_m^{(1)}(x)dx = 0,$$

$$\frac{1}{\sin\theta}\frac{d}{d\theta}\sin\theta P_n^{(1)} = -n(n+1)P_n,$$

$$\frac{dP_n}{d\theta} = P_n^{(1)}, \quad \frac{dP_n^{(1)}}{d\theta} = -[n(n+1)P_n + \cot\theta P_n^{(1)}].$$

In view of Eqs. (8) and (10), the transforms of the displacement and stress components given by Eqs. (5) are represented in the form

$$u_R^* = \sum_{n=0}^{\infty}\left[\frac{d\Phi_n^*}{dR} - \frac{n(n+1)\Psi_n^*}{R}\right]P_n,$$

$$u_\theta^* = \frac{1}{R}\sum_{n=1}^{\infty}\left[\Phi_n^* - \frac{d}{dR}R\Psi_n^*\right]P_n^{(1)},$$

$$\bar\sigma_{RR}^* = \sum_{n=0}^{\infty}\left[\frac{\gamma^2 s^2\Phi_n^*}{2} - \frac{2}{R}\frac{d\Phi_n^*}{dR}\right.$$

$$\left. + n(n+1)\left(\frac{\Phi_n^*}{R^2} - \frac{d}{dR}\frac{\Psi_n^*}{R}\right)\right]P_n,$$

$$\bar\sigma_{R\theta}^* = \sum_{n=1}^{\infty}\left[\frac{d}{dR}\frac{\Phi_n^*}{R} - \frac{1}{2}\gamma^2 s^2\Psi_n^*\right.$$

$$\left. + \frac{1}{R^2}\frac{d}{dR}R\Psi_n^* - \frac{n(n+1)\Psi_n^*}{R^2}\right]P_n^{(1)}, \qquad (11)$$

$$\bar\sigma_{\theta\theta}^* = \sum_{n=0}^{\infty}\left[\nu_s s^2\Phi_n^* + \frac{1}{R}\frac{d\Phi_n^*}{dR} - \frac{n(n+1)}{R^2}\right.$$

$$\left.\times\left(\Phi_n^* - \frac{1}{R}\frac{dR^2\Psi_n^*}{dR}\right)\right]P_n - \frac{\cot\theta}{R^2}\sum_{n=1}^{\infty}\left[\Phi_n^* - \frac{d}{dR}R\Psi_n^*\right]P_n^{(1)},$$

$$\bar\sigma_{\varphi\varphi}^* = \sum_{n=0}^{\infty}\left[\nu_s s^2\Phi_n^* + \frac{1}{R}\frac{d\Phi_n^*}{dR} - \frac{n(n+1)\Psi_n^*}{R^2}\right]P_n$$

$$+ \frac{\cot\theta}{R^2}\sum_{n=1}^{\infty}\left[\Phi_n^* - \frac{d}{dR}R\Psi_n^*\right]P_n^{(1)}.$$

These relations contain complete information on the dynamics of the body under consideration in the operator form. Therefore, it is appropriate to consider these relations in more detail.

Relations (11) were obtained with the only additional assumption being that the potentials of the problem can be represented in form (6). The components of the normal and tangent (to the body boundaries) displacements and stresses are expanded in accordance with the potentials. This implies that the normal displacement and stress, as well as the "gradient" potential Φ^*, are expanded in terms of the functions P_n, and the tangent displacement and stress, as well as the "curl" potential Ψ^*, in terms of the functions $P_n^{(1)}$. The other stresses are expanded in both components of the discrete basis $\{P_n, P_n^{(1)}\}$.

The presence of $\cot\theta$ in the formulas for $\bar\sigma_{\theta\theta}$ and $\bar\sigma_{\varphi\varphi}$ does not result in the occurrence of poles at $\theta = 0$, because all $P_n^{(1)}$ polynomials include $\sin\theta$ as a factor [see Eq. (10)].

For $n = 0$, all terms involving the potential Ψ^* vanish, and Eq. (11) describes the centrosymmetric stress–strain state of the body, which depends only on the potential Φ^* and is well known from one-dimensional problems of ball dynamics. For $n > 0$, all the characteristics of the stress–strain state involve both potentials, and the powers of the functions $\sin\theta$ and $\cos\theta$ entering into P_n and $P_n^{(1)}$ increase with the number n. Thus, expansion (11) may be considered as a series of successive deviations of the stress–strain state from the centrosymmetric state.

At the $\theta = 0$ axis for each $n = 1, 2, \ldots$, we have $P_n^{(1)} = 0$ and, hence, $u_\theta^* = \bar\sigma_{R\theta}^* = 0$, in agreement with the symmetry conditions of the problem. The conditions imposed on the boundary $\theta = \frac{\pi}{2}$, $R_0 \le R \le R_1$ must be consistent with those imposed on the surfaces $R = R_i$, $i = 0$ and 1, $0 \le \theta < \frac{\pi}{2}$.

In particular, in order for the equilibrium conditions

$$F_z = 2\pi \int_{R_0}^{R_1} \int_0^{\pi/2} [\sigma_{RR}(\tau, R, \theta)\cos\theta - \sigma_{R\theta}(\tau, R, \theta)\sin\theta]\sin\theta R^2 d\theta dR = 0,$$

$$U_z = 2\pi \int_{R_0}^{R_1} \int_0^{\pi/2} [u_R(\tau, R, \theta)\cos\theta - u_\theta(\tau, R, \theta)\sin\theta]\sin\theta R^2 d\theta dR = 0$$

to be fulfilled, the forces on the surfaces R_i must be chosen so that the numbers n of the functions P_n and $P_n^{(1)}$ entering into its θ expansion be odd and, moreover, $n \geq 3$. In this case, the natural condition $\sigma_{\theta\theta} = 0$ and the condition $u_R = 0$ are fulfilled on the contour $\theta = \frac{\pi}{2}$. If the force is such that the numbers $n \geq 2$ of both functions are even, then the conditions $\sigma_{R\theta} = u_\theta = 0$ are fulfilled at the boundary $\theta = \frac{\pi}{2}$. The functions P_n and $P_n^{(1)}$ entering into Eqs. (11) cannot have opposite parities, because system (11) was constructed from Eq. (5) under condition (6).

Then, analyzing Eqs. (11), we consider the structure of the expressions in the square brackets. These expressions are linear in Φ^* and Ψ^* and do not involve derivatives higher than the first order with respect to R. Moreover, they include only those s-dependent functions that, first, have the form $\exp(-\zeta Rs)$, where $\zeta = \mp 1$, $\mp\gamma$, which enter into Φ^* and Ψ^*; second, have the form s^2, which were obtained by repeated differentiation with respect to time; and, third, enter into C_{jn}, $j = 1, 2, 3, 4$, $n = 0, 1, 2, \ldots$, and are determined after the representation of the conditions on the boundaries R_i, $i = 0, 1$.

In accordance with the Laplace transform formulas [3], for each piecewise-smooth function $F^*(R_i, s) \Leftrightarrow F(R_i, \tau)$ and the operator $\hat{L}_n$ defined in Eq. (9), there is the correspondence

$$F^*(R_i, s)\hat{L}_n e^{-\zeta Rs} \Leftrightarrow \begin{cases} \hat{L}_n F(R_i, \tau - \zeta R) & \text{for } \tau \geq \zeta R \\ 0 & \text{for } \tau < \zeta R. \end{cases} \quad (12)$$

Therefore, the functions Φ^* and Ψ^* and their derivatives with respect to R may be considered as translation (in time) functions differentiated with respect to R (with a weight of R^{-1}), which lead to the formation of a series of waves traveling inward from the boundaries of the body. The amplitude and shape of these waves are determined by the boundary conditions.

Therefore, after the determination of C_{jn}, substitution of them into Φ^* and Ψ^*, and the inverse Laplace transform, Φ^* and Ψ^* must be expanded in series in terms of the transforms and the method of characteristics in the (R, τ) plane must be applied.

Let us determine C_{jn} from the boundary conditions of the problem. According to Eqs. (11), if the radial displacements $u_R(R_i, \tau)f_1(\theta)$, radial stresses $\bar{\sigma}_{RR}(R_i, \tau)f_2(\theta)$, or their combinations are given on the boundaries R_i, then $f_j(\theta)$, $j = 1, 2$, should be expanded in P_n:

$$f_j(\theta) = \sum_{n=0}^{\infty} a_{jn} P_n,$$
$$a_{jn} = g_{0n} \int_{-1}^{1} f_j(\arccos x) P_n(x) dx. \quad (13)$$

If the tangent displacements $u_\theta(R_i, \tau)f_3(\theta)$, tangent stresses $\bar{\sigma}_{R\theta}(R_i, \tau)f_4(\theta)$, or their combinations are specified, then $f_j(\theta)$, $j = 3, 4$, should be expanded in $P_n^{(1)}$:

$$f_j(\theta) = \sum_{n=1}^{\infty} b_{jn} P_n^{(1)},$$
$$b_{jn} = g_{1n} \int_{-1}^{1} f_j(\arccos x) P_n^{(1)}(x) dx. \quad (14)$$

For more complicated boundary conditions involving combinations of functions expanded in the different families of orthogonal Legendre polynomials, the corresponding expansion takes the form

$$f(\theta) = \sum_{n=0}^{\infty} a_n P_n + \sum_{n=1}^{\infty} b_n P_n^{(1)}, \quad (15)$$

where, in view of the orthogonality of P_n and $P_n^{(1)}$, the coefficients a_n and b_n are determined by formulas (13) and (14).

We express Φ_n^* and Ψ_n^* in terms of the functions $\varphi_{1n} = \hat{L}_n \exp(sR)$, $\varphi_{2n} = \hat{L}_n \exp(-sR)$, $\psi_{1n} = \hat{L}_n \exp(\gamma sR)$, and $\psi_{2n} = \hat{L}_n \exp(-\gamma sR)$ and equate the expressions for the normal and tangent displacements and stresses at the boundary points R_i for each number n in Eq. (11) to the corresponding terms of the expansions of their values specified on these boundaries.

For $n = 0$, nonzero radial displacements or stresses can be specified at the boundaries $R = R_i$, $i = 0, 1$. In this case, C_{10} and C_{20} are determined from the equations

$$\begin{aligned} &C_{10}\frac{d\varphi_{10}}{dR} + C_{20}\frac{d\varphi_{20}}{dR} = a_{10}u_R^*(R_i, s), \quad i = 0, 1, \\ &\left[\frac{\gamma^2 s^2}{2} - \frac{2}{R}\frac{d}{dR}\right](C_{10}\varphi_{10} + C_{20}\varphi_{20}) = a_{20}\bar{\sigma}_{RR}^*(R_i, s). \end{aligned} \tag{16}$$

For $n > 0$, the boundary conditions are chosen from the expressions

$$\begin{aligned} &\frac{d}{dR}(C_{1n}\varphi_{1n} + C_{2n}\varphi_{2n}) + n(n+1) \\ &\times\left[\frac{C_{3n}\psi_{1n} + C_{4n}\psi_{2n}}{R}\right] = a_{1n}u_R^*(R_i, s), \\ &\left[\frac{\gamma^2 s^2}{2} - \frac{2}{R}\frac{d}{dR} + \frac{n(n+1)}{R^2}\right](C_{1n}\varphi_{1n} + C_{2n}\varphi_{2n}) \\ &- n(n+1)\frac{d}{dR}\frac{[C_{3n}\psi_{1n} + C_{4n}\psi_{2n}]}{R} = a_{2n}\bar{\sigma}_{RR}^*(R_i, s), \\ &C_{1n}\varphi_{1n} + C_{2n}\varphi_{2n} - \frac{d}{dR}R[C_{3n}\psi_{1n} + C_{4n}\psi_{2n}] \\ &= b_{1n}R_i u_\theta^*(R_i, s), \\ &\frac{d}{dR}\left[\frac{C_{1n}\varphi_{1n} + C_{2n}\varphi_{2n}}{R}\right] \\ &-\left[\frac{\gamma^2 s^2}{2} - \frac{1}{R^2}\frac{d}{dR}R + \frac{n(n+1)}{R^2}\right] \\ &\times(C_{3n}\psi_{1n} + C_{4n}\psi_{2n}) = b_{2n}\bar{\sigma}_{R\theta}^*(R_i, s). \end{aligned} \tag{17}$$

Determining C_{jn} from Eqs. (16) and (17) and substituting them into Eqs. (9) and (6), we obtain the operator form of the potentials Φ and Ψ as series in $P_n(\theta)$ and $P_n^{(1)}(\theta)$. Finally, taking the inverse Laplace transform $\Phi^*(s) \Rightarrow \Phi(\tau)$ and $\Psi^*(s) \Rightarrow \Psi(\tau)$ and using Eq. (5), we obtain all the original parameters of the stress–strain state for the problem.

REFERENCES

1. P. K. Suetin, *Classical Orthogonal Polynomials* (Nauka, Moscow, 1979).
2. E. Kamke, *Gewöhnliche Differentialgleichungen* (Academie, Leipzig, 1959; Nauka, Moscow, 1976).
3. V. A. Ditkin and A. P. Prudnikov, *Handbook of Ordinary Differential Equations* (Vysshaya Shkola, Moscow, 1965).

Translated by M. Lebedev

Doklady Physics, Vol. 49, No. 4, 2004, pp. 231–233. Translated from Doklady Akademii Nauk, Vol. 395, No. 4, 2004, pp. 479–481.

MECHANICS

Universal Precursor of Geomechanical Catastrophes

V. A. Dubrovskiĭ and V. N. Sergeev

Presented by Academician E.I. Shemyakin November 25, 2003

Received November 26, 2003

Here, a catastrophe is treated as an abrupt change in the state of the system under consideration, and a catastrophic event lasting a certain, relatively short, time interval is a process of transition from one state to another. The problem of revealing the signs of the approaching catastrophic stage is the most urgent problem in studying the evolutionary–catastrophic behavior of the system. It is particularly important for forecasting earthquakes, rockbursts, and landslides, as well as for decreasing the damage they cause. A statement about an obligatory precursor of catastrophes is formulated as follows [1, 2].

If a system with a certain set of critical parameters has an unstable equilibrium position separating the parameter regions corresponding to stable and unstable states of the system, then an external action generates waves in the stable domain with frequencies that must vanish when the system approaches the critical unstable equilibrium position for finite sizes of wave perturbations.

According to this principle, any catastrophe must be preceded by slow wave changes in certain parameters characterizing the state of the system. The frequency of these natural wave motions of the instability center tends to zero upon approaching the instability threshold, or catastrophe. Such a behavior is exemplified by (i) current vertical and horizontal motions whose direction reverses prior to orogenesis [2]; (ii) slow motions of the day surface detected by geodesic methods on the Garm test site (Tajikistan) before earthquakes; (iii) failure of slip along a crack [3] simulating earthquakes; (iv) rock impacts and development of fracture of solids that are preceded by waves traveling along a crack (trapped waves [4]); and (v) slow wave motions detected as seiche oscillations in the Black Sea before earthquakes in the Black Sea region (the Caucasus, Turkey, the Balkans) [5].

The specific wave character of signs preceding a catastrophe with a continuous decrease in their frequencies was noted when studying the earthquake preparation process. The observed phenomena of weak seismic splash and its damping immediately before an earthquake can be associated with the above decrease in the frequency of the waves when the geophysical parameters of the future seismic center approach the catastrophic threshold values. Indeed, seismic instruments in this case begin to detect the precursor waves when they fall within the detection band. Then, with the further decrease in frequency upon approaching unstable equilibrium, seismic lull occurs, i.e., wave phenomena leave the detection band. Moreover, calm associated with the presence of dissipation in the system is also possible. In any case, this prognostic sign must always appear, because it is an inseparable element of the evolution of the seismic center towards the instability threshold. Moreover, this wave deformation process preceding an earthquake can initiate other previously noted signs of various physical origins. An increase in the radon content and change in the water level in wells as a result of change in the susceptibility of the crust under its periodic deformation or electric and electromagnetic phenomena in the atmosphere and ionosphere [6], which can be attributed to the electrohydrodynamic and electroelastic mechanisms of the generation of the electric field and, therefore, electromagnetic radiation [7], are among these signs. We note that slow waves preceding earthquakes in Turkey, the Caucasus, and the Balkans are almost directly detected by detecting seiche oscillations in the Black Sea [5]. In this case, seiche oscillations are resonantly excited when slow variable-frequency waves preceding earthquakes fall within the necessary frequency band.

A similar decrease in the frequency of seismoacoustic background is also detected before rockbursts in mines as well as before the destruction of the continuity of a solid when a deep crack is formed and developed.

Since the wave precursor of natural and technogenic catastrophes (first predicted in [8]) seems to be very important both fundamentally and for applications, we discuss its physical meaning with simultaneous mathematical justification of the principle formulated above. Since the wave behavior under consideration is manifested primarily in the linear approximation, we should deal with linearized stability theory. The physics of the process is such that randomly generated small perturbations increase when developing the instability of the

Institute of Geosphere Dynamics,
Russian Academy of Sciences,
Leninskiĭ pr. 38-6, Moscow, 117334 Russia

1028-3358/04/4904-0231$26.00

ground state and thereby drive the system to a new state by transferring energy from the ground state to the new state. In this case, randomly generated perturbation is not necessarily the single driving force of the transformation of states during the entire catastrophic interval. This force can also be a sequence of small perturbations and catastrophic periods alternating each other, as occurs, e.g., when turbulence and vorticity are developed in a continuous medium (ordered chaos) [9].

We have to study the natural wave motions of the system approaching the unstable equilibrium position, i.e., the catastrophe threshold. Therefore, we must first solve the problem of system equilibrium that is specified by certain partial differential equations in the presence of spatially periodic, time-independent perturbation under given boundary conditions. This solution must yield the characteristic equation for the real critical length $\lambda_c = \frac{2\pi}{k_c}$ of the perturbation wave at which the system can be in the unstable equilibrium state:

$$\Delta(k, q) = 0. \quad (1)$$

Here, $k = \frac{2\pi}{\lambda}$ is the wave number and q is one or several dimensionless parameters depending on the elastic density parameters of the system. The unstable equilibrium position means that $\Delta(k, q)$ as a function of k has opposite signs on different sides of the point k_c; i.e., the plot of $\Delta(k, q)$ as a function of k intersects rather than touches the k axis at the point $k = k_c$. At the same time, mathematical analysis of the dynamic (time-dependent) problem for the same system with the same boundary conditions leads to the characteristic equation relating the frequency ω and wave number k of the wave perturbation:

$$f(\omega, k, q) = 0. \quad (2)$$

Dispersion equation (2) arises when the wave solution of the linearized partial differential equations describing the behavior of the system is sought in the form

$$u = u_0 \exp\{i(\omega t - kx)\}.$$

The dynamic description obviously reduces to the static description in the limit of very slow wave processes, when the frequency ω is close to zero. This means that Eq. (2) reduces to Eq. (1) in the static limit; i.e., $f(\omega, k, q) \longrightarrow \Delta(k, q)$ for $\omega \longrightarrow 0$. Since we analyze the behavior of the system near the instability threshold, i.e., for low frequencies, $f(\omega, k, q)$ can be expanded as a function of ω near the point $\omega = 0$:

$$f(\omega, k, q) \approx \Delta(k, q) - ib\omega + \frac{a\omega^2}{2}. \quad (3)$$

Here, the expansion coefficients $b = -\left(\frac{\partial f}{\partial \omega}\right)_{\omega = 0}$ and $a = \left(\frac{\partial^2 f}{\partial \omega^2}\right)_{\omega = 0}$ are assumed to be real; i.e., we assume that the equations do not involve odd derivatives with respect to x_j, and the imaginary unit i appears due to the dependence $u = u_0 \exp\{i(\omega t - kx)\}$ in the presence of dissipative terms in the equations (with odd time derivatives). According to the theory of linear partial differential equations, the last property means that either damping (dissipation) or increase (instability) in the solution with time is possible.

For a conservative (without dissipation) system, the second term on the right-hand side of Eq. (3) vanishes, because characteristic equation (2) in this case involves only frequency squared. Then, from Eqs. (2) and (3), we obtain

$$\omega^2 = -\frac{2\Delta(k, q)}{a}. \quad (4)$$

This equation shows that there is always an imaginary frequency ω responsible for an exponentially increasing solution and an oscillating solution on the first and second sides of the point k_c, respectively, due to the existence of unstable equilibrium. This means that natural oscillations with decreasing frequency must exist in the conservative system evolving towards the instability threshold, and this decrease is proportional to the decrease in the function $\Delta(k, q)$ when k approaches k_c. At the unstable equilibrium point, where $\Delta(k, q) = 0$, the frequency of the natural oscillations vanishes and then becomes imaginary according to the reversal of the sign of $\Delta(k, q)$, which means the exponential increase in small perturbations, i.e., the development of instability.

In the presence of damping in the system, the behavior of the system approaching the instability threshold is quite different. We first give some preliminary remarks. According to Eqs. (2) and (3), we arrive at the square equation for ω in the stable region near the instability threshold. For simplicity, the coefficient a of the term ω^2 can always be taken to be positive. Since damped oscillations must occur in the system in the stable region after an external action, the coefficient b of the term ω must be taken to be positive. Then, the solution of the square equation for ω has the form

$$\omega = \frac{1}{a}\left(ib \pm \sqrt{-b^2 - 2a\Delta}\right). \quad (5)$$

It follows from Eq. (5) that Δ must be negative in the stable region, where damped oscillations exist by definition. In this case, for sufficiently large $|\Delta|$, i.e., far enough from the catastrophic threshold, damped oscillations occur (due to an external action). If $|\Delta|$ decreases with the evolution of the system, the real part of frequency decreases according to Eq. (5), which means

slower oscillations of the system, and the phase velocity $c = \frac{\omega}{k}$ of perturbations tends to zero, because k tends to a finite value $\bar{k}$. When $2|a\Delta| = b^2$, the radicand in Eq. (5) vanishes at $k = \bar{k}$, oscillation frequency vanishes, and any perturbation is continuously damped near $k = \bar{k}$. This exponential continuous damping occurs for $k_c < k < \bar{k}$. In this case, the damping of perturbations slows down when k approaches k_c. When Δ vanishes at $k = k_c$, the instability threshold is reached. After that, perturbations in the system with positive Δ increases exponentially, which corresponds to the ω branch with the negative sign of the root in Eq. (5).

In summary, the system evolving towards a catastrophe behaves as follows. First, natural oscillations are generated in the system by an external action in the stable domain. They are damped in the presence of dissipation. Then, with a decrease in $|\Delta|$ ($\Delta < 0$), any perturbation induced by the external action is damped without the oscillating regime. This means the beginning of the lull stage before the approaching catastrophe. The catastrophe begins and is developed for $k \le k_c$, when Δ becomes positive. At $k = k_c$, the ω branch with a negative imaginary part arises, which gives rise to the continuous exponential increase in perturbation. This is a scenario of the system behavior in the stable region upon approaching the catastrophic threshold.

Therefore, for systems with dissipation, two prognostic stages can be indicated: a decrease in, first, the frequency of observed wave perturbations and, second, the damping decrement of aperiodic perturbations. When dissipation is sufficiently low, the second stage can be short, and the decrease in the frequency of oscillatory perturbations to very low values immediately changes to the development of instability similar to conservative systems without real lull.

The above approach is also applicable to any systems with conservation laws that can be represented by, e.g., partial differential equations (bank systems, economic and social structures, ethnic groups, etc.). The above theory of catastrophe is quite general, and its generality is at the level of conservation laws. The principle formulated above clearly determines change in the governing parameters of a system before the catastrophic stage. It is substantial that only the conditions of unstable equilibrium and the governing parameters of the system are sufficient.

ACKNOWLEDGMENTS

This work was supported by the Russian Foundation for Basic Research, project no. 03-05-64087.

REFERENCES

1. V. A. Dubrovskiĭ and V. N. Sergeev, *Neogene Tectonics: General and Regional Aspects* (GEOS, Moscow, 2001), pp. 222–226.
2. V. A. Dubrovskiĭ, *Lithosphere of Central and Eastern Europe: Geodynamics* (Naukova Dumka, Kiev, 1988), pp. 118–124.
3. V. A. Dubrovskiy and D. Dieterich, EOS Trans. Am. Geophys. Union **71**, 635 (1989).
4. Y.-G. Li, P. C. Leary, K. Aki, and P. E. Malin, Science **249**, 763 (1990).
5. V. V. Nesterov, *Large-Base Laser Interferometers in Geophysical Research* (Tavriya, Simferopol, 1996).
6. *Atmospheric and Ionospheric Electromagnetic Phenomena Associated with Earthquakes*, Ed. by M. Hayakawa (Terra Sci. Publ, Tokyo, 1999).
7. V. A. Dubrovskiĭ and N. N. Rusakov, Dokl. Akad. Nauk SSSR **306**, 64 (1989).
8. V. A. Dubrovskiĭ, Izv. Akad. Nauk SSSR, Fiz. Zemli, No. 1, 29 (1985).
9. V. A. Dubrovskiĭ, Dokl. Akad. Nauk **370**, 754 (2000) [Dokl. Phys. **45**, 52 (2000)].

Translated by R. Tyapaev

Doklady Physics, Vol. 49, No. 4, 2004, pp. 234–236. Translated from Doklady Akademii Nauk, Vol. 395, No. 4, 2004, pp. 482–484.

MECHANICS

Asymptotic Model of Rayleigh Waves in the Far-Field Zone in an Elastic Half-Plane

Yu. D. Kaplunov* and L. Yu. Kossovich**

Presented by Academician I.G. Goryacheva November 11, 2003

Received November 17, 2003

It is common opinion that a Rayleigh wave does not appear explicitly in the conventional formulations of dynamical problems in the theory of elasticity for bodies with a free surface. As a rule, this wave can be revealed only by additional transformations associated with, e.g., the derivation of the corresponding dispersion equation. The lack of the direct mathematical description (in the form of approximate relationships) of Rayleigh waves complicates the analysis of dynamical surface phenomena and leads to some methodical difficulties in the formulation of a general theory of elastic waves.

In this paper, we formulate an asymptotic model of Rayleigh waves in the far-field zone in the case of plane strain. The first step of the model involves the analysis of hyperbolic equation (12) describing the one-dimensional propagation of a Rayleigh wave along the boundary of a half-plane. Then, the wave attenuation into the half-plane will be found by solving two Neumann problems given by Eqs. (13), (14) and by Eqs. (15), (16) for the Lamé potentials. Our consideration is based on general asymptotic principles and employs the symbolic-integration method.

The equations of motion of an elastic half-plane can be presented in the form

$$\frac{\partial^2\varphi}{\partial x^2} + \frac{\partial^2\varphi}{\partial y^2} - c_1^{-2}\frac{\partial^2\varphi}{\partial t^2} = 0,$$
$$\frac{\partial^2\psi}{\partial x^2} + \frac{\partial^2\psi}{\partial y^2} - c_2^{-2}\frac{\partial^2\psi}{\partial t^2} = 0. \quad (1)$$

Here, x and y are the Cartesian coordinates; t is the time; φ and ψ are the so-called Lamé volume and shear potentials, respectively; and c_1 and c_2 are the velocities of dilatational and shear waves, respectively. The displacements v_i and stresses σ_{ij} ($i, j = 1, 2$) are given by the expressions

$$v_1 = \frac{\partial\varphi}{\partial x} + \frac{\partial\psi}{\partial y}, \quad v_2 = \frac{\partial\varphi}{\partial y} - \frac{\partial\psi}{\partial x}; \quad (2)$$

$$\sigma_{11} = \frac{E}{2(1+\nu)\kappa^2}\left(\frac{\partial^2\varphi}{\partial x^2} + (1-2\kappa^2)\frac{\partial^2\varphi}{\partial y^2} + 2\kappa^2\frac{\partial^2\psi}{\partial x\partial y}\right),$$
$$\sigma_{22} = \frac{E}{2(1+\nu)\kappa^2}\left((1-2\kappa^2)\frac{\partial^2\varphi}{\partial x^2} + \frac{\partial^2\varphi}{\partial y^2} - 2\kappa^2\frac{\partial^2\psi}{\partial x\partial y}\right), \quad (3)$$
$$\sigma_{12} = \frac{E}{2(1+\nu)}\left(2\frac{\partial^2\varphi}{\partial x\partial y} - \frac{\partial^2\psi}{\partial x^2} + \frac{\partial^2\psi}{\partial y^2}\right),$$

where E is Young's modulus, ν is Poisson's ratio, and $\kappa^2 = \frac{c_2^2}{c_1^2} = \frac{1-2\nu}{2-2\nu}$.

Below, we consider only the case of an unsteady normal action on the half-plane boundary $y = 0$ under zero initial conditions. Thus,

$$\sigma_{22}(x, 0, t) = -P(x, t), \quad \sigma_{12} = 0, \quad (4)$$

where $P(x, t)$ is a given stress. We now find the front-line asymptotic expression for the Rayleigh wave in the far-field zone. To this end, we introduce the scaled variables [1]

$$\xi = \frac{x - c_R t}{\varepsilon L}, \quad \zeta = \frac{y}{\varepsilon L}, \quad \tau = \frac{t c_R}{L}. \quad (5)$$

Here, $c_R = k_R c_2$ is the velocity of the Rayleigh wave, where k_R is the root of the transcendent equation

$$(2 - k_R^2)^2 - 4\sqrt{1 - k_R^2}\sqrt{1 - \kappa^2 k_R^2} = 0;$$

and L is a characteristic spatial scale. For example, it is half the length of the spread interval of stress in bound-

* *Institute for Problems of Mechanics, Russian Academy of Sciences, pr. Vernadskogo 101, Moscow, 117526 Russia*

** *Saratov State University, ul. Astrakhanskaya 83, Saratov, 410012 Russia*
e-mail: kossovichLU@yandex.ru

1028-3358/04/4904-0234$26.00 © 2004 MAIK "Nauka/Interperiodica"

ary conditions (4) if it is specified in the form

$$P(x, t) = \exp\left(-\frac{x^2}{4L^2}\right)\frac{f(t)}{\sqrt{\pi}L},$$

where $f(t)$ is a given function of time. In the far-field zone, the small parameter ε can be taken as the ratio of the characteristic size L to the path covered by the Rayleigh wave in a sufficiently large time interval T, i.e., $\varepsilon = \frac{L}{c_R T} \ll 1$.

Introducing the operator notation

$$\partial_\xi = \frac{\partial}{\partial\xi}, \quad \partial_\tau = \frac{\partial}{\partial\tau}, \tag{6}$$

we rewrite Eqs. (1)–(3) in terms of variables (5):

$$\frac{d^2\varphi}{d\xi^2} + [(1-\kappa^2 k_R^2)\partial_\xi^2 + \varepsilon\cdot 2\kappa^2 k_R \partial_\xi\partial_\tau - \varepsilon^2\kappa^2\partial_\tau^2]\varphi = 0,$$
$$\frac{d^2\psi}{d\xi^2} + [(1-k_R^2)\partial_\xi^2 + \varepsilon\cdot 2k_R\partial_\xi\partial_\tau - \varepsilon^2\partial_\tau^2]\psi = 0; \tag{7}$$

$$v_1 = \frac{1}{\varepsilon L}\left(\partial_\xi\varphi + \frac{d\psi}{d\xi}\right), \quad v_2 = \frac{1}{\varepsilon L}\left(\frac{d\varphi}{d\xi} - \partial_\xi\psi\right); \tag{8}$$

$$\sigma_{11} = \frac{E}{2(1+\nu)\kappa^2\varepsilon^2 L^2}\left((1-2\kappa^2)\frac{d^2\varphi}{d\xi^2} + \partial_\xi^2\varphi + 2\kappa^2\partial_\xi\frac{d\psi}{d\xi}\right),$$
$$\sigma_{22} = \frac{E}{2(1+\nu)\kappa^2\varepsilon^2 L^2}\left(\frac{d^2\varphi}{d\xi^2} + (1-2\kappa^2)\partial_\xi^2\varphi - 2\kappa^2\partial_\xi\frac{d\psi}{d\xi}\right), \tag{9}$$
$$\sigma_{12} = \frac{E}{2(1+\nu)\varepsilon^2 L^2}\left(2\partial_\xi\frac{d\varphi}{d\xi} + \frac{d^2\psi}{d\xi^2} - \partial_\xi^2\psi\right).$$

Employing the Lur'e symbolic method [2–4], we write the Lamé potentials in the form

$$\varphi = \exp\{-i[(1-\kappa^2 k_R^2)\partial_\xi^2 + \varepsilon\cdot 2\kappa^2 k_R\partial_\xi\partial_\tau - \varepsilon^2\kappa^2\partial_\tau^2]^{1/2}\xi\}\Phi,$$
$$\psi = \exp\{-i[(1-k_R^2)\partial_\xi^2 + \varepsilon\cdot 2k_R\partial_\xi\partial_\tau - \varepsilon^2\partial_\tau^2]\xi\}^{1/2}\Psi, \tag{10}$$

where $\Phi(\xi, \tau)$ and $\Psi(\xi, \tau)$ are the desired functions. The minus sign in the exponents in symbolic formulas (10) determines the attenuation of the solution with the distance from the boundary of the half-plane.

Substituting expressions (10) for φ and ψ into Eqs. (9) and omitting asymptotically negligible terms, we arrive at the following operator equations under boundary conditions (4):

$$i\varepsilon\cdot 2\sqrt{1-k_R^2}\partial_\xi^2\partial_\tau\Psi = -\frac{(1+\nu)\varepsilon^2 L^2}{E}B\partial_\xi P,$$
$$i\sqrt{1-\kappa^2 k_R^2}\partial_\xi\Phi = -\left(1-\frac{k_R^2}{2}\right)\partial_\xi\Psi, \tag{11}$$

where

$$B = 2\left(\frac{k_R}{1-k_R^2} + \frac{\kappa^2 k_R}{1-\kappa^2 k_R^2} - \frac{2k_R}{1-k_R^2/2}\right)^{-1}.$$

The transformation of the first equation to the initial variables yields the boundary hyperbolic equation for $\chi(x, t) = \left.\frac{\partial\psi}{\partial y}\right|_{y=0}$:

$$\frac{\partial^2\chi}{\partial t^2} - c_R^2\frac{\partial^2\chi}{\partial x^2} = -\frac{(1+\nu)c_R^2 B}{Ek_R}\frac{\partial P}{\partial x}. \tag{12}$$

Knowing the normal derivative of the shear potential on the boundary, we can find the principal part of the potential attenuation into the half-plane by solving the elliptic equation [see operator form (7)]

$$\left(1-\frac{c_R^2}{c_2^2}\right)\frac{\partial^2\psi}{\partial x^2} + \frac{\partial^2\psi}{\partial y^2} = 0 \tag{13}$$

under the boundary condition

$$\frac{\partial\psi}{\partial y} = \chi \tag{14}$$

at $y = 0$. The volume potential is then found from the similar Neumann problem

$$\left(1-\frac{c_R^2}{c_1^2}\right)\frac{\partial^2\varphi}{\partial x^2} + \frac{\partial^2\varphi}{\partial y^2} = 0; \tag{15}$$

$$\left.\frac{\partial\varphi}{\partial y}\right|_{y=0} = \left(1-\frac{c_R^2}{2c_2^2}\right)\left.\frac{\partial\psi}{\partial x}\right|_{y=0}. \tag{16}$$

These relations directly follow from operator formulas (10).

The approximate theory presented above corresponds to an intuitive understanding of a Rayleigh surface wave. Indeed, perturbations now propagate along the half-plane boundary with a finite velocity c_R, which enters explicitly into one-dimensional wave operator (12). In this case, the wave attenuation into the half-plane is described by two-dimensional elliptic equations (13) and (15), which formally contain no derivatives with respect to time. As a result, field singularities of the Rayleigh wave do not pass into the internal region.

The asymptotic expressions for stresses in the far-field zone of the Rayleigh wave take the form

$$\sigma_{11} = \frac{E}{1+\nu}\left[\left(1+\frac{c_R^2}{2c_2^2}-\frac{c_R^2}{c_1^2}\right)\frac{\partial^2\varphi}{\partial x^2}+\frac{\partial^2\psi}{\partial x\partial y}\right],$$

$$\sigma_{22} = -\frac{E}{1+\nu}\left[\left(1-\frac{c_R^2}{2c_2^2}\right)\frac{\partial^2\varphi}{\partial x^2}+\frac{\partial^2\psi}{\partial x\partial y}\right], \qquad (17)$$

$$\sigma_{12} = \frac{E}{1+\nu}\left[\frac{\partial^2\varphi}{\partial x\partial y}-\left(1-\frac{c_R^2}{2c_2^2}\right)\frac{\partial^2\psi}{\partial x^2}\right].$$

As an example, we now calculate the Rayleigh wave for the two-dimensional Lamb problem under boundary conditions (4) with $P(x, t) = p\delta(x)\delta(t)$, where δ is the Dirac delta function and p is a given constant. Standard calculations based on the method of integral transformations for Eqs. (12)–(16) yield the following expressions for the displacements (we consider only $x > 0$, $\eta = c_R t - x$):

$$v_1 = \frac{\sqrt{1-\kappa^2 k_R^2}B(1+\nu)c_2 p}{2\pi(1-k_R^2/2)E}$$

$$\times\left[\frac{y}{(1-\kappa^2 k_R^2)y^2+\eta^2}-\frac{1-k_R^2}{1-k_R^2/2}\frac{y}{(1-k_R^2)y^2+\eta^2}\right],$$

$$v_2 = \frac{\sqrt{1-\kappa^2 k_R^2}B(1+\nu)c_2 p}{2\pi(1-k_R^2/2)E} \qquad (18)$$

$$\times\left[-\frac{\eta}{(1-\kappa^2 k_R^2)y^2+\eta^2}+\frac{1}{1-k_R^2/2}\frac{\eta}{(1-k_R^2)y^2+\eta^2}\right].$$

These formulas coincide with the expressions for the displacement field of the surface wave determined by an exact solution of the Lamb problem [5].

The model formulated above makes it possible to study dynamical effects associated with a Rayleigh wave, e.g., the resonance effect of moving load [6–8]. The above method is applicable not only to an isotropic elastic half-plane. In particular, it can easily be extended to bodies with a more complicated shape and physical–mechanical properties as well as to Stoneley interface waves.

REFERENCES

1. J. D. Cole, *Perturbation Methods in Applied Mathematics* (Blaisdell, Waltham, 1968; Nauka, Moscow, 1974).
2. A. I. Lur'e, *Three-Dimensional Problems of the Theory of Elasticity* (Gostekhizdat, Moscow, 1955; Interscience, New York, 1964).
3. U. K. Nigul, Prikl. Mat. Mekh. **27**, 558 (1963).
4. J. D. Kaplunov, L. Yu. Kossovich, and E. V. Nolde, *Dynamics of Thin-Walled Elastic Bodies* (Academic, San-Diego, 1998).
5. G. I. Petrashen', Dokl. Akad. Nauk SSSR **64**, 649 (1949).
6. R. V. Gol'dshtein, Prikl. Mat. Mekh. **29**, 516 (1965).
7. L. B. Freund, Trans. ASME, J. Appl. Mech. **40**, 699 (1973).
8. Yu. D. Kaplunov, Preprint No. 277, IPM AN SSSR (Institute for Problems in Mechanics, Moscow, 1986).

Translated by V. Chechin

Doklady Physics, Vol. 49, No. 4, 2004, pp. 237–238. Translated from Doklady Akademii Nauk, Vol. 395, No. 4, 2004, pp. 485–486.

MECHANICS

Example of a Flow of a Viscous Incompressible Fluid around a Sphere at an Arbitrary Reynolds Number

A. V. Shcheprov

Presented by Academician A.A. Petrov October 27, 2003

Received October 27, 2003

In [1–3], the Navier–Stokes equations describing axisymmetric flows of an incompressible viscous fluid in cylindrical coordinates with the axial x and radial r components were reduced to the form

$$L\varphi = \sigma, \tag{1}$$

$$\frac{1}{R}L\sigma = \frac{1}{r}\left(\frac{\partial\varphi}{\partial r}\frac{\partial\sigma}{\partial x} - \frac{\partial\varphi}{\partial x}\frac{\partial\sigma}{\partial r}\right) + \frac{2\sigma}{r^2}\frac{\partial\varphi}{\partial x}. \tag{2}$$

Here, $\varphi(x, r)$ is the stream function defined by the formula

$$d\varphi = rv_x dr - rv_r dx,$$

where v_x and v_r are the axial and radial velocity components, respectively; R is the Reynolds number;

$$L = \frac{\partial^2}{\partial x^2} + \frac{\partial^2}{\partial r^2} - \frac{1}{r}\frac{\partial}{\partial r},$$

and $\sigma(x, r)$ is an auxiliary function.

It was found in [1–3] that both sides of Eq. (2) vanish after the substitution of the function

$$\sigma = cr^2, \tag{3}$$

where c is an arbitrary constant; i.e., this function is a particular solution of this equation.

In this study, we consider the stream function given by

$$\varphi = c\left[\frac{a^5r^2}{15(x^2 + r^2)^{3/2}} - \frac{a^2r^2}{6} + \frac{x^2r^2}{10} + \frac{r^4}{10}\right], \tag{4}$$

where a is an arbitrary positive constant and the constant c is from Eq. (3). It is easy to verify that this function is a solution of Eq. (1) with right-hand side (3). In this case,

$$\varphi(x, 0) = \frac{\partial\varphi}{\partial r}(x, 0) \equiv 0$$

on the symmetry axis $r = 0$ for $|x| \geq a$ and

$$\varphi(x, \sqrt{a^2 - x^2}) = \frac{\partial\varphi}{\partial n}(x, \sqrt{a^2 - x^2}) \equiv 0 \tag{5}$$

on the circle $x^2 + r^2 = a^2$, where $\frac{\partial}{\partial n}$ is the normal derivative. Thus, functions (3) and (4) describe an axisymmetric flow of a viscous incompressible fluid around a sphere with radius a, and equalities (5) are the no-slip conditions on the surface of the sphere. Since both sides of Eq. (2) vanish after the substitution of function (3), the resulting flow is independent of the Reynolds number.

For the first time, a flow around a sphere was investigated in the 1850s by Stokes, who solved the equation for a viscous fluid in the absence of convection [4, 5] (see also [6, p. 504]). In 1911, Hadamard [7, p. 1311] solved the problem of the fall of a spherical liquid drop in a different viscous fluid in the absence of mixing. As in the studies by Stokes, the convective (nonlinear) terms in the equations for the viscous fluid were disregarded. The continuity of the tangential stress was one of the conditions imposed on the surface. It is worth noting that an internal flow was described in [7] by function (3), while the function φ coincides with the stream function of Hill's spherical vortex [8], which satisfies both the Euler and Navier–Stokes equations. Since convective terms are absent in the original equations, the solutions obtained in the aforementioned studies are formally valid only for low Reynolds numbers. This study shows that functions (3) and (4), which represent a particular solution of the Navier–Stokes equations given by Eqs. (1) and (2), describe a continuous flow of a viscous fluid around a sphere for

Dorodnicyn Computing Center,
Russian Academy of Sciences,
ul. Vavilova 40, Moscow, 119991 Russia
e-mail: yds@ccas.ru

1028-3358/04/4904-0237$26.00

an arbitrary Reynolds number under one of the possible boundary conditions at infinity.

ACKNOWLEDGMENTS

I am grateful to Yu.D. Shmyglevskiĭ for stimulating discussions and assistance in the preparation of the manuscript for publication.

REFERENCES

1. U. Crudeli, Atti Accad. Naz. Lincei, Cl. Sci. Fis., Mat. Nat., Rend. **5**, 500 (1927).
2. U. Crudeli, Atti Accad. Naz. Lincei, Cl. Sci. Fis., Mat. Nat., Rend. **5**, 783 (1927).
3. U. Crudeli, Atti Accad. Naz. Lincei, Cl. Sci. Fis., Mat. Nat., Rend. **6**, 397 (1927).
4. G. G. Stokes, Philos. Mag. **1**, 337 (1851).
5. G. G. Stokes, Trans. Cambridge Philos. Soc. **9**, 8 (1856).
6. N. E. Kochin, I. A. Kibel', and N. V. Roze, *Theoretical Hydromechanics* (Fizmatgiz, Moscow, 1963), Part 2.
7. *Oeuvres de Jacques Hadamard* (CNRS, Paris, 1968), Vol. 3.
8. M. J. M. Hill, Br. Assoc. Adv. Sci., Rep. 696 (1893).

Translated by T. Syromyatnikova

Doklady Physics, Vol. 49, No. 4, 2004, pp. 239–245. Translated from Doklady Akademii Nauk, Vol. 395, No. 5, 2004, pp. 614–620.

MECHANICS

Destabilization Paradox

O. N. Kirillov

Presented by Academician V.F. Zhuravlev December 4, 2003

Received December 10, 2003

In 1952, analyzing the stability of a two-link pendulum loaded by a follower force, H. Ziegler [1] surprisingly concluded that the critical force at which a nonconservative system with negligibly low dissipation lost stability was much weaker than that in a system where dissipation was absent from the very beginning. This phenomenon, called the destabilization paradox, was later found in many mechanical and physical systems [2–4]. Despite numerous works, problems generated by the destabilization paradox have not yet been generally solved, although they are of the most theoretical interest according to Bolotin [2]. In this work, a theory is developed to both qualitatively and quantitatively explain the paradoxical behavior of general nonconservative systems under the action of weak dissipative and gyroscopic forces. The problem of the stability of the Reut–Sugiyama pendulum is analyzed as an example.

1. Let us consider a linear autonomous nonconservative mechanical system described by the equation

$$\mathbf{M}\ddot{\mathbf{y}} + \mathbf{D}(\mathbf{k})\dot{\mathbf{y}} + \mathbf{A}(q)\mathbf{y} = 0, \qquad (1)$$

where $\mathbf{M}$, $\mathbf{D}$, and $\mathbf{A}$ are the real $m \times m$ matrices specifying the inertial, dissipative along with gyroscopic, and nonconservative position forces, respectively; $\mathbf{y}$ is the generalized coordinate vector; and the dots stand for differentiation with respect to time t. The matrix $\mathbf{D}$ is a smooth function of the parameter vector $\mathbf{k} = (k_1, k_2, \ldots, k_{n-1})$, $\mathbf{D}(0) = 0$, the matrix $\mathbf{A}$ is a smooth function of the scalar load parameter $q \geq 0$, and the matrix $\mathbf{M}$ is parametrically independent.

Seeking a solution of Eq. (1) in the form $\mathbf{y} = \mathbf{u}\exp(\lambda t)$, we arrive at the generalized eigenvalue problem

$$(\lambda^2\mathbf{M} + \lambda\mathbf{D}(\mathbf{k}) + \mathbf{A}(q))\mathbf{u} = 0, \qquad (2)$$

where $\mathbf{u}$ is the eigenvector and λ is the eigenvalue. A nonconservative system without gyroscopic and dissipative forces ($\mathbf{k} = 0$), which is described by the equation

$$\mathbf{M}\ddot{\mathbf{y}} + \mathbf{A}(q)\mathbf{y} = 0 \qquad (3)$$

is called the circulatory system [1–4]. The spectrum of the circulatory system is mirror symmetric; i.e., if λ is an eigenvalue of the linear operator $\lambda^2\mathbf{M} + \mathbf{A}(q)$, then $-\lambda$, $\bar{\lambda}$, and $-\bar{\lambda}$, where the bar stands for complex conjugation, are also eigenvalues. Therefore, the circulatory system is stable in the Lyapunov sense if all its eigenvalues λ are imaginary and semisimple [5].

Let the circulatory system be stable for $q = 0$. When the load parameter increases and reaches a certain critical value $q = q_0$, two simple imaginary eigenvalues can merge into a double eigenvalue $i\omega_0$ with the Jordan chain of a length of 2. With further increase in the load, the double eigenvalue generally splits into a pair of complex eigenvalues; one of them has a positive real part, which means vibration instability (flutter, Fig. 1a). Thus, the range $0 \leq q < q_0$ belongs to the stability region of the unperturbed system described by Eq. (3) [5].

Perturbation of the circulatory system by weak dissipative and gyroscopic forces ($\mathbf{k} \neq 0$) breaks the coupling between the eigenvalues and, when the load parameter reaches a certain critical value $q = q_{\mathrm{cr}}(k_1, k_2, \ldots, k_{n-1})$, leads to the displacement of one of the eigenvalues to the right-hand side of the complex plane without the formation and further bifurcation of the double eigenvalue (Fig. 1a). Moreover, if $\mathbf{k} = \varepsilon\tilde{\mathbf{k}}$, where $\tilde{\mathbf{k}}$ is the fixed vector and $\varepsilon \longrightarrow 0$,

$$\tilde{q}_{\mathrm{cr}} \equiv \lim_{\varepsilon \to 0} q_{\mathrm{cr}}(\varepsilon\tilde{\mathbf{k}}) \leq q_0. \qquad (4)$$

This inequality expresses the destabilization paradox first pointed out in [1]: the critical load can abruptly decrease when infinitely weak gyroscopic and dissipative forces are taken into account. More recently, for various mechanical systems, it was shown that the limiting critical load $\tilde{q}_{\mathrm{cr}}$ depends on the choice of the vector $\tilde{\mathbf{k}}$ [2–4]. In particular, changing the relation between the parameters $k_1, k_2, \ldots, k_{n-1}$, one can avoid a decrease in the critical load and thereby destabilization (Bolotin effect [2]). For the two-dimensional Ziegler pendulum with two dissipation parameters, Seyranian [7] found a region on the parameter plane where a nonconservative system perturbed by weak dissipative forces was asymptotically stable and $q_{\mathrm{cr}}(\mathbf{k}) > q_0$.

Institute of Mechanics, Moscow State University, Michurinskiĭ pr. 1, Moscow, 119192 Russia

1028-3358/04/4904-0239$26.00

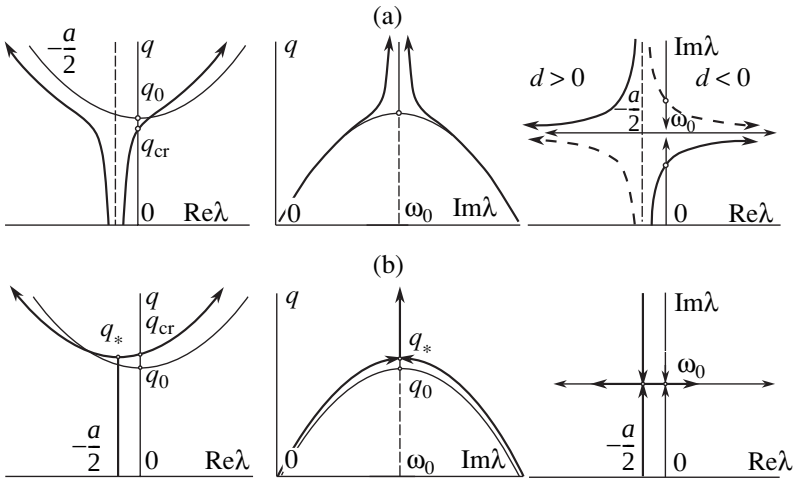

Fig. 1. Trajectories of the eigenvalues of the (thin lines) unperturbed circulatory system and (thick lines) system with weak velocity-dependent forces for (a) $d \neq 0$ and (b) $d = 0$.

In this work, for the general linear nonconservative system described by Eq. (1), an explicit approximation is found for the function $q_{cr}(\mathbf{k})$, which makes it possible to determine both the jump of the critical load and the asymptotic-stability region. In addition, explicit asymptotic expressions are obtained for the description of the trajectories of eigenvalues and their decomposition into independent curves under perturbations of the circulatory system by weak dissipative and gyroscopic forces.

2. Let us consider the point $\mathbf{p}_0 = (0, \ldots, 0, q_0)$ in the n-dimensional space of the parameters $k_1, k_2, \ldots, k_{n-1}$, and q of the system described by Eq. (1). It is assumed that $\pm i\omega_0$, where $\omega_0 > 0$, are the double eigenvalues of the operator $\mathbf{A}(q_0) + \lambda^2\mathbf{M}$ with the Jordan chain of a length of 2 and the remaining eigenvalues $\pm i\omega_{0,s}$, where $\omega_{0,s} > 0$ and $s = 1, 2, \ldots, m-2$, are imaginary and simple. The nonconservative system corresponding to $\mathbf{k} = 0$ and $q = q_0$ is a circulatory system, and the point $\mathbf{p}_0$ belongs to the boundary of the stability region.

Eigenvectors $\mathbf{u}_0$ and $\mathbf{v}_0$, as well as associated vectors $\mathbf{u}_1$ and $\mathbf{v}_1$, corresponding to the double eigenvalue $i\omega_0$ satisfy the equations

$$\begin{aligned}(\mathbf{A}(q_0) - \omega_0^2\mathbf{M})\mathbf{u}_0 &= 0,\\ (\mathbf{A}(q_0) - \omega_0^2\mathbf{M})\mathbf{u}_1 &= -2i\omega_0\mathbf{M}\mathbf{u}_0,\end{aligned} \tag{5}$$

$$\begin{aligned}\mathbf{v}_0^{\mathrm{T}}(\mathbf{A}(q_0) - \omega_0^2\mathbf{M}) &= 0,\\ \mathbf{v}_1^{\mathrm{T}}(\mathbf{A}(q_0) - \omega_0^2\mathbf{M}) &= -2i\omega_0\mathbf{v}_0^{\mathrm{T}}\mathbf{M}.\end{aligned} \tag{6}$$

The vectors $\mathbf{u}_0$, $\mathbf{v}_0$ and $\mathbf{u}_1$, $\mathbf{v}_1$ are taken to be real and imaginary, respectively, so that

$$\begin{aligned}2i\omega_0\mathbf{v}_0^{\mathrm{T}}\mathbf{M}\mathbf{u}_1 &= 1,\\ 2i\omega_0\mathbf{v}_1^{\mathrm{T}}\mathbf{M}\mathbf{u}_1 + \mathbf{v}_1^{\mathrm{T}}\mathbf{M}\mathbf{u}_0 + \mathbf{v}_0^{\mathrm{T}}\mathbf{M}\mathbf{u}_1 &= 0.\end{aligned} \tag{7}$$

Let us analyze the stability of system (1) under the linear perturbation of the parameter vector $\mathbf{p} = (\mathbf{k}, q)$:

$$\mathbf{p}(\varepsilon) = *_0 + \varepsilon\mathbf{p}', \quad \varepsilon \geq 0, \tag{8}$$

where prime means the derivative with respect to ε at $\varepsilon = 0$. The perturbed double eigenvalue is generally expanded into the Newton–Puiseux series

$$\lambda = i\omega_0 + \varepsilon^{1/2}\lambda_1 + \varepsilon\lambda_2 + \ldots, \tag{9}$$

where the coefficients λ_1 and λ_2 are determined from the equations [8]

$$\begin{aligned}\lambda_1^2 &= -i\omega_0\langle\mathbf{f}, \mathbf{k}'\rangle - \tilde{f}q',\\ 2\lambda_2 &= -\langle\mathbf{f} - \omega_0\mathbf{h}, \mathbf{k}'\rangle - i\tilde{h}q'.\end{aligned} \tag{10}$$

Here, angular brackets mean the scalar product of the vector $\mathbf{k}' = (k_1', k_2', \ldots, k_{n-1}')$ and real vectors $\mathbf{f}$ and $\mathbf{h}$ with the components

$$\begin{aligned}f_r &= \mathbf{v}_0^{\mathrm{T}}\frac{\partial\mathbf{D}}{\partial k_r}\mathbf{u}_0, \quad ih_r = \mathbf{v}_1^{\mathrm{T}}\frac{\partial\mathbf{D}}{\partial k_r}\mathbf{u}_0 + \mathbf{v}_0^{\mathrm{T}}\frac{\partial\mathbf{D}}{\partial k_r}\mathbf{u}_1,\\ r &= 1, 2, \ldots, n-1,\end{aligned} \tag{11}$$

and the real values $\tilde{f}$ and $\tilde{h}$ are given by the expressions

$$\tilde{f} = \mathbf{v}_0^{\mathrm{T}}\frac{\partial\mathbf{A}}{\partial q}\mathbf{u}_0, \quad i\tilde{h} = \mathbf{v}_1^{\mathrm{T}}\frac{\partial\mathbf{A}}{\partial q}\mathbf{u}_0 + \mathbf{v}_0^{\mathrm{T}}\frac{\partial\mathbf{A}}{\partial q}\mathbf{u}_1. \tag{12}$$

Thus, from Eqs. (8)–(10), we obtain [8]

$$\begin{aligned}\lambda &= i\omega_0 \pm \sqrt{-i\omega_0\langle\mathbf{f}, \mathbf{k}\rangle - \tilde{f}(q - q_0)}\\ &\quad -\frac{1}{2}(\langle\mathbf{f} - \omega_0\mathbf{h}, \mathbf{k}\rangle + i\tilde{h}(q - q_0)) + \ldots.\end{aligned} \tag{13}$$

If the radicand is nonzero, this equation describes the splitting of the double eigenvalue $i\omega_0$ when varying

the parameters **k** and q. In this case, $i\omega_0$ splits generally into two simple eigenvalues, one of which has a positive real part (instability). If $\langle \mathbf{f}, \mathbf{k}\rangle = 0$, the square root in Eq. (13) is imaginary for $\tilde{f}(q - q_0) > 0$, and the condition $\langle \mathbf{h}, \mathbf{k}\rangle < 0$ is necessary for asymptotic stability. In this case, under sufficiently small perturbations (8), the eigenvalue $i\omega_0$ (and $-i\omega_0$) splits into two simple eigenvalues with negative real parts.

In addition, the stability of system (1) is determined by the behavior of $2m - 4$ simple eigenvalues $\pm i\omega_{0,s}$. Let us take the real right $\mathbf{u}_{0,s}$ and left $\mathbf{v}_{0,s}$ eigenvectors that correspond to the eigenvalues $i\omega_{0,s}$ and satisfy the normalization conditions

$$2\omega_{0,s}\mathbf{v}_{0,s}^{\mathrm{T}}\mathbf{M}\mathbf{u}_{0,s} = 1. \tag{14}$$

The increment of the eigenvalues $\pm i\omega_{0,s}$ under perturbations (8) has the form

$$\lambda = \pm i\omega_{0,s} \mp i\tilde{g}_s(q - q_0) - \omega_{0,s}\langle \mathbf{g}_s, \mathbf{k}\rangle + \ldots, \quad s = 1, 2, \ldots, m-2, \tag{15}$$

where $\tilde{g}_s$ and the components of the real vector $\mathbf{g}_s$ are given by the expressions

$$\tilde{g}_s = \mathbf{v}_{0,s}^{\mathrm{T}}\frac{\partial \mathbf{A}}{\partial q}\mathbf{u}_{0,s}, \quad g_{s,r} = \mathbf{v}_{0,s}^{\mathrm{T}}\frac{\partial \mathbf{D}}{\partial k_r}\mathbf{u}_{0,s}, \quad r = 1, 2, \ldots, n-1. \tag{16}$$

If $\langle \mathbf{g}_s, \mathbf{k}\rangle > 0$, then $\mathrm{Re}\lambda < 0$. Thus, under the conditions

$$\langle \mathbf{f}, \mathbf{k}\rangle = 0, \quad \langle \mathbf{h}, \mathbf{k}\rangle < 0, \quad \tilde{f}(q - q_0) > 0, \quad \langle \mathbf{g}_s, \mathbf{k}\rangle > 0, \quad s = 1, 2, \ldots, m-2, \tag{17}$$

system (1) is asymptotically stable for sufficiently small linear variations of the parameters **k** and q.

3. According to relations (17), the set of directions from the point $\mathbf{p}_0 = (0, q_0)$ to the asymptotic-stability region has the dimension $n - 1$ in the n-dimensional parameter space. It is known that the dimension of the asymptotic-stability region coincides with the dimension of the parameter space [9]. This means that the asymptotic-stability region can be reached only along the curve touching the plane $\langle \mathbf{f}, \mathbf{k}\rangle = 0$ at the point $\mathbf{p}_0$. To gain more precise information about the shape of the asymptotic-stability region near the point $\mathbf{p}_0$, let us consider smooth variation of the parameter vector

$$\mathbf{p}(\varepsilon) = \begin{bmatrix} 0 \\ q_0 \end{bmatrix} + \varepsilon\begin{bmatrix} \mathbf{k}' \\ 0 \end{bmatrix} + \frac{\varepsilon^2}{2}\begin{bmatrix} \mathbf{k}'' \\ q'' \end{bmatrix} + o(\varepsilon^2) \tag{18}$$

under the assumption that

$$\langle \mathbf{f}, \mathbf{k}'\rangle = 0. \tag{19}$$

The curve specified by Eqs. (18) and (19) is orthogonal to the q axis in the parameter space, because $q' \equiv 0$.

The coefficient λ_1 of expansion (9) that is determined by the first of Eqs. (10) vanishes along the curve specified by Eqs. (18) and (19). Therefore, the double eigenvalue splits linearly with respect to ε:

$$\lambda = i\omega_0 + \lambda_2\varepsilon + \ldots, \tag{20}$$

where the coefficient λ_2 is the root of the quadratic equation [8]

$$2\lambda_2^2 - 2\lambda_2\omega_0\langle \mathbf{h}, \mathbf{k}'\rangle + (\tilde{f}q'' + 2\omega_0^2\langle \mathbf{G}\mathbf{k}', \mathbf{k}'\rangle) + i\omega_0(\langle \mathbf{f}, \mathbf{k}''\rangle + 2\langle \mathbf{H}\mathbf{k}', \mathbf{k}'\rangle) = 0. \tag{21}$$

Here, the vectors **f**, **h** and quantities $\tilde{f}$, $\tilde{h}$ are determined by Eqs. (11) and (12), respectively; the real matrix **H** has the components

$$H_{rs} = \frac{1}{2}\mathbf{v}_0^{\mathrm{T}}\frac{\partial^2 \mathbf{D}}{\partial k_r \partial k_s}\mathbf{u}_0, \quad r, s = 1, 2, \ldots, n-1, \tag{22}$$

and the real matrix **G** is determined by the expression

$$\langle \mathbf{G}\mathbf{k}', \mathbf{k}'\rangle = \sum_{r=1}^{n-1} k_r'\mathbf{v}_0^{\mathrm{T}}\frac{\partial \mathbf{D}}{\partial k_r}\mathbf{S}_0\left(\sum_{s=1}^{n-1} k_s'\frac{\partial \mathbf{D}}{\partial k_s}\mathbf{u}_0\right), \tag{23}$$

where $\mathbf{S}_0$ is the operator inverse to the operator $\mathbf{A}(q_0) - \omega_0^2\mathbf{M}$.

In view of Eqs. (18) and (19), which explicitly specify the curve $\mathbf{p}(\varepsilon)$, and expansion (20), Eq. (21) is represented in the form

$$\Delta\lambda^2 - \Delta\lambda\omega_0\langle \mathbf{h}, \mathbf{k}\rangle + \tilde{f}(q - q_0) + \omega_0^2\langle \mathbf{G}\mathbf{k}, \mathbf{k}\rangle + i\omega_0(\langle \mathbf{f}, \mathbf{k}\rangle + \langle \mathbf{H}\mathbf{k}, \mathbf{k}\rangle) = 0, \tag{24}$$

where $\Delta\lambda = \lambda - i\omega_0$. According to the Bilharz criterion [10], all roots of polynomial (24) with complex coefficients have negative real parts iff

$$\tilde{f}(q - q_0) > \frac{(\langle \mathbf{f}, \mathbf{k}\rangle + \langle \mathbf{H}\mathbf{k}, \mathbf{k}\rangle)^2}{\langle \mathbf{h}, \mathbf{k}\rangle^2} - \omega_0^2\langle \mathbf{G}\mathbf{k}, \mathbf{k}\rangle, \tag{25}$$

$$\langle \mathbf{h}, \mathbf{k}\rangle < 0. \tag{26}$$

Without loss of generality, we take $\tilde{f} < 0$. Then, the critical parameter q above which instability (flutter) occurs is given by the expression

$$q_{\mathrm{cr}}(\mathbf{k}) = q_0 + \frac{(\langle \mathbf{f}, \mathbf{k}\rangle + \langle \mathbf{H}\mathbf{k}, \mathbf{k}\rangle)^2}{\tilde{f}\langle \mathbf{h}, \mathbf{k}\rangle^2} - \frac{\omega_0^2}{\tilde{f}}\langle \mathbf{G}\mathbf{k}, \mathbf{k}\rangle. \tag{27}$$

Considering the case where

$$\{\mathbf{k}: q < q_{cr}(\mathbf{k})\} \subset \{\mathbf{k}: \langle \mathbf{h}, \mathbf{k}\rangle < 0, \langle \mathbf{g}_s, \mathbf{k}\rangle > 0, \quad s = 1, 2, \ldots, m-2\}, \tag{28}$$

i.e., all simple eigenvalues $\pm i\omega_{0,s}$ are displaced to the left-hand side of the complex plane, we conclude that the surface $q_{cr}(\mathbf{k})$ approximated by Eq. (27) is the boundary of the asymptotic-stability region. According to Eq. (27), it is easy to see that the limit of q_{cr} as a function of $k_1, k_2, \ldots, k_{n-1}$ does not exist at the point $\mathbf{k} = 0$ due to singularity. This conclusion was first drawn in [6, 7], where the stability of a gyroscope in a gimbal and Ziegler pendulum was analyzed.

Setting $\mathbf{k} = \varepsilon\tilde{\mathbf{k}}$ in Eq. (27), we find the jump of the critical load as a function of $\tilde{\mathbf{k}}$:

$$\Delta q \equiv q_0 - \lim_{\varepsilon \to 0} q_{cr}(\varepsilon\tilde{\mathbf{k}}) = -\frac{1}{\tilde{f}}\frac{\langle \mathbf{f}, \tilde{\mathbf{k}}\rangle^2}{\langle \mathbf{f}, \tilde{\mathbf{k}}\rangle^2}* \tag{29}$$

The limit of q_{cr} along the $\tilde{\mathbf{k}}$ direction exists if $\langle \mathbf{h}, \tilde{\mathbf{k}}\rangle \neq 0$, because the numerator and denominator in Eq. (29) are homogeneous. When $\langle \mathbf{f}, \tilde{\mathbf{k}}\rangle = 0$, the jump of the critical load vanishes. This condition provides the ratio $\frac{k_i}{k_j} = -\frac{f_j}{f_i}$, where $i, j = 1$ and 2, of the components k_1 and k_2 of the two-dimensional vector $\mathbf{k} = (k_1, k_2)$ for which the circulatory system is not destabilized by weak dissipative and gyroscopic forces. The dependence of the critical load on the ratio of the dissipation parameters was first found by Bolotin [2, 3]. For two-dimensional system (1) with the matrix $\mathbf{D}(\mathbf{k}) = k\tilde{\mathbf{D}}$, where $\tilde{\mathbf{D}}$ is a fixed matrix, expression (29) describing the jump of the critical load takes the form

$$\Delta q = \frac{-2(\mathrm{tr}\mathbf{A}_0)^2}{2\mathrm{tr}\mathbf{A}_0\mathbf{A}_1 - \mathrm{tr}\mathbf{A}_0\mathrm{tr}\mathbf{A}_1}\left(\frac{2\mathrm{tr}\mathbf{A}_0\tilde{\mathbf{D}} - \mathrm{tr}\mathbf{A}_0\mathrm{tr}\tilde{\mathbf{D}}}{2\mathrm{tr}\mathbf{A}_0\tilde{\mathbf{D}} - 3\mathrm{tr}\mathbf{A}_0\mathrm{tr}\tilde{\mathbf{D}}}\right)^2,$$

where $\mathbf{A}_0 = \mathbf{A}(q_0)$, $\mathbf{A}_1 = \frac{d\mathbf{A}}{dq}$, and the derivative is taken at $q = q_0$.

The isolines of function (27) are the boundaries of the asymptotic-stability region in the space of the parameters $\mathbf{k} = (k_1, k_2, \ldots, k_{n-1})$. The isolines $q_{cr} = q_0$, where q_0 is the critical parameter q for the unperturbed circulatory system, are given by the expression

$$\langle \mathbf{f}, \mathbf{k}\rangle = \pm\omega_0\langle \mathbf{h}, \mathbf{k}\rangle\sqrt{\langle \mathbf{Gk}, \mathbf{k}\rangle} - \langle \mathbf{Hk}, \mathbf{k}\rangle. \tag{30}$$

For the two-dimensional parameter vector $\mathbf{k} = (k_1, k_2)$, Eq. (27) describes a surface known as the Whitney umbrella [9]. Expressing the parameter k_1 in terms of k_2 from Eq. (30) and vice versa, we obtain an approximation of the boundary of the asymptotic-stability region on the (k_1, k_2) plane for $q_{cr} = q_0$ in the form

$$k_i = -\frac{f_j}{f_i}k_j - \frac{\mathbf{f}^T\mathbf{H}^*\mathbf{f} \pm \omega_0(h_i f_j - h_j f_i)\sqrt{\mathbf{f}^T\mathbf{G}^*\mathbf{f}}}{f_i^3}k_j^2 + o(k_j^2), \quad i, j = 1, 2, \tag{31}$$

$$\mathbf{H}^* = \begin{bmatrix} H_{22} & -H_{12} \\ -H_{21} & H_{11} \end{bmatrix}, \quad \mathbf{G}^* = \begin{bmatrix} G_{22} & -G_{12} \\ -G_{21} & G_{11} \end{bmatrix},$$

where the matrices $\mathbf{H}$ and $\mathbf{G}$ with the respective components H_{rs} and G_{rs}, where $r, s = 1$ and 2, are given by expressions (22) and (23), respectively. It follows from Eq. (31) that the asymptotic-stability region has a singularity—turning point—at the origin. The asymptotic expression for the stabilization-region boundary in form (31) was first found in [7] for the Ziegler pendulum with two independent dissipation parameters.

Substituting $\Delta\lambda = \mathrm{Re}\lambda + i(\mathrm{Im}\lambda - \omega_0)$ into Eq. (24) and separating the real and imaginary parts, we arrive at the following equations describing the displacement of the eigenvalues λ on the complex plane under small variations of the parameters q and $\mathbf{k}$:

$$\left(\mathrm{Im}\lambda - \omega_0 - \mathrm{Re}\lambda - \frac{a}{2}\right)^2 - \left(\mathrm{Im}\lambda - \omega_0 + \mathrm{Re}\lambda + \frac{a}{2}\right)^2 = 2d, \tag{32}$$

$$\left(\mathrm{Re}\lambda + \frac{a}{2}\right)^4 + \left(c - \frac{a^2}{4}\right)\left(\mathrm{Re}\lambda + \frac{a}{2}\right)^2 = \frac{d^2}{4}, \tag{33}$$

$$(\mathrm{Im}\lambda - \omega_0)^4 - \left(c - \frac{a^2}{4}\right)(\mathrm{Im}\lambda - \omega_0)^2 = \frac{d^2}{4}, \tag{34}$$

where $a = -\omega_0\langle \mathbf{h}, \mathbf{k}\rangle$, $c = \tilde{f}(q - q_0) + \omega_0^2\langle \mathbf{Gk}, \mathbf{k}\rangle$, and $d = \omega_0(\langle \mathbf{f}, \mathbf{k}\rangle + \langle \mathbf{Hk}, \mathbf{k}\rangle)$. According to Eqs. (32)–(34) for $\mathbf{k} = 0$, when varying the parameter q, two simple imaginary eigenvalues merge at $q = q_0$ and then split in the direction perpendicular to the imaginary axis with the formation of a pair of simple complex eigenvalues (flutter). Such a behavior of the eigenvalues is known as *strong interaction* and is typical for the circulatory system [5]. The trajectories of the eigenvalues of the circulatory system when varying the parameter q are shown in Fig. 1 by the thin lines (for $\tilde{f} < 0$).

For $\mathbf{k} \neq 0$ and $d \neq 0$, dissipative and gyroscopic forces destroy strong interaction by displacing and splitting the trajectories of the eigenvalues of the circu-

latory system, as is shown in Fig. 1a. This effect, which was previously known only qualitatively [2–4], is analytically described by Eqs. (32)–(34). When varying the parameter q at a fixed vector $\mathbf{k}$, the eigenvalues are displaced along the branches of hyperbola (32) on the complex plane. This hyperbola has two asymptotes, $\mathrm{Re}\lambda = -\frac{a}{2}$ and $\mathrm{Im}\lambda = \omega_0$. If $a > 0$, one of the two eigenvalues lies on the left-hand side of the complex plane, and the second eigenvalue is displaced to the right-hand side at the critical load q_{cr} determined by Eq. (27).

For $d = 0$, the strong interaction between eigenvalues holds despite the introduction of weak velocity-dependent forces ($\mathbf{k} \neq 0$). According to Eq. (33), the complex eigenvalues with $\mathrm{Re}\lambda = -\frac{a}{2}$ are strongly coupled with each other for q equal to

$$q_* = q_0 + \omega_0^2 \frac{\langle \mathbf{h}, \mathbf{k}\rangle^2 - 4\langle \mathbf{Gk}, \mathbf{k}\rangle}{4\tilde{f}}. \qquad (35)$$

When varying the parameter q, the double eigenvalue $\lambda_* = -\frac{a}{2} + i\omega_0$ splits into two simple complex-conjugated eigenvalues, one of which intersects the imaginary axis at the critical value given by Eq. (27), as is shown in Fig. 1b for $a > 0$. In this case, weak forces dependent on the generalized velocities stabilize the circulatory system when $\langle \mathbf{Gk}, \mathbf{k}\rangle > 0$.

4. Let us consider the Reut–Sugiyama pendulum [11] consisting of two rigid rods that have the same length l and equal unit-length mass m. The rods are joined together by a hinge. A plane rigid massless plate is fixed in the free end of one rod perpendicularly to it. The pendulum is subject to the force Q always directed along the vertical axis that is the equilibrium position of the pendulum (Fig. 2). This system was realized under laboratory conditions, and the force Q was generated by the pressure of an air jet [11]. Viscoelastic hinges of the pendulum are characterized by the same rigidity c and viscosity b. The external damping coefficient due to air resistance is denoted as e. In the dimensionless quantities

$$q = \frac{Ql}{c}, \quad \gamma = \frac{b}{l\sqrt{cml}}, \quad \kappa = \frac{el^2}{\sqrt{cml}}, \quad \tau = \frac{t}{l}\sqrt{\frac{c}{ml}}, \qquad (36)$$

the equation of small oscillations of the pendulum has the form [11]

$$\ddot{\mathbf{y}} + \mathbf{D}\dot{\mathbf{y}} + \mathbf{A}\mathbf{y} = 0, \qquad (37)$$

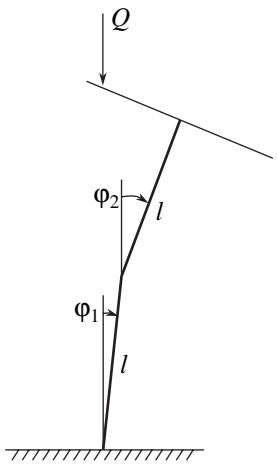

Fig. 2. Reut–Sugiyama pendulum.

where

$$\mathbf{D} = \frac{1}{7}\begin{bmatrix} 7\kappa + 42\gamma & -30\gamma \\ -84\gamma & 7\kappa + 66\gamma \end{bmatrix},$$
$$\mathbf{A} = \frac{1}{7}\begin{bmatrix} 42 - 30q & -30 \\ 66q - 84 & 66 \end{bmatrix}, \quad \mathbf{y} = \begin{bmatrix} \varphi_1 \\ \varphi_2 \end{bmatrix}. \qquad (38)$$

In the absence of dissipation ($\gamma = \kappa = 0$), the equilibrium position of the pendulum is stable if $0 \le q < q_0$. Under the load $q_0 = \frac{18 - 2\sqrt{7}}{5} \simeq 2.54170$ [11], there are a pair of double eigenvalues $\pm i\omega_0$, where $\omega_0 = 6^{1/2}7^{-1/4}$, corresponding to one eigenvector.

The Routh–Hurwitz conditions applied to the system of Eqs. (37) and (38) provides the equation for the boundary of the asymptotic-stability region for $q_{cr} = q_0$ in the form

$$(36\gamma^2 + 108\gamma\kappa + 7\kappa^2)(54\gamma + 7\kappa)(6\gamma + \kappa\sqrt{7})$$
$$= 216(9 - \sqrt{7})^2\gamma^2, \quad \kappa > -\frac{54}{7}\gamma, \quad \kappa > -\frac{6\sqrt{7}}{7}\gamma. \qquad (39)$$

The asymptotic-stability region with the boundary given by Eq. (39) is shaded in Fig. 3. It approaches the origin as a narrow tongue along the vertical axis, which illustrates the stabilizing and destabilizing effects of low external κ and internal γ dampings, respectively [3, 4]. Indeed, Fig. 3 shows that, for any infinitely small γ value, there is a κ value such that the perturbed nonconservative system is stable with $q_{cr}(\gamma, \kappa) > q_0$.

Let us use the above results to approximate the asymptotic-stability region near the origin as well as to describe the behavior of the eigenvalues. Solving prob-

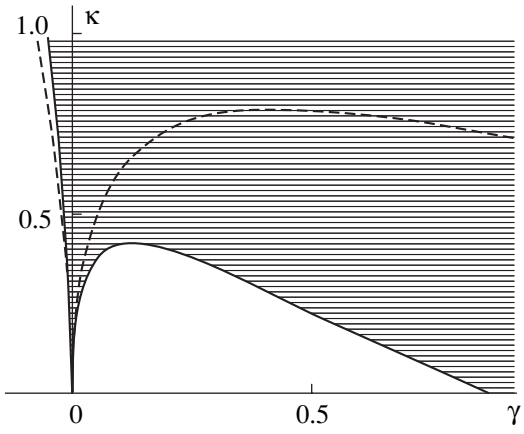

Fig. 3. Asymptotic-stability region is shaded on the plane of the parameters of internal γ and external κ damping for $q_{cr} = q_0$.

lems given by Eqs. (5) and (6) for $q_0 = \frac{18 - 2\sqrt{7}}{5}$ and $\omega_0 = 6^{1/2}7^{-1/4}$ with the matrices **D** and **A** specified by Eqs. (38), we obtain the Jordan vector chains for the double eigenvalue $i\omega_0$:

$$\mathbf{u}_0 = \frac{\sqrt{7}}{140}\begin{bmatrix} -5 \\ 11 - \sqrt{7} \end{bmatrix}, \quad \mathbf{v}_0 = \begin{bmatrix} 11 - \sqrt{7} \\ 5 \end{bmatrix},$$
$$\mathbf{u}_1 = \frac{i\omega_0}{120}\begin{bmatrix} -5 \\ 11 - 3\sqrt{7} \end{bmatrix}, \quad \mathbf{v}_1 = \frac{7i\omega_0}{3}\begin{bmatrix} 1 \\ 0 \end{bmatrix}. \tag{40}$$

The substitution of these vectors into expressions (11), (12), (22), and (23) yields

$$\mathbf{f} = \frac{3}{7}\begin{bmatrix} 9 - \sqrt{7} \\ 0 \end{bmatrix}, \quad \tilde{f} = -\frac{15}{14}, \quad \mathbf{h} = -\frac{\omega_0\sqrt{7}}{42}\begin{bmatrix} 3(9 + \sqrt{7}) \\ 7 \end{bmatrix}, \tag{41}$$
$$\mathbf{H} \equiv 0, \quad \mathbf{G} = \frac{1}{24}\begin{bmatrix} 0 & 3 \\ 3 & \sqrt{7} \end{bmatrix}.$$

In view of expressions (41), expression (27) for the critical load takes the form

$$q_{cr}(\gamma, \kappa) = q_0 - \frac{\sqrt{7}}{30}\frac{216(9 - \sqrt{7})^2\gamma^2}{((9 + \sqrt{7})3\gamma + 7\kappa)^2} + \frac{\sqrt{7}}{30}(6\gamma\kappa + \sqrt{7}\kappa^2). \tag{42}$$

Approximation of the stability-region boundary given by Eq. (39) that follows from Eq. (42) for $q_{cr} = q_0$ is shown by the dashed line in Fig. 3. According to Eq. (42), the critical load for $\gamma = 0$ increases with external damping as $q_{cr} = q_0 + \frac{7\kappa^2}{30}$, which agrees with the shape of the stability region shown in Fig. 3.

The substitution of Eq. (41) into Eqs. (32) and (33) provides explicit expressions describing the trajectories of the eigenvalues on the complex plane as well as the behavior of their real parts when varying the load parameter q:

$$\left(\mathrm{Im}\,\lambda - \omega_0 + \mathrm{Re}\,\lambda + \frac{3(9 + \sqrt{7})\gamma + 7\kappa}{14}\right)^2$$
$$-\left(\mathrm{Im}\,\lambda - \omega_0 - \mathrm{Re}\,\lambda - \frac{3(9 + \sqrt{7})\gamma + 7\kappa}{14}\right)^2$$
$$= \gamma\frac{6(\sqrt{7} - 9)\omega_0}{7}, \tag{43}$$

$$\left(\mathrm{Re}\,\lambda + \frac{3(9 + \sqrt{7})\gamma + 7\kappa}{14}\right)^4$$
$$-\frac{3}{14}\left(5(q - q_0) + \frac{3\gamma}{7}((44 + 9\sqrt{7})\gamma + 21\kappa)\right)$$
$$\times\left(\mathrm{Re}\,\lambda + \frac{3(9 + \sqrt{7})\gamma + 7\kappa}{14}\right)^2 = \gamma^2\frac{27(44\sqrt{7} - 63)}{343}. \tag{44}$$

For $\kappa = \gamma = 0$, the eigenvalues are strongly coupled at $q = q_0$. In the absence of internal damping ($\gamma = 0$), the double eigenvalue is displaced to the left-hand side of the complex plane due to external damping κ stabilizing the circulatory system. In this case, $\tilde{q}_{cr} = q_0$ according to Eqs. (29) and (42). In the absence of external damping ($\kappa = 0$), internal damping γ destroys strong interaction and displaces frequency curves to the left-hand side of the complex plane. In this case, the Reut–Sugiyama pendulum is destabilized by internal damping, and, according to Eqs. (29) and (42), the jump of the critical load for $\gamma \longrightarrow 0$ is equal to

$$\Delta q = \frac{4\sqrt{7}}{5}\frac{44 - 9\sqrt{7}}{44 + 9\sqrt{7}} \simeq 0.63013, \tag{45}$$

which agrees satisfactorily with the exact value $\Delta q = \frac{2(44 - 9\sqrt{7})}{45} \simeq 0.89725$ [11]. The approximate jump value $\Delta q = 0.43733$ for $\frac{\gamma}{\kappa} = 1$ and $\gamma \longrightarrow 0$ is quite close to the exact value $\Delta q = 0.42198$. Thus, the approximation of the critical-load jump by Eqs. (29) and (42) is improved with decreasing the ratio $\frac{\gamma}{\kappa}$ to zero.

ACKNOWLEDGMENTS

I am grateful to A.P. Seyranian for attention to the work and stimulating discussions. This work was supported by the Russian Foundation for Basic Research and National Natural Science Foundation of China (project no. 02-01-39004), Russian Foundation for Basic Research (project no. 03-01-00161), and Basic Research and Higher Education Program administered jointly by the US Civilian Research and Development Foundation for the Independent States of the Former Soviet Union and the Ministry of Education of the Russian Federation (grant no. Y1-MP-06-19).

REFERENCES

1. H. Ziegler, Ing. Archiv. **20**, 49 (1952).
2. V. V. Bolotin, *Nonconservative Problems in the Theory of Elastic Stability* (Fizmatgiz, Moscow, 1961; Pergamon, London, 1965).
3. V. V. Bolotin and N. I. Zhinzher, Int. J. Solids Struct. **5**, 965 (1969).
4. A. P. Seyranian, Usp. Mekh. **13** (2), 89 (1990).
5. A. P. Seyranian, Izv. Ross. Akad. Nauk, Mekh. Tverd. Tela, No. 1, 142 (1994).
6. V. F. Zhuravlev, Izv. Akad. Nauk, Mekh. Tverd. Tela, No. 6, 13 (1992).
7. A. P. Seyranian, Dokl. Akad. Nauk **348**, 323 (1996) [Phys. Dokl. **41**, 214 (1996)].
8. O. N. Kirillov, *How Do Small Velocity-Dependent Forces (De)stabilize a Non-Conservative System?* (Danish Center for Applied Mathematics and Mechanics-DCAMM, Copenhagen, 2003), Rep. No. 681.
9. V. I. Arnold, *Additional Chapters of the Theory of Ordinary Differential Equations* (Nauka, Moscow, 1978; Springer, New York, 1983).
10. H. Bilharz, Z. Angew. Math. Mech. **24**, 77 (1944).
11. Y. Sugiyama, in *Modern Problems of Structural Stability* (Springer, Vienna, 2002), pp. 341–394.

Translated by R. Tyapaev

Doklady Physics, Vol. 49, No. 4, 2004, pp. 246–249. Translated from Doklady Akademii Nauk, Vol. 395, No. 5, 2004, pp. 621–625.

MECHANICS

Incubation Time Criterion and the Pulsed Strength of Continua: Fracture, Cavitation, and Electrical Breakdown

Yu. V. Petrov

Presented by Academician N.F. Morozov November 24, 2003

Received December 19, 2003

Experiments on the dynamic fracture of solids, liquids, conductors, and insulators that is caused by fast intense actions of environment or directed energy fluxes reveal a number of effects indicating a fundamental difference between the fast dynamic rupture (breakdown) of materials and a similar process under slow quasistatic actions. For example, one of the basic problems in testing the dynamic-strength properties of materials is associated with the dependence of the limiting characteristics on the duration, amplitude, and growth rate of an external action, as well as on a number of other factors. Whereas a critical value is a constant for a material in the static case, experimentally determined critical characteristics in dynamics are strongly unstable, and as a result, their behavior becomes unpredictable. The indicated (and some other) features of the behavior of materials subjected to pulsed actions are common for a number of seemingly quite different physical processes, such as dynamic fracture (starting cracks and splitting), cavitation in liquids, and electrical breakdown in solids. In this paper, we analyze examples illustrating typical dynamic effects inherent in the these processes. We propose a unified interpretation for the fracture of solids and liquids and electrical breakdown in insulators using the structural-time approach [1, 2] based on the concept of the fracture incubation time.

CRITERION OF THE FRACTURE INCUBATION TIME

The basic cause of difficulties in modeling the aforementioned effects of mechanical or electrical strength is the absence of an adequate limiting condition that determines the instant of rupture or breakdown. This problem can be solved by using both the structural macromechanics of fracture and the concept of the fracture incubation time, which represents the kinetic processes of the formation of macroscopic breaks [1, 2]. The above effects become essential for actions whose periods are comparable with the scale determined by the fracture incubation time associated with preparatory relaxation processes of developing microdefects in the material structure.

The criterion of the fracture incubation time proposed in [1, 2] makes it possible to calculate effects of the unstable behavior of dynamic-strength characteristics. These effects are observed in experiments on the fracture of solids. This criterion can be generalized in the form of the condition

$$\frac{1}{\tau}\int_{t-\tau}^{t}\left(\frac{F(t')}{F_s}\right)^{\alpha}dt' \le 1. \qquad (1)$$

Here, $F(t)$ is the intensity of a local force field causing the fracture of the medium, F_s is the static limit of the local force field, and τ is the incubation time associated with the dynamics of a relaxation process preparing the break. The fracture time is defined as the time at which condition (1) becomes an equality. The parameter α characterizes the sensitivity of a material to the intensity of the force field causing fracture.

By example of the mechanical break of a material, we now consider one of the possible methods of interpreting and determining the parameter τ. We assume that a standard sample made of a given material under tension is broken into two parts under the stress P arising at a certain time $t = 0$: $F(t) = PH(t)$, where $H(t)$ is the Heaviside step function. In the case of quasi-brittle fracture, the material is unloaded, and the local stress at the break point decreases rapidly (but not instantaneously) from P to 0. In this case, the corresponding unloading wave is generated, propagates over the sample, and can be detected by well-known (e.g., interferometric) methods. The stress variation at the break point can be conditionally represented by the dependence $\sigma(t) = P - Pf(t)$, where the function $f(t)$ varies from 0 to 1 within a certain time interval T. The case $f(t) = H(t)$ corresponds to the classical theory of strength. In other

St. Petersburg State University,
Universitetskaya nab. 7/9, St. Petersburg, 199164 Russia
e-mail: yp@YP1004.spb.edu

1028-3358/04/4904-0246$26.00

words, according to the classical approach, break occurs instantaneously ($T = 0$). In practice, the break of a material (sample) is a process proceeding in time, and the function $f(t)$ describes the kinetics of the passage from a conditionally defect-free state [$f(0) = 0$] to the completely broken state at the given point [$f(T) = 1$] (Fig. 1). Applying fracture criterion (1) to this situation, we arrive at the relation $T = \tau$ for $P = F_s$. In other words, the incubation time introduced above is equal to the duration of the fracture process after the stress in the material has reached the static breaking strength. This duration can be measured in experiments on the static fracture of samples by means of different methods, e.g., by measuring the time of the increase in pressure at the unloading wave front, which is determined by the interferometric method using the velocity profile of points on the sample surface. Below, we analyze examples of the actual realization of criterion (1) in various physicomechanical problems.

FRACTURE OF SOLIDS

A typical example illustrating the complicated behavior of the dynamic strength of solids is the time dependence of strength observed under splitting conditions [4] (see Fig. 2). This dependence of the fracture time t_* on the critical pulse amplitude P_* for different pulse durations shows that the dynamic strength is not a material constant but depends on the time to fracture (i.e., sample "lifetime"). The criterion of critical stress $\sigma(t) \le \sigma_s$, where σ_s is the static strength, describes well long-term quasistatic fracture caused by long-duration wave pulses $\sigma(t) = P\varphi(t)$, where P is the amplitude and $\varphi(t)$ is the time profile function. However, in the case of short-duration pulses, the fracture time weakly depends on the threshold pulse amplitude, and this dependence has a certain asymptote. This effect is called the phenomenon of the mechanical branch of the strength time dependence. Neither the conventional theory of strength nor known time criteria explain this phenomenon.

The total time dependence of strength can be obtained on the basis of incubation time criterion (1). For the splitting fracture under consideration, this criterion takes the form of the limiting condition previously proposed in [3]:

$$\frac{1}{\tau}\int_{t-\tau}^{t}\sigma(t')dt' \le \sigma_s, \qquad (2)$$

where $\sigma(t)$ is the time dependence of the local stress at the break point. The scheme for the application of criterion (2) to splitting problems is given in [2, 3]. An example of a calculation using criterion (2) for the time dependence of the strength of aluminum ($\tau = 0.75$ μs, $\sigma_s = 103$ MPa) for triangular pulses realized in the experiments reported in [4] is represented in Fig. 2 by the solid curve.

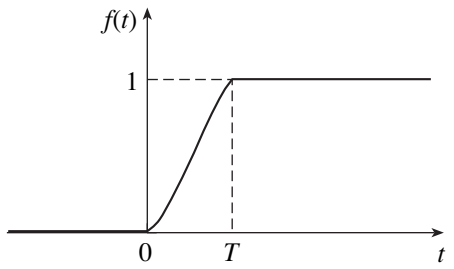

Fig. 1. Schematic kinetics of the fracture of a sample at the break point.

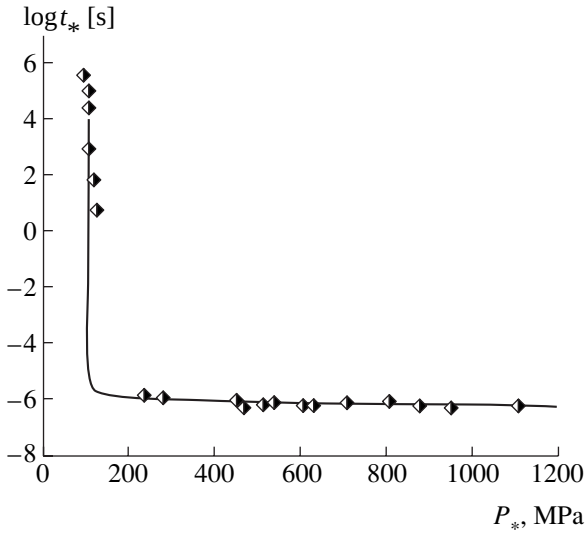

Fig. 2. Logarithm of the fracture-process duration t_* vs. the threshold amplitude P_* of a stress pulse that causes splitting in an aluminum sample [4].

Effects in the behavior of the dynamic fracture toughness [2] can be analyzed in a similar manner. Rate dependences K_{Id} of the dynamic fracture toughness, which were observed in experiments, are characterized by a strong instability and can noticeably change when varying the duration of the load rise stage, the shape of the time profile of a loading pulse, sample geometry, and the method of load application [5–7]. The calculations based on the concept of the incubation time corresponding to the conditions of a number of experiments were carried out in [8]. The results show that the dynamic fracture toughness is not an intrinsic characteristic of a material. Therefore, the employment of both the criterion of the critical intensity coefficient $K_I(t) \le K_{Id}$ and the characteristic K_{Id} as a material parameter defining the dynamic fracture (in analogy to the static parameter K_{Is}) is incorrect.

CAVITATION IN LIQUIDS

Cavitation is the violation of the continuity of a liquid (i.e., the initial stage of fracture) in the field of ten-

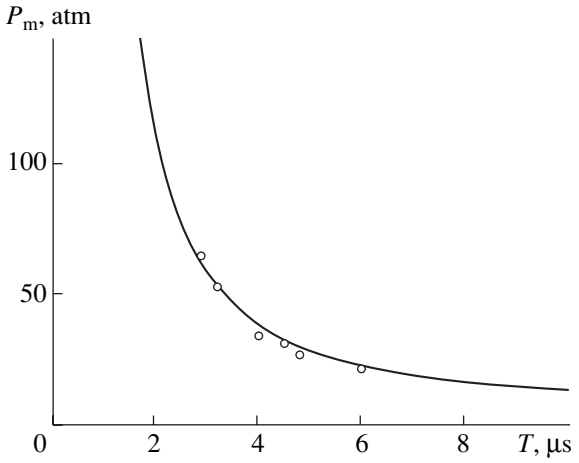

Fig. 3. Mechanical strength measured and calculated for water as a function of the pulse duration [11].

sile stresses. This phenomenon is accompanied by the growth of vapor bubbles on cavitation nuclei, which are virtually always present in liquids in the form of microscopic bubbles of free gas, microparticles, or their combinations [9, 10]. One of the parameters characterizing the cavitation strength of water is the cavitation threshold. This threshold is a certain negative pressure above which cavitation nuclei intensely grow, and as a consequence, the dynamics of the free surface of the liquid, the intensity of light scattering, etc., change abruptly.

Figure 3 shows the experimental data obtained by Besov *et al.* [11] by using the capacity method of detecting the cavitation threshold through the dynamics of the free surface of the liquid when a shock wave is reflected from this surface. According to this procedure, the shock wave is produced in a shock tube by a pressure of a pulsed magnetic field onto the conducting membrane transferring the pressure pulse to the liquid. The pressure pulse that was realized in the experiment with water and caused the cavitation on the free surface had the form

$$\sigma(t) = -P_A \sin\left(\frac{\pi t}{T}\right) e^{-\frac{t}{T_1}}, \quad T_1 = 2.85 \times 10^{-6}\ \text{s}.$$

The maximum pulse amplitude P_m was reached at the time $t = \frac{T}{\pi}\arctan\left(\frac{\pi T_1}{T}\right)$ and determined by the formula

$$P_m = \frac{\pi T_1}{\sqrt{T^2 + \pi^2 T_1^2}} \exp\left(\frac{T}{\pi T_1}\arctan\left(\frac{\pi T_1}{T}\right)\right).$$

In order to analyze the initial stage of the cavitation fracture, we make use of incubation time criterion (1). In this case, we take into account that tensile stresses in mechanics of a deformed body are positive, whereas tensile pressures in liquids are negative. In addition, compressing pressure must be taken into account. Therefore, condition (1) for a liquid takes the form

$$\frac{1}{\tau}\int_{t-\tau}^{t} \operatorname{sgn}(\sigma(t'))\left(\operatorname{abs}\left(\frac{\sigma(t')}{\sigma_s}\right)\right)^{\alpha} dt' \le 1. \qquad (3)$$

The strength of water, which was calculated in accordance with criterion (3), is shown by the solid curve in Fig. 3 as a function of the pulse duration T for σ_s = 1 atm, $\alpha = 0.5$, and $\tau = 19$ μs [11].

Thus, the experiments show that the cavitation strength of liquids increases nonlinearly with decreasing loading-pulse duration. Using the incubation time criterion makes it possible to calculate the experimentally observed increase in the cavitation threshold with decreasing the pulse duration.

ELECTRICAL BREAKDOWN IN INSULATORS

The above effects are also observed in pulsed electrical breakdown in insulators, which is an urgent problem in the development and exploitation of high-voltage facilities and other electrical equipment. For example, the typical feature of pulsed breakdown is an increase in the breakdown voltage with reducing pulse duration. The breakdown channel in alkali-halide crystals, which is produced by a pulsed electric field with a duration of 10 ns, arises at voltages exceeding quasistatic ones by several times (i.e., with durations of 1 μs and more) [12]. The same effect is typical of ionic compounds. As an example, the breakdown electric field E^* measured in [13] for ammonium perchlorate single crystals is presented in Fig. 4 as a function of the duration t_0 of the leading edge of the pulse. This dependence also characterizes the electrical strength as a function of the voltage growth rate in a sample and can be called the time dependence of strength by analogy with the above examples of splitting, starting cracks, and cavitation. In the experiment reported in [13], thin single-crystal ammonium perchlorate plates were placed in a pulsed electric field. The electrical breakdown of samples resulted in their burning out accompanied by the appearance of a through channel. The experimental data shown in Fig. 4 correspond to distances between electrodes of 0.01 and 0.03 cm. As is seen, for times $t_0 \le 1.5$ μs, the electrical strength of a material increases with a reduction in the duration of the leading edge of a voltage pulse (with an increase in the voltage growth rate in a sample). For $t_0 > 1.5$ μs, the breakdown electric field becomes virtually independent of t_0.

In the case under consideration, the electrical-breakdown criterion corresponding to relationship (1) can be written in the form

$$\frac{1}{\tau}\int_{t-\tau}^{t} E(t')dt' \le E_s. \qquad (4)$$

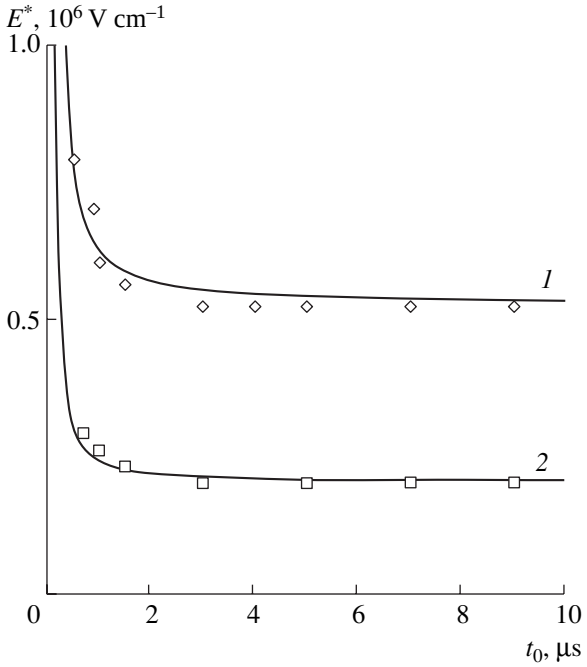

Fig. 4. Electrical strength E^* of ammonium perchlorate vs. the duration t_0 of the leading edge of an electrical pulse for the interelectrode distance L = (*1*) 0.1 and (*2*) 0.03 cm [13].

Here, E_s is the static electrical strength of a material, which can depend on the interelectrode distance, and τ is the incubation time for the electrical breakdown of the material, which is determined by the kinetics of the electron multiplication in the electric discharge. The curves in Fig. 4 are the time dependences for the electrical strength of ammonium perchlorate calculated according to criterion (4) with the parameters τ = 0.33 μs and $E_s = 0.52 \times 10^6$ and 0.2×10^6 V cm^{-1} for L = 0.01 and 0.03 cm, respectively. The onset time of increasing the breakdown field in the dependences plotted in Fig. 4 is entirely determined by the τ value. As was shown in [13], this time was virtually independent of the interelectrode distance. This indicates that the incubation time in the case under discussion may be considered as a material characteristic.

Thus, the examples of different physical processes considered above show the fundamental importance of investigating incubation processes preparing abrupt structural changes (fracture and phase transitions) in continua under intense pulsed actions. The fracture incubation time is evidently a universal basic characteristic of the dynamic strength and must become one of the main material parameters to be experimentally determined (measured). The above results show that the structural-time approach is fundamental and makes it possible to adequately represent the dynamics of both the fracture of solids and liquids and electrical breakdown in insulators.

ACKNOWLEDGMENTS

This work was supported by the Russian Foundation for Basic Research (project nos. 02-01-01035 and 03-01-39010), the Swiss National Science Foundation, and NATO Scientific Affairs Division.

REFERENCES

1. Yu. V. Petrov, Dokl. Akad. Nauk SSSR **321**, 66 (1991) [Sov. Phys. Dokl. **36**, 802 (1991)].
2. N. Morozov and Y. Petrov, *Dynamics of Fracture* (Springer, Berlin, 2000).
3. N. F. Morozov, Yu. V. Petrov, and A. A. Utkin, Dokl. Akad. Nauk SSSR **313**, 276 (1990) [Sov. Phys. Dokl. **35**, 646 (1990)].
4. N. A. Zlatin, S. M. Mochalov, G. S. Pugachev, and A. M. Bragov, Fiz. Tverd. Tela (Leningrad) **16**, 1752 (1974) [Sov. Phys. Solid State **16**, 1137 (1974)].
5. K. Ravi-Chandar and W. G. Knauss, Int. J. Fract. **25**, 247 (1984).
6. J. F. Kalthoff, Int. J. Fract. Mech. **23**, 289 (1986).
7. J. W. Dally and D. B. Barker, Exp. Mech. **28**, 298 (1988).
8. N. F. Morozov and Yu. V. Petrov, Izv. Ross. Akad. Nauk, Mekh. Tverd. Tela, No. 6, 100 (1993).
9. A. S. Besov, V. K. Kedrinskiĭ, Y. Matsumoto, *et al.*, Din. Sploshnoĭ Sredy, No. 104, 16 (1992).
10. M. Kornfel'd, *Elasticity and Strength of Liquids* (GIIL, Moscow, 1951).
11. A. S. Besov, V. K. Kedrinskiĭ, N. F. Morozov, *et al.*, Dokl. Akad. Nauk **378**, 333 (2001) [Dokl. Phys. **46**, 363 (2001)].
12. A. A. Vorob'ev and G. A. Vorob'ev, *Electrical Breakdown and Destruction of Solid Dielectrics* (Vysshaya Shkola, Moscow, 1966).
13. I. G. Khaneft and A. V. Khaneft, Zh. Tekh. Fiz. **70** (4), 42 (2000) [Tech. Phys. **45**, 423 (2000)].

Translated by G. Merzon

Doklady Physics, Vol. 49, No. 4, 2004, pp. 250–255. Translated from Doklady Akademii Nauk, Vol. 395, No. 6, 2004, pp. 761–766.

MECHANICS

Hydromechanical Calculation of Free Filtration from Watercourses of a Curvilinear Profile with the Shifted Thalweg

K. N. Anakhaev

Presented by Academician S.S. Grigoryan November 1, 2003

Received November 18, 2003

Watercourses in the form of channels, storages, reservoirs, etc., often have curvilinear profiles, and filtration in them under the corresponding conditions can be characterized as free. This problem in application to symmetric watercourses with the central thalweg was considered in the hydromechanical formulation by using the semi-inverse method in [1–5]. In this case, Vedernikov and Pavlovskiĭ assumed the initial ring base of the profile of a watercourse in the plane of the Joukowski complex [2–5]:

$$\theta = z - iW = (x + \psi) + i(y - \varphi) = \theta_1 + i\theta_2. \quad (1)$$

Here, $z = x + iy$ is the complex filtration zone with the current coordinates x and y (Fig. 1); $W = \varphi + i\psi$ is the region of the reduced complex potential with the coordinates of the pressure head function $\varphi = \frac{\varphi_n}{k}$ and stream function $\psi = \frac{\psi_n}{k}$ with the specific filtration rate from the watercourse $Q = \frac{Q_n}{k}$ (Fig. 2e), where quantities with the subscript n are real values of these parameters and k is the ground filtration coefficient [5]; and

$$\theta_1 = x + \psi, \quad \theta_2 = y - \varphi \quad (2)$$

are the coordinates of the Joukowski complex region (Fig. 2a).

Unfortunately, these solutions enable one to determine the filtration parameters for a given B/H ratio, where B and H are the width and depth of the watercourse, only for the symmetric profile of the watercourse. Meanwhile, most real watercourses have asymmetric profiles with the shifted thalweg (point A). In view of this circumstance, we consider the initial curvilinear profile of a watercourse with the thalweg located at a depth of $H = 1$ (in arbitrary units) and is shifted from the watercourse axis by a varying in the interval $-\frac{B}{2} \le a \le \frac{B}{2}$ (Fig. 1). In this case, the stream function ψ increases from $\psi = -\frac{Q}{2}$ at point *1* to $\psi = \frac{Q}{2}$ at point *2*, and $\psi_N = 0$ at point N on the watercourse profile. The width of the filtration flow between points *3* and *4* for $y \longrightarrow \infty$ is equal to $b_\infty = Q$, because the head gradient tends to unity. Thus specified filtration zone *1–A–N–2–3–4* is represented in the lower half-plane of the Joukowski complex in the form of a unit semicircle (Fig. 2a) whose characteristic points are as follows:

points *1* and *2*:

$$x = \pm\frac{B}{2}, \quad y = 0, \quad \psi = \mp\frac{Q}{2}, \quad \varphi = 0,$$

$$\theta_1 = \mp\frac{Q - B}{2}, \quad \theta_2 = 0;$$

point *A*:

$$x = a, \quad y = H = 1, \quad \psi = \psi_A = -a,$$

$$\varphi = 0, \quad \theta_1 = 0, \quad \theta_2 = H = 1; \quad (3)$$

point *N*:

$$x = x_N, \quad y = y_N, \quad \psi = \psi_N = 0, \quad \varphi = 0;$$

$$\theta_1 = x_N, \quad \theta_2 = y_N;$$

points *3* and *4*:

$$x = \pm\frac{Q}{2} + b, \quad y = \infty, \quad \psi = \pm\frac{Q}{2},$$

$$\varphi = \infty, \quad \theta_1 = b, \quad \theta_2 = 0,$$

where the upper signs correspond to points *1* and *3*, and the lower signs, to points *2* and *4*.

In Eqs. (3), it is taken that the stream function at the point A is equal to the negative shift of the thalweg from the axis of the watercourse, $\psi_A = -a$, and the shift b of

Kabardino-Balkar State Agricultural Academy, ul. Tolstogo 185, Nalchik, 360004 Russia

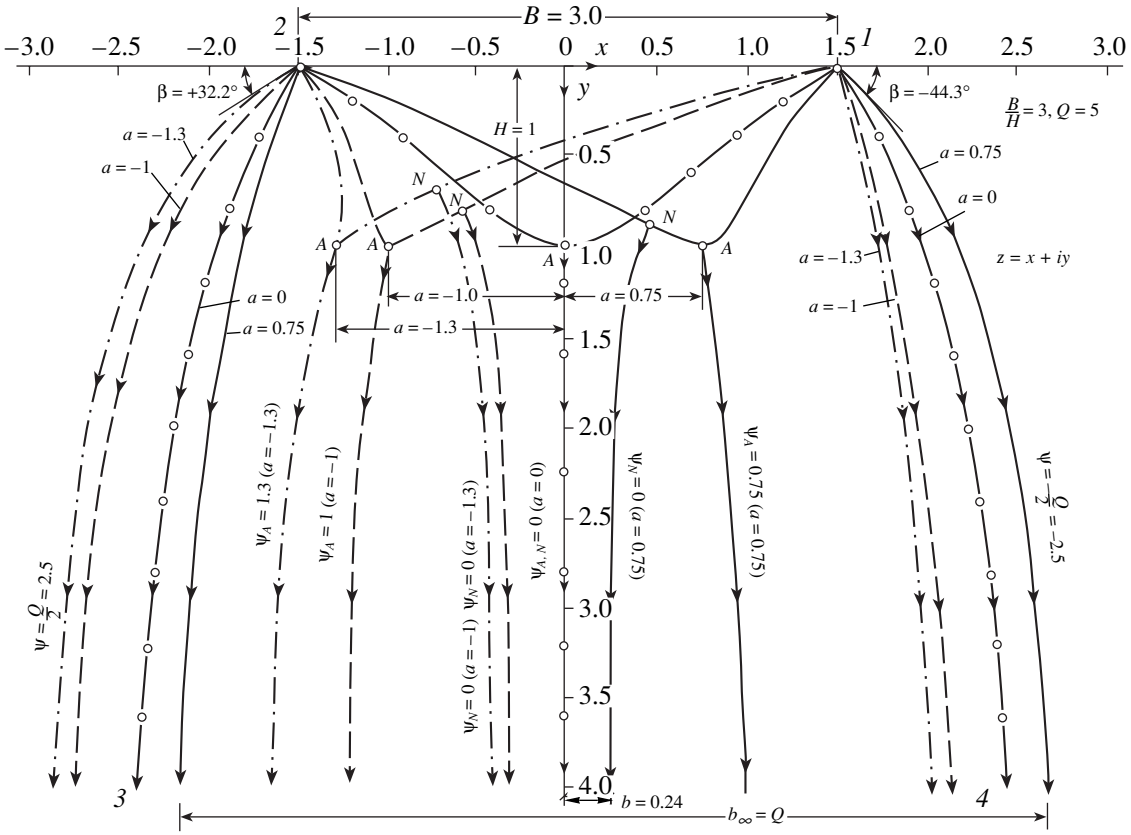

Fig. 1. Free filtration from a watercourse of a curvilinear profile for $\frac{B}{H}$ = 3 and thalweg shift a = 0.75, 0, –1.0, –1.3.

the zero streamline ($\psi_N = 0$) from the vertical Oy axis is given by the expression (as will be shown below)

$$b = \tan\frac{0.5a\pi}{Q}. \quad (4)$$

From relations (3) for points *1*, *2*, and *A* in the region θ, we find the filtration rate

$$Q = B + 2H, \quad (5)$$

which is also equal to the maximum width b_∞ of the filtration zone.

The semicircle region $\theta = \theta_1 + i\theta_2$ is conformally mapped onto a similar unit semicircle in the complex half-plane $t = t_1 + it_2$ (Fig. 2b) by the linear fractional transformation

$$t = \frac{b - \theta}{\theta b - 1}, \quad (6)$$

which transfers points *3* and *4* to the coordinate origin and point *N* onto the Ot_1 axis. From this condition, we obtain the images of the point *N* in the θ and *Z* regions:

$$\theta_N = z_N = \theta_1 + i\theta_2 = x_N + iy_N = \frac{2b}{1 + b^2} + i\frac{1 - b^2}{1 + b^2}. \quad (7)$$

Points *1* and *2* correspond to t = –1 and 1, respectively; points *3* and *4*, to t = 0; the point *A*, to $t_A = t_1 + it_2 = -\frac{2b}{1 + b^2} + i\frac{1 - b^2}{1 + b^2}$; and the point *N*, to $t_N = i$.

Further transformations are performed as follows. The $t = t_1 + it_2$ region is mapped by the inversion

$$\varsigma_0 = -\frac{1}{t} \quad (8)$$

onto the upper half-plane $\varsigma_0 = \xi_0 + i\eta_0$ with a unit semicircle hole (Fig. 2c). The $\varsigma_0 = \xi_0 + i\eta_0$ region is mapped by the Joukowski function

$$\varsigma = 0.5\left(\varsigma_0 + \frac{1}{\varsigma_0}\right) \quad (9)$$

onto the upper half-plane $\varsigma = \xi + i\eta$ (Fig. 2d). The region of the complex potential $W = \varphi + i\psi$ is mapped by the function

$$W_1 = \frac{i\pi W}{Q} \quad (10)$$

onto the half-band $W_1 = \psi_1 + i\varphi_1$ with the width π that

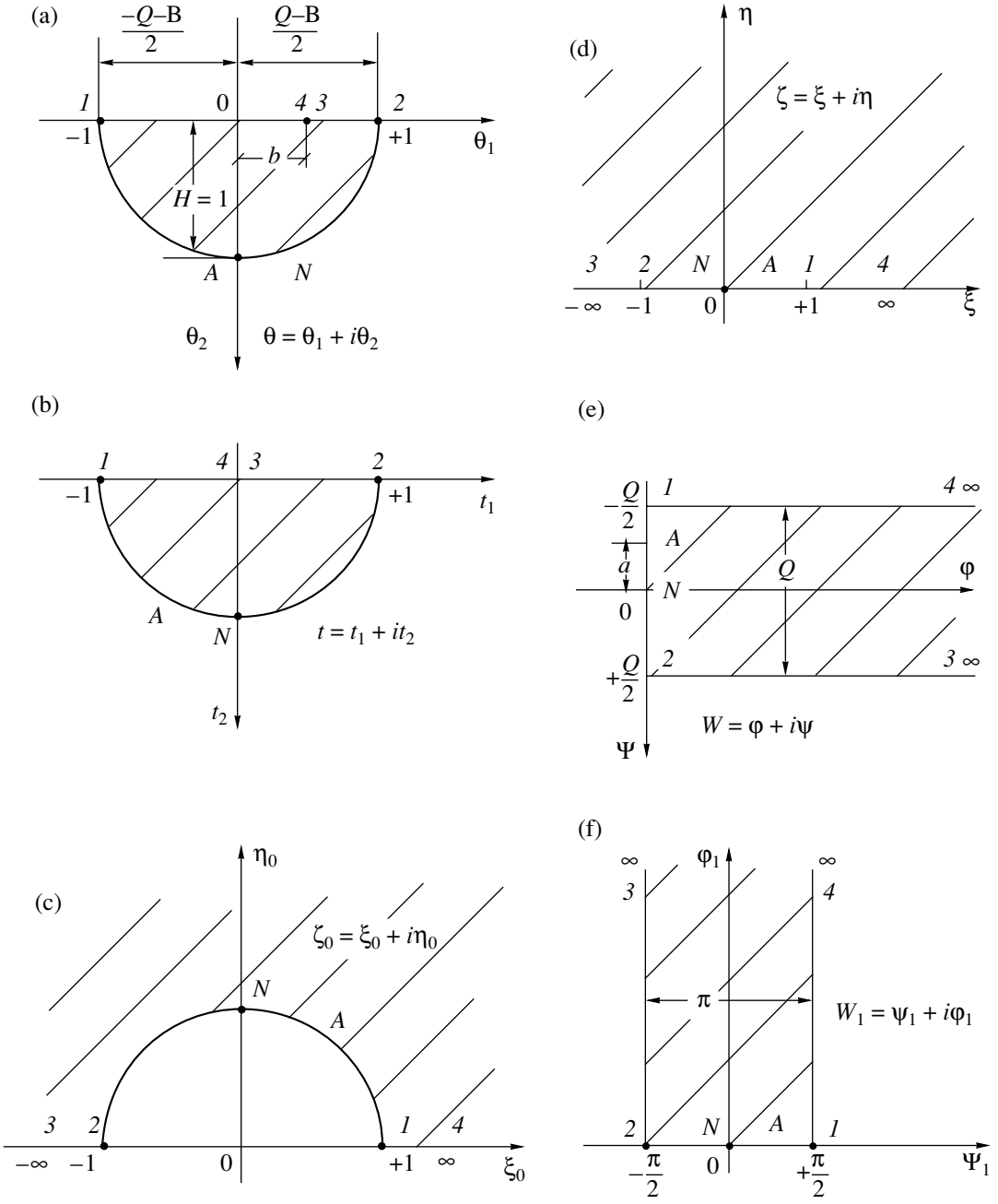

Fig. 2. Scheme of the sequential conformal mappings of the region of the Joukowski complex $\theta = \theta_1 + i\theta_2$ onto the region of the complex potential $W = \varphi + i\psi$.

is in turn mapped onto the upper half-plane

$$\zeta = \sin W_1. \tag{11}$$

Thus, the W and θ regions are related as

$$W = i\frac{Q}{\pi}\arcsin\left[\frac{1}{2}\left(\frac{\theta b - 1}{b - \theta} + \frac{b - \theta}{\theta b - 1}\right)\right]. \tag{12}$$

Separating the real and imaginary parts, we obtain

$$\varphi = \frac{Q}{\pi}\operatorname{arccosh}\frac{M}{2}, \quad \psi = -\frac{Q}{\pi}\arcsin\frac{2\xi}{M}. \tag{13}$$

Here,

$$M = \sqrt{(1+\xi)^2 + \eta^2} + \sqrt{(1-\xi)^2 + \eta^2},$$

$$\xi = \frac{\xi_0(\xi_0^2 + \eta_0^2 + 1)}{2(\xi_0^2 + \eta_0^2)}, \quad \eta = \frac{\eta_0(\xi_0^2 + \eta_0^2 - 1)}{2(\xi_0^2 + \eta_0^2)}, \tag{14}$$

$$\xi_0 = -\frac{t_1}{t_1^2 + t_2^2}, \quad \eta_0 = \frac{t_2}{t_1^2 + t_2^2},$$

$$t_1 = \frac{(b-\theta_1)(\theta_1 b-1)-b\theta_2^2}{(\theta_1 b-1)^2+b^2\theta_2^2}, \quad t_2 = \frac{\theta_2(1-b^2)}{(\theta_1 b-1)^2+b^2\theta_2^2},$$

where θ_1 and θ_2 are given by Eqs. (2). According to Eqs. (14) for $\eta = 0$, $M = 2$, $\psi = -\frac{Q}{\pi}\arcsin\xi$, and $\varphi = 0$ for $\xi < 1$, whereas and $M = 2$, $\psi = \mp\frac{Q}{2}$, and $\varphi = \frac{Q}{\pi}\operatorname{arccosh}|\xi|$ for $|\xi| \geq 1$ (the upper and lower signs correspond to positive and negative ξ values, respectively). The quantity b given by Eq. (4) is determined by the mutual mapping of the values fixed for the point A in the regions W and θ.

The hydromechanical method proposed above for solving the problem of free filtration from watercourses with the shifted thalweg provides the determination of all the necessary parameters of a filtration flow. In particular, for given quantities B, H, and a, the coordinates of the watercourse profile are determined by the formulas

$$x = \frac{2b+(1+b^2)\sin\alpha}{1+b^2+2b\sin\alpha} - \psi, \qquad y = \frac{(1-b^2)\cos\alpha}{1+b^2+2b\sin\alpha}, \tag{15}$$

where $\alpha = \frac{\pi\psi}{Q}$ and ψ is the given stream function.

Depression surfaces *1–4* and *2–3* (Fig. 1) are determined by the relation

$$y = \frac{Q}{\pi}\operatorname{arccosh}\left|\frac{\left[\left(x\mp\frac{Q}{2}\right)b-1\right]^2+\left[b-\left(x\mp\frac{Q}{2}\right)\right]^2}{2\left[\left(x\mp\frac{Q}{2}\right)b-1\right]\left[b-\left(x\mp\frac{Q}{2}\right)\right]}\right|, \tag{16}$$

where the upper and lower signs correspond to the *1–4* and *2–3* sections, respectively. Formulas (15) and (16) for $a = b = 0$ give solutions for the particular case of a symmetric watercourse with the central thalweg.

The filtration velocity V at the moistened perimeter *1–A–2* of the watercourse is given by the expression

$$V = \frac{d\psi}{ds} = \left(\left(\frac{\partial x}{\partial\psi}\right)^2+\left(\frac{\partial y}{\partial\psi}\right)^2\right)^{-1/2}, \tag{17}$$

where ds is an elementary section of the watercourse profile. In view of Eqs. (15), formula (17) takes the form

$$V = \frac{Q}{\pi}\left(\left[\frac{(1-b^2)^2\cos\alpha}{(1+b^2+2b\sin\alpha)^2}-\frac{Q}{\pi}\right]^2 + \left[(1-b^2)\frac{2b+(1+b^2)\sin\alpha}{(1+b^2+2b\sin\alpha)^2}\right]^2\right)^{-1/2}. \tag{18}$$

According to Eq. (18) for $\psi = -\frac{Q}{2}, \frac{Q}{2}, -a$, and 0, the filtration velocities at points *1*, *2*, *A*, and *N*, respectively, are given by the expressions

$$V_{1,2} = \left(1+\left(\frac{\pi}{Q}\frac{1\pm b}{1\mp b}\right)^2\right)^{-1/2}, \quad V_A = \left(1-\frac{\pi}{Q}\frac{1+b^2}{1-b^2}\right)^{-1}, \quad V_N = \left(1-\frac{\pi}{Q}\left(2-\frac{\pi}{Q}\right)\left(\frac{1-b^2}{1+b^2}\right)^2\right)^{-1/2}, \tag{19}$$

where the upper and lower signs stand for positive and negative x values, respectively.

The expressions for the particular case of a symmetric watercourse with the central thalweg are obtained from Eqs. (18) and (19) with $a = b = 0$:

$$V = \left(1-\frac{\pi}{Q}\left(2\cos\alpha-\frac{\pi}{Q}\right)\right)^{-1/2}, \qquad V_{1,2} = \frac{Q}{\sqrt{Q^2+\pi^2}}, \quad V_{A,N} = \frac{Q}{Q-\pi}. \tag{20}$$

These expressions coincide with the rigorous results obtained by Vedernikov [4, p. 121] and Pavlovskiĭ [5, p. 457].

The inclination angle β of the filtration velocity from the horizontal line to the surface of the moistened perimeter *1–A–2* of the watercourse is determined by the expression

$$\beta = \arctan\frac{dx}{dy} = \arctan\left(\frac{dx}{d\psi}\frac{d\psi}{dy}\right),$$

which is reduced, by using Eqs. (13)–(15), to

$$\beta = \arctan\frac{Q\cdot\pi^{-1}(1+b^2+2b\sin\alpha)^2-(1-b^2)^2\cos\alpha}{[2b+(1+b^2)\sin\alpha](1-b^2)}, \tag{21}$$

where the negative and positive β values correspond to the clockwise and counterclockwise inclinations,

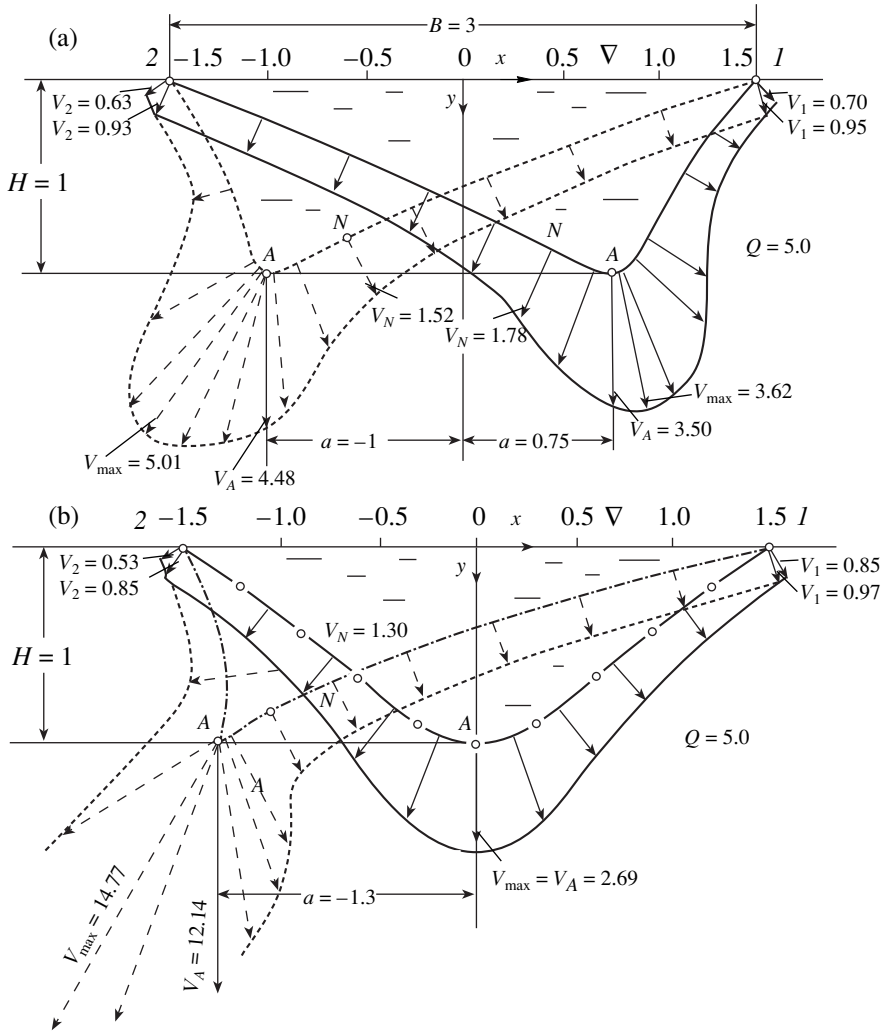

Fig. 3. Diagrams of the inlet filtration velocities in watercourses with curvilinear profiles for $\frac{B}{H} = 3$ and thalweg shift a = (a) 0.75 and –1.0, as well as a = (b) 0 and –1.3.

respectively. The angle β at points *1* and *2* is obtained from Eq. (21) for $y = 0$:

$$\beta_{1,2} = \arctan\left[\frac{Q}{\pi}\frac{(1 \mp b)^2}{b^2 \mp 1}\right], \qquad (22)$$

where the upper and lower signs stand for points *1* and *2*, respectively. The solution for the watercourse with the central thalweg is obtained from Eqs. (21) and (22) for $a = b = 0$:

$$\beta = \arctan\frac{Q \cdot \pi^{-1} - \cos\alpha}{\sin\alpha} = \arctan\frac{Q \cdot \pi^{-1} - y}{\mp\sqrt{1 - y^2}},$$
$$\beta_{1,2} = \mp\arctan\frac{Q}{\pi}, \qquad (23)$$

where the upper and lower signs are used for positive and negative x values, respectively. For this solution, the velocity is vertical ($\beta = 90°$) at the point A ($y = 1$).

Figure 1 shows the curvilinear profiles of the watercourse that are calculated by the above formulas for $B = 3$ and $H = 1$, as well as the thalweg shift $a = 0.75$, –1.0, –1.3, and 0. The corresponding depression surfaces *1–4* and *2–3*, as well as zero streamlines ($\psi_N = 0$) and streamlines from the thalweg A ($\psi_A = -a$), are plotted. For a symmetric watercourse with the central thalweg (for $a = b = 0$), the profile with the depression surfaces coincides with the rigorous solutions obtained by Vedernikov and Pavlovskiĭ [2–5]. Comparison shows that the depression surfaces for asymmetric profiles deviate from those for the symmetric profile by 40–45% or more.

Figure 3 shows diagrams of the filtration velocities for the curvilinear profiles of watercourses for $a = 0.75$,

–1.0, –1.3, and 0. These diagrams show that the maximum inlet filtration velocities for asymmetric watercourses are much higher (by a factor of 2–3 or more) than the values for symmetric profiles for the same filtration rates from them. In addition, these maximum filtration velocities are shifted from the watercourse thalweg (point A) towards the steeper bank (e.g., for $\frac{B}{H} = 10$, this shift can reach 20%). Moreover, the filtration velocities (and inclination angles β) at points *1* and *2* for gentle banks are higher than the values for steep banks.

The results obtained in this work may be used when designing various watercourses, in particular, for the efficient arrangement of filtration-preventing systems, determination of the zone of filtration pollutions from reservoirs, etc.

REFERENCES

1. J. Kozeny, Wasserkraft und Wasserwirtschaft **26** (3), 28 (1931).
2. V. V. Wedernikow, Wasserkraft und Wasserwirtschaft **29** (12), 137 (1934).
3. V. V. Vedernikov, *Filtration from Channels* (ONTI, Moscow, 1934).
4. V. V. Vedernikov, *Filtration Theory in Application to Irrigation and Drain* (GSI, Moscow, 1939).
5. N. N. Pavlovskiĭ, *A Collection of Works*, Vol. 2: *The Motion of Ground Waters* (Izd. Akad. Nauk SSSR, Moscow, 1956).

Translated by R. Tyapaev

Doklady Physics, Vol. 49, No. 4, 2004, pp. 256–260. Translated from Doklady Akademii Nauk, Vol. 395, No. 6, 2004, pp. 767–771.

MECHANICS

Aerodynamic Focusing of Polydisperse Particles in Dusty Gas Flows Past Bodies

L. A. Egorova, A. N. Osiptsov, and V. I. Sakharov

Presented by Academician G.G. Chernyĭ December 18, 2003

Received December 23, 2003

The investigation of interaction between aerodispersed flows and solid surfaces is of considerable interest due to the numerous engineering applications, such as the thermal and erosion protection of flying vehicles moving in the Earth's atmosphere and in the atmospheres of other planets. When a high-speed flying vehicle passes through either aerosol or dust clouds, both local (e.g., local friction coefficient and heat-transfer coefficient) and global flow characteristics can change [1, 2]. Low-inertia particles are accumulated in the boundary layer, which significantly increases the heating of the front surface of the vehicle even for very low concentrations of particles in the free stream [3]. Spatial inhomogeneities in either concentration or inertial properties (such as size, form, and density) of the particles in the free stream can give rise to nonstationary effects in the shock layer as well as to the appearance of peak thermal and force loads. The investigation of this problem was begun in [4, 5], where a number of model inhomogeneities in the concentration and sizes of particles were considered in the range of parameters corresponding to the absence of inertial deposition of particles (low-inertia particles) on the front surface of a body immersed in a flow.

Below, we consider the range of parameters corresponding to the regime of inertial deposition of particles on a sphere in a supersonic dusty flow. It is shown that the front surface of the sphere can be subjected to peak thermal loads caused by aerodynamic focusing of particles with different inertial properties. We demonstrate that the unlimited cumulation (in the framework of the collisionless model of particles) of the momentum and energy of the particles in the shock layer of a blunt body immersed in a flow occurs for certain spatial distributions of the particles in the inertia parameter in the free stream.

Institute of Mechanics, Moscow State University, Michurinskiĭ pr. 1, Moscow, 119192 Russia
e-mail: egorova@imec.msu.ru, osiptsov@imec.msu.ru, sakharov@imec.msu.ru

FORMULATION OF THE PROBLEM AND THE METHOD OF ITS SOLUTION

We consider a flow past a sphere of radius L that moves with a constant supersonic velocity U and enters an inhomogeneous dust layer at the time instant $t = 0$. In the reference frame fixed to the body, the problem is time-dependent due to the time-dependent boundary conditions on the bow shock wave. We use the two-continuum model of a dusty gas [6] with a low mass concentration of particles whose effect on the parameters of the carrier phase in the shock layer is ignored. A viscous perfect gas with constant heat capacities is considered as the carrier phase, where spherical particles each with radius σ and mass m have concentration n_s^*. In general, these parameters are different at different points of the initial dust layer and are treated as known functions of the initial coordinates.

In what follows, the subscript s denotes the parameters of the dispersed phase, the subscript ∞ refers to the parameters of the free stream, and the subscript c denotes the parameters of the adiabatic gas drag that correspond to the limiting ($M \longrightarrow \infty$) hypersonic speed of the flow (M is the Mach number of the gas in the unperturbed flow). The dimensional parameters are denoted by asterisks in order to distinguish them from the dimensionless ones.

The expressions describing the interphase exchange by momentum and energy (per particle) are taken in the form [7]

$$\mathbf{f}_s = 6\pi\sigma\mu^*(\mathbf{V}^* - \mathbf{V}_s^*)G, \quad q_s = 4\pi\sigma\lambda^*(T^* - T_s^*)D,$$

$$G = \left(1 + \frac{\mathrm{Re}_s^{2/3}}{6}\right)\Phi_1(\mathrm{M}_s, \mathrm{Re}_s),$$

$$D = (1 + 0.3\mathrm{Pr}^{1/3}\mathrm{Re}_s^{1/2})\Phi_2(\mathrm{M}_s, \mathrm{Re}_s),$$

$$\mathrm{M}_s = \frac{|\mathbf{V}^* - \mathbf{V}_s^*|}{a^*},$$

1028-3358/04/4904-0256$26.00 © 2004 MAIK "Nauka/Interperiodica"

$$\mathrm{Re}_s = \mathrm{Re}_{s0}\frac{\rho^*\mu_c^*|\mathbf{V}^* - \mathbf{V}_s^*|}{\rho_c^*\mu^* U}, \quad \mathrm{Re}_{s0} = \frac{2\sigma U\rho_c^*}{\mu_c^*},$$

$$\Phi_1 = \frac{1}{\varphi}(1 + \exp(-0.427\mathrm{M}_s^{-4.63} - 3\mathrm{Re}_s^{-0.88})),$$

$$\Phi_2 = \left(1 + 3.42\frac{\mathrm{M}_s}{\mathrm{Re}_s}\frac{1 + 0.3\mathrm{Re}_s^{1/2}\mathrm{Pr}^{1/3}}{\mathrm{Pr}}\right)^{-1},$$

$$\varphi = 1 + \frac{\mathrm{M}_s}{\mathrm{Re}_s}\left(3.82 + 1.28\exp\left(-1.25\frac{\mathrm{Re}_s}{\mathrm{M}_s}\right)\right).$$

Here, $\mathbf{V}^*$ is the velocity; T^* is the temperature; μ^* and λ^* are the viscosity and thermal conductivity of the gas, respectively; a^* is the speed of sound in the gas; Pr is the Prandtl number of the carrier phase; Re_s and M_s are the Reynolds and Mach numbers of the flow past the particles; and the characteristic Reynolds number Re_{s0} of the flow past the particle moving in the shock layer characterizes the deviation of the drag force from Stokes' law. The functions φ and Φ_2 describe the corrections on the finite Knudsen numbers of the flow past the particles $\left(\mathrm{Kn}_s \approx 1.255\sqrt{\gamma}\frac{\mathrm{M}_s}{\mathrm{Re}_s}\ [8]\right)$; for the continuous flow past the particles, $\varphi = \Phi_2 = 1$. The quantities $\frac{\mu^*}{\mu_c^*}$ and $\frac{\lambda^*}{\lambda_c^*}$ are square-root functions of $\frac{T^*}{T_c^*}$.

Let us introduce a curvilinear coordinate system whose x and y axes are directed along the generatrix and normal to the surface, respectively, and the dimensionless variables $x = \frac{x^*}{L}$, $y = \frac{y^*}{L}$, $\rho = \frac{\rho^*}{\rho_c^*}$, $n_s = \frac{n_s^*}{n_{s\infty}^*}$, $\mu = \frac{\mu^*}{\mu_c^*}$, $p = \frac{p^*}{\rho_c^* U^2}$, $T = \frac{2T^* c_p}{U^2}$, and $T_s = \frac{2T_s^* c_p}{U^2}$. Here, $n_{s\infty}^*$ is the characteristic particle concentration in the dust layer and c_p is the specific heat of the gas at constant pressure. The phase velocities are scaled to U, the phase temperatures are scaled to the limiting drag temperature for the hypersonic velocity of the free stream $T_c^* = \frac{U^2}{2c_p}$, and the remaining parameters of the carrier phase are scaled to the characteristic values at the given limiting temperature.

Since the effect of the particles on the carrier phase is disregarded, we first calculate the parameters of the carrier phase and then the motion of the dispersed phase in the given velocity and temperature fields of the gas.

The gas parameters near the front surface of the sphere is numerically calculated by using the complete Navier–Stokes equations (without separating the shock wave) on a nonuniform mesh concentrated to the body surface. We use an implicit finite-difference scheme based on the finite-volume method. The inviscid components of the flow through the cell boundaries are calculated by exactly solving the Riemann problem of the decay of an arbitrary discontinuity. This problem is determined by the boundary values of the parameters in neighboring cells. These parameters are found by using a nonoscillating one-dimensional compensation of the initial physical variables: pressure, temperature, and Cartesian velocity components inside cells along the corresponding coordinates. Viscous flows through the inner boundaries of cells are calculated using the centered differences, while flows through the boundaries lying on the body surface are calculated using one-sided three-point formulas. The difference equations are solved by using an implicit two-layer iteration scheme. In the implicit part of the finite-difference operator, the directed differences are used in accordance with the signs of the eigenvalues of the Jacobi matrices of the convective terms. The system of the finite-difference equations is written in the form convenient for the application of the Gauss–Seidel iterative method for the lines along which the implicit operator is inversed by three-point runs. The details of the numerical method were described in [9].

The parameters of the dispersed phase are found by the complete Lagrangian method [10]. We introduce Lagrangian coordinates x_0, y_0, and τ, where x_0 and y_0 are the Euler coordinates of points in the dust layer at the time instant $t = 0$ and $\tau = \frac{t^* U_\infty}{L}$ is the dimensionless time of motion of a chosen particle along the trajectory.

In these Lagrangian coordinates (for fixed x_0 and y_0 values), the equations for the momentum and energy of particles in the dimensionless form are written as

$$\frac{dx_s}{d\tau} = \frac{u_s}{1 + y_s}, \quad \frac{dy_s}{d\tau} = v_s,$$

$$\frac{du_s}{d\tau} = \beta\mu G(u - u_s) - \frac{u_s v_s}{1 + y_s},$$
$$\frac{dv_s}{d\tau} = \beta\mu(v - v_s)G + \frac{u_s^2}{1 + y_s}, \qquad (1)$$

$$\frac{dT_s}{d\tau} = \frac{2}{3}\frac{1}{\mathrm{Pr}}\frac{c_p}{c_s}\beta\mu(T - T_s)D, \quad \beta = \frac{6\pi\sigma\mu_c^* L}{mU}.$$

Here, the inertia parameters of particles β and the characteristic Reynolds numbers of the flow past particles Re_{s0} (entering into the expressions for G and D) are considered as known functions of x_0 and y_0. These functions are determined by the spatial distribution (in size, mass, etc.) of particles in the dust layer.

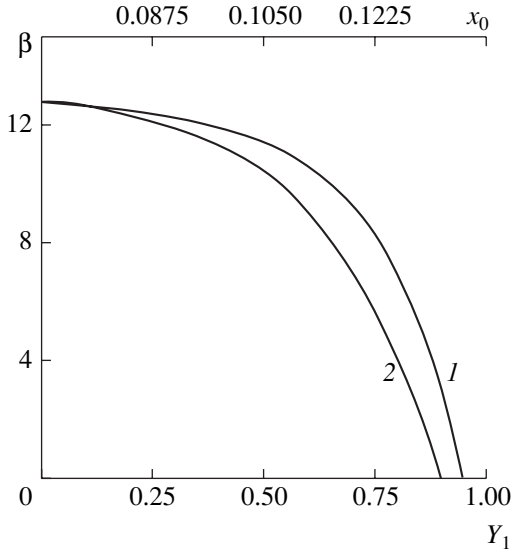

Fig. 1. Distribution of the inertial properties of particles in dust layers: (*1*) $\beta(y_0)$, (*2*) $\beta(x_0)$; $Y_1 = y_0 - y_{sh}$, where y_{sh} is the deviation of the shock wave from the symmetry axis.

In the chosen Lagrangian coordinates, the continuity equation for the medium of particles has the form

$$n_s(\tau, x_0, y_0)J(1+y)^2\sin x = n_{s0}(0, x_0, y_0)(1+y_0)^2\sin x_0. \quad (2)$$

Here, J is the Jacobian of the change of variables from x, y to x_0, y_0. According to [10], the differentiation of Eqs. (1) with respect to the Lagrangian coordinates x_0 and y_0 yields a closed system of ordinary differential equations for the components of the Jacobian J. The numerical integration of this system along with Eqs. (1)–(2) makes it possible to find all the parameters of the dispersed phase (including concentration) on a fixed trajectory of particles. The awkward differential equations for the components of J are not represented. The following initial conditions at $\tau = 0$ are set in front of the shock wave in the inhomogeneous dust layer:

$$\tau = 0: x_s = x_0, \quad y_s = y_0, \quad u_s = \sin x_0,$$
$$v_s = -\cos x_0, \quad T_s = T_\infty, \quad n_s = n_{s0}, \quad (3)$$
$$J_{11} = 1, \quad J_{12} = 0, \quad J_{21} = 0, \quad J_{22} = 1.$$

The described system of the differential equations along with the boundary conditions specified by Eqs. (3) is solved numerically by the fourth-order Runge–Kutta method. In addition, we use the linear interpolation of the gas parameters obtained by solving the Navier–Stokes equations at the nodes of the nonuniform mesh concentrated to the body surface. The calculations presented below are performed for the following parameters of the carrier phase: Re = 10^6, M = 6, $\gamma = 1.4$, $T_w = 0.42$, and Pr = 0.7 (here, the Reynolds number is calculated using the sphere radius and the parameters at infinity, γ is the adiabatic index, and T_w is the dimensionless temperature of the surface immersed in a flow).

EXAMPLES OF INHOMOGENEITIES LEADING TO UNLIMITED CUMULATION OF THE DISPERSED PHASE

The calculations are performed in the range of the parameters corresponding to the regime of inertial deposition of particles on the front surface of the body $\beta < \beta^0$, where β^0 corresponds to the boundary of the inertial-deposition regime [3]. Assuming that the entire momentum and energy fluxes of the precipitating particles are transmitted to the surface in this regime (reflected particles are ignored), the contributions of the particles to the local force $\mathbf{F}_s$ and thermal Q_s loads on the body surface (if the particle trajectories do not intersect) can be evaluated as follows:

$$\mathbf{F}_s^* = -mn_{sw}^*\mathbf{V}_{sw}v_{sw},$$

$$Q_s^* = -mn_{sw}^*v_{sw}^*\left[c_s(T_{sw}^* - T_w^*) + \frac{\mathbf{V}_{sw}^{*2}}{2}\right].$$

Here, the subscript w denotes the parameters on the surface.

According to our calculations, the difference in the inertial properties of particles can lead to their aerodynamic focusing in the shock layer of the body immersed in a flow. In this case, the spatial distribution of the inertial properties [inertia parameter $\beta(x_0, y_0)$] in the initial dust layer can be such that the peak (infinitely increasing) local fluxes of the momentum and energy of the particles arise on the body surface.

Figure 1 shows two such distributions of the inertial properties of particles. These distributions were found by parametric calculations. In the first example, the parameter β in the initial dust layer depends only on y_0 (curve *1*), and in the second example, only on x_0 (curve *2*). For simplicity, it is assumed that particles are immersed in the flow in the continuous-medium regime ($Kn_s = 0$) and the quantity Re_{s0} is constant and equal to 15. The corresponding particle trajectories in the shock layer are presented in Fig. 2. In these dust layers, the inertial properties of particles vary monotonically with the coordinate. In the first case, the inertia of the "front" particles is lower than the inertia of the "back" ones. In the second case, the low-inertia particles are located near the flow axis and the inertia of particles increases with the distance from the axis. As is seen in Fig. 2a, the finite-thickness dust layer moving in the shock layer collapses onto a surface, and all the parti-

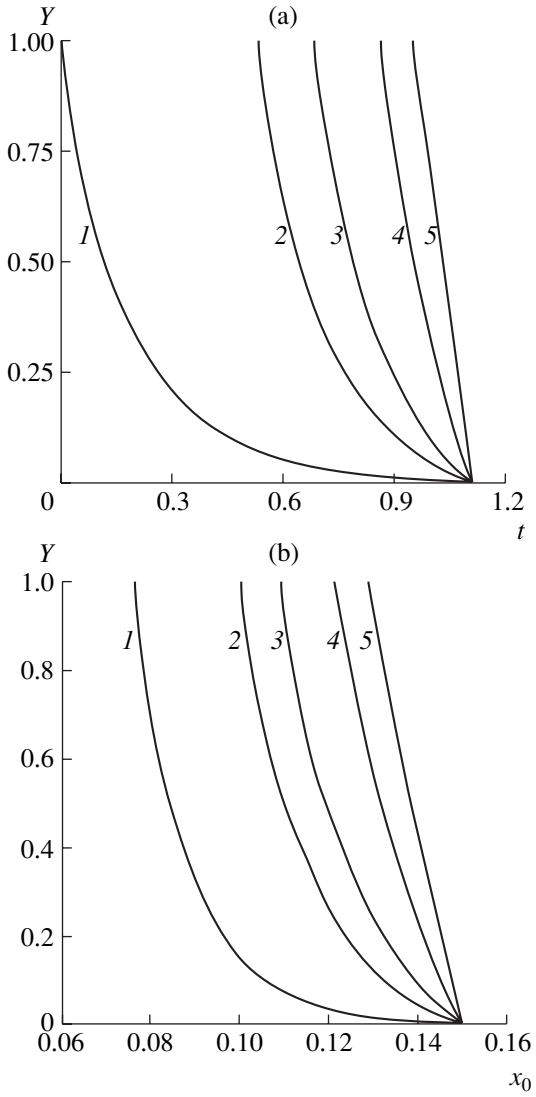

Fig. 2. Trajectories of various kinds of particles in the shock layer (a) at the symmetry axis for the case of the first inhomogeneity and (b) for the case of the second inhomogeneity for β = (*1*) 8, (*2*) 7, (*3*) 5, (*4*) 3, and (*5*) 0 and $Y = \frac{y}{y_{sh}}$.

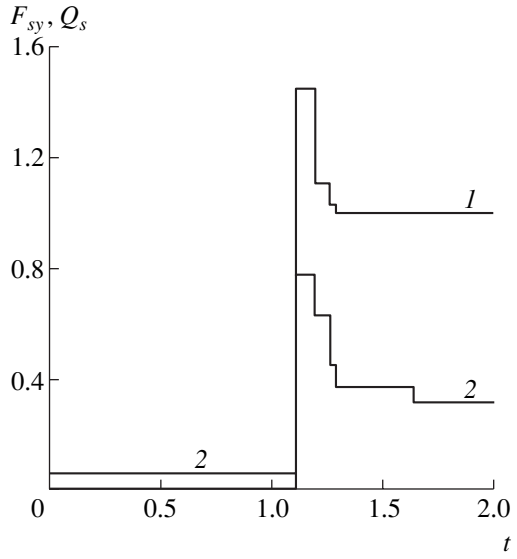

Fig. 3. Dimensionless fluxes of the (*1*) momentum and (*2*) energy of the particles at the stagnation point for the case of the piecewise constant inhomogeneity $\beta(y_0)$ approximating curve *1* in Fig. 1.

cles on the symmetry axis of the finite-thickness dust layer reach the stagnation point of the body at the time instant $\tau \approx 0.99$. In the second case, the finite tube of the particle flow has zero thickness at the side surface of the body.

For the given dust layers, the model of noninteracting particles gives infinite local momentum and energy fluxes on the surface (in the first case, they are local in time), because $n_s \longrightarrow \infty$. The formation of the peak fluxes is illustrated in Fig. 3, where the calculated dimensionless (*1*) momentum and (*2*) energy fluxes are presented. The calculations are performed for a piecewise step function that has constant β values in five identical intervals (five fractions of the particles) of the initial region Y_1 and approximates the dependence $\beta(Y_1)$ (Fig. 1, curve *1*). In this case, it is assumed that the inhomogeneous layer lies between the homogeneous layers corresponding to the most and least inertial particles, all fractions in the inhomogeneous layer have the identical initial concentrations n_{s0}^*, and $c_s = c_p$.

The dimensionless fluxes were summed over the number of fractions $i = 5$ precipitating simultaneously on the front surface:

$$F_{sy} = \sum_i n_{swi} v_{swi}^2,$$

$$Q_s = -\sum_i \frac{1}{2} n_{swi} v_{swi} \left[\frac{c_s}{c_p} (T_{swi} - T_w) + v_{swi}^2 \right].$$

The maximum momentum and energy fluxes increase infinitely with the number of partition intervals (the number of fractions).

Interparticle collisions in actual flows evidently limit infinite values of the fluxes. However, the revealed possibility of sharp peak local loads arising on the body surface must be taken into account when designing high-speed flying vehicles.

ACKNOWLEDGMENTS

This work was supported by the Russian Foundation for Basic Research (RFBR, project no. 02-01-00770) and the Chinese National Foundation for Natural Sciences (project no. 03-01-39004 joint with RFBR).

REFERENCES

1. L. E. Dunbar, J. F. Courtney, and L. D. McMillen, AIAA J. **13**, 908 (1975).
2. D. T. Hove and E. Taylor, AIAA J. **14**, 1486 (1976).
3. E. B. Vasilevskiĭ, A. N. Osiptsov, A. V. Chirikhin, and L. V. Yakovleva, Inzh.-Fiz. Zh. **74** (6), 29 (2001).
4. A. N. Osiptsov, A. V. Rozin, and B. Y. Wang, Acta Mech. Sin., No. 3, 201 (1999).
5. A. N. Osiptsov, Izv. Akad. Nauk, Ser. Mekh. Zhidk. Gaza, No. 5, 107 (2001).
6. F. E. Marble, Annu. Rev. Fluid Mech. **2**, 397 (1970).
7. D. J. Carlson and R. F. Hoglund, AIAA J. **2**, 1980 (1964).
8. I. P. Ginzburg, *Aerogasdynamics* (Vysshaya Shkola, Moscow, 1966).
9. V. I. Sakharov, V. G. Gromov, and E. I. Fateeva, *Development of the Algorithms and Comparative Analysis of the Solutions of the Problems of Hypersonic Chemically Nonequilibrium Flow around Bodies in Terms of Navier–Stokes Equations, Models of Partial Chemical Equilibrium, and Equations of Viscous Shock Layer: Report of the Institute of Mechanics No. 4507* (Mosk. Gos. Univ., Moscow, 1998).
10. A. N. Osiptsov, Astrophys. Space Sci. **274**, 377 (2000).

Translated by Yu. Vishnyakov